

Study of system trade-offs in “on-chip” hyperspectral imaging for industrial applications

Carolina BLANCH PÉREZ DEL NOTARIO

Examination Committee:

Prof. Dr. Dirk De Vos, chair

Prof. Dr. Wouter Saeys, supervisor

Dr. Ir. Andy Lambrechts, supervisor (Imec)

Prof. Dr. Ben Somers

Prof. Dr. Tinne Tuytelaars

Prof. Dr. Carlos López Molina (Public University of Navarra)

Dr. Ir. Juan Antonio Fernández Pierna (CRA-W)

Dissertation presented in partial
fulfilment of the requirements for
the degree of Doctor of Bioscience Engineering
Science (PhD): Bioscience Engineering

June 2021

© 2021 KU Leuven, Faculty of Bioscience Engineering

Uitgegeven in eigen beheer, Carolina BLANCH PÉREZ DEL NOTARIO, BELGIUM

Alle rechten voorbehouden. Niets uit deze uitgave mag worden vermenigvuldigd en/of openbaar gemaakt worden door middel van druk, fotokopie, microfilm, elektronisch of op welke andere wijze ook zonder voorafgaandelijke schriftelijke toestemming van de uitgever.

All rights reserved. No part of the publication may be reproduced in any form by print, photoprint, microfilm, electronic or any other means without written permission from the publisher.

Acknowledgements

A PhD is not the work of one single person, the main author. It reflects the contribution and support of many people in many different stages and aspects of life. Therefore, there is a long list of people I want to thank.

First, I would like to start thanking my supervisors Wouter Saeys and Andy Lambrechts for making this PhD possible. Thank you so much Wouter for your patient guidance throughout papers and manuscript. Thanks a lot Andy as well for your advice and for believing that combining my job with this was feasible. I want to extend my gratitude to all other jury members: Carlos López, Ben Somers, Juan-Antonio Fernández Tinne Tuytelaars, and Dirk De Vos for your good advice and recommendations as well. You all definitely helped improved its quality.

Thank you to all my colleagues and ex-colleagues at the Integrated Imaging group in Imec for contributing to our group and therefore to this PhD. To Hendrickje for starting to play with the illumination and triggering part of this PhD, Bert for all his help with our technology description, and everybody else not only for their individual contributions to hardware and software development but more importantly for being nice colleagues: Bart, Bert, Caglar, Eric, Kathleen, Klaas, Nick, Roeland, Siri, Thomas, Paul, Pilar, Sebastien, Vincent, and Wouter and the LFI colleagues Abdul, Geert, Jasper, Lin, Luo, Richard, Yuqian and Ziduo. My gratitude as well to the Horizon 2020 EU project Resyntex and the iFAST project from Flanders' FOOD and VLAIO for providing me nice application cases to work on.

Not to forget many Imec friends for making my life fun at Imec: my “wireless” friends Claude, Matthias, Steve, and the “Latin” gang of Adonis, Alejandra, Maritza, Mateo, Maria M., Maria V., Miguel, Monika, Pilar, Victor and Wei. Thanks for all the nice lunches and coffees and hopefully we see each other more from now on. Thank you, Pilar and Arjen, for all those nice hikes together!

Thank you so much also to all my friends in Leuven, some I met shortly after arrival during my master at KUL, others much later but you all contributed to the fact that Leuven conquered my heart, I stayed here and finally decided to go for a PhD.

Thank you to my ‘old time’ friends who I met in my first years in Leuven, some of them already gone: Abelardo, Bart, Denise, Diana, Evelyne, Helgi, Isa, Javi, Juan, Karim, Maitane, Martin, Muhua, Pascale, Pilar, Tom, Toon, Sandra, Sigrid, Wei and many others. Thank you as well to all my “galleguinhos”, who gave a Galician touch to Imec: Lucia, Jorge, Suevia, Yudani, Olalla, Estela, Diego, Abelardo, Oscar, Juan Pablo, Susana, Araceli just to name a few of them. I also have great memories with the wonderful “catalan-madrilenian-italian” imec connection: Angels, Conchi, Elena, Francesca, Gabriella, Lidia, and Santi. Thank you so much to my recently gone PhD KU Leuven friends, with whom I have shared so many great times at parties, coffees, fantastic trips, and also shared shiatsu, kizomba, boabom and inspiring seminars: Ari, Bahar, Marco, Orjon, Carolina, Martino, Fernando, Mar, Carlos and Didac.

Special thanks to my friends from Brussels and their lately frequent visits to Leuven to share coffee and chocolates: Isa, Cat and Luis. My gratitude as well to sensei Kawada for introducing me to the mysteries of a well-balanced system of body and mind and to my shiatsu friends Elena, Samia, Sylvie, Anne, Emmanuelle, Philippe... Hopefully I can go back to learn and practice with you soon.

And many thanks to the dear friends that are currently still around in Leuven sharing time with coffees, walks and talks, and giving your company and support during these difficult corona times. What would I have done without you: Adriana, Ariana, Herminia, Isobel & Joris (thanks for your help with the translation!), Koen, Maritza, Juan and Lola, Carolina, Marilu, Tom, and Wouter. Let us hope we can all meet soon again for barbecues, beers, and games. Finally, and most importantly, thank you Ronald for your continuous support (and for the nice pasta dishes that gave me the energy I needed for this PhD).

Thanks as well to many other people that are not mentioned here but that also always brought lots of laughs, smiles and happiness to my life in Leuven.

And then my roots of course, I want to share so much gratitude as well to all my friends in Pamplona, I am so lucky to have been able to keep you as friends, despite the distance and years, and to share my heart between both places. Thank you for so many years of great friendship, sharing lots of good moments: Arantza, Delia, Izaskun, Laura, Raquel, and Sara. Thank you Arantza and Silvia for putting the PhD back in my mind and to the rest of their gang (Oscar, Txema, Samuel, Txori & co) for the nice remote “pintxo-potes” during the confinement. Thank you to my university friends for still sharing Xmas dinners and much more: Delia, Enrique, Iban, Gabriel, Jesus, John-Paul, Jose-Luis, Luismi, Unai and Yoli (Greece is waiting for us).

Thanks also to the wonderful world, and its many beautiful locations that recharged my batteries and energies during trips and “holi-thesis-days” (I do think this is a great idea of my PhD, not to be patented but to be shared with the world to increase overall happiness :).

And the greatest thanks and contribution goes to my family of course, extended family like sister in-law Ana, and my uncles, aunts, cousins, and my already gone grandparents. But most important of all, to my parents, who have taught me the most important things and have given me all the support and love I can ever wish for. Thanks to my brother Alberto, for being always such a good example to follow, and to my nephew Eric, for reminding me how important it is to have fun with whatever you are doing, although, to avoid injuries, you should not try to compete with the physical enthusiasm of a mighty 7-year-old.

Abstract

Hyperspectral imaging increases the capabilities of traditional machine vision by extending the information content from three broad bands (RGB) to a spectrum of multiple narrow bands beyond the visible domain. This provides a combination of spectral and spatial information, which increases the potential for applications with respect to traditional color imaging or point spectroscopy.

While hyperspectral imaging is a technology that has already shown high potential in a wide range of application domains, its adoption by Industry has been slow so far. This has been attributed to the high camera cost on one hand and processing expertise required for the large amounts of data generated on the other hand. In this sense, recent hyperspectral technology developments are trying to bridge this gap by creating more affordable cameras that can better meet industrial needs. Typically, the development of more industrially suited cameras is done at the expense of either a lower number of bands or lower spatial resolution, which may in turn reduce their discrimination performance with respect to high-end research equipment.

To explore these trade-offs, a system-wide exploration was performed of hyperspectral imaging based on cameras, which target industrial needs. To this end, multiple system parameters such as wavelength range, camera hardware, illumination system or data analysis methods were varied for some specific applications.

First, system level optimization was explored by using the wavelength range as a key system parameter to reduce camera hardware cost for a textile sorting application. In this application, it is shown that a suboptimal wavelength range may still be able to meet the discrimination requirements, while substantially reducing the hardware cost.

Next, the focus was shifted to a case of seed mix ingredient discrimination and quantification. The added value of data preprocessing and the integration of spatial information with the spectral information is demonstrated to increase the system performance and reach the application targets. Further, it is demonstrated that the illumination system is a key parameter in hyperspectral imaging applications, in particular with snapshot cameras. The presented results show how illumination can have a relevant impact on the performance (up to 10% increase in classification accuracy) by achieving a more balanced spectral and spatial illumination.

Finally, different system parameters such as camera hardware, illumination system and data analysis methods are evaluated together. In terms of data processing, the impact of pre- and post-processing methods are explored, while pixel-based analysis is compared to a more joint spatial-spectral image analysis based on convolutional neural networks. It is demonstrated that the joint evaluation of all these system parameters allows to make the best choices to meet the application requirements and increased the mean classification accuracy by up to 25%. Moreover, it allows to explore varied system configurations that offer different performance-cost-speed tradeoffs.

To conclude this dissertation, some guidelines for system level optimization and parameter selection are proposed from the application characteristics and requirements. This paves the way for a broader industrial adoption of hyperspectral imaging technology.

Beknopte samenvatting

Hyperspectrale beeldvorming breidt de capaciteiten van traditionele machine vision uit door aan de informatie-inhoud van drie breedbandige kleurkanalen (RGB) die van verscheidene smalle banden buiten het zichtbare spectrum toe te voegen. Dit biedt een combinatie van spectrale en ruimtelijke informatie die het potentieel van toepassingen verhoogt ten aanzien van traditionele kleurenbeeldvorming of puntspectroscopie.

Hoewel hyperspectrale beeldvorming een technologie is die al veel potentieel getoond heeft in een brede waaier van toepassingsdomeinen, wordt de technologie momenteel slechts beperkt ingezet. Een mogelijke verklaring hiervoor is enerzijds de hoge camerakost en anderzijds de expertise die nodig is om de grote hoeveelheden gegenereerde data te verwerken. Recente ontwikkelingen in hyperspectrale technologie proberen aan deze verzuchting tegemoet te komen door goedkopere cameras te produceren die beter inspelen op de noden van de industrie. De ontwikkeling van meer geschikte industriële camera's gaat typisch ten koste van ofwel het aantal banden ofwel de ruimtelijke resolutie, wat op zijn beurt een negatief effect kan hebben op het onderscheidend vermogen in vergelijking met hoogwaardiger onderzoeksapparatuur.

In een nadere beschouwing van deze wisselwerking wordt een systeem brede exploratie uitgevoerd van hyperspectrale beeldvorming met 'on-chip' camera's met de opzet tegemoet te komen aan de noden van de industrie. Hierbij worden verscheidene systeemp parameters zoals golflengtebereik, camerahardware, belichtingssysteem en data-analysemethoden afgewogen voor enkele specifieke toepassingen.

Ten eerste worden de optimalisatiemogelijkheden op systeemniveau onderzocht met het golflengtebereik als essentiële systeemp parameter om de kost van de camera hardware voor een textiel-sorteesysteem te reduceren. In deze toepassing wordt aangetoond dat een suboptimaal golflengtebereik nog steeds het vereiste onderscheidend vermogen kan behalen en tegelijkertijd de hardware kost aanzienlijk kan reduceren.

Daarna verschuift de focus naar een casus waarbij de ingrediënten in een zaadmengsel herkend en gekwantificeerd moeten worden. Hier wordt de toegevoegde waarde aangetoond van data pre-processing en de integratie van ruimtelijke informatie met inbegrip van de spectrale informatie om de systeemperformantie te verbeteren en de beoogde toepassingsdoelstellingen te behalen. Verder wordt aangetoond dat het belichtingssysteem een cruciale parameter is in hyperspectrale beeldverwerkingstoepassingen en dan specifiek in combinatie met snapshot camera's. De gepresenteerde resultaten tonen aan hoe een weloverwogen spectrale en ruimtelijke belichting een substantiële impact kan hebben op de performantie (een tot 10% hogere classificatie nauwkeurigheid).

Finaal worden verschillende systeemp parameters zoals camerahardware, belichtingssysteem en data-analysemethoden samen geëvalueerd. Voor wat betreft dataverwerking wordt de impact van pre- en post-processing methoden bekeken, terwijl een pixel-georiënteerde analyse vergeleken wordt met een meer geïntegreerde ruimtelijk-spectrale beeldanalyse gebaseerd op convolutionele neurale netwerken. Het wordt aangetoond dat de gezamenlijke analyse van al deze systeemp parameters toelaat om de beste keuzes te maken om tegemoet te komen aan de toepassingsvereisten en verhoogde de gemiddelde classificatie nauwkeurigheid tot wel 25%. Deze aanpak laat bovendien toe om diverse

systeemconfiguraties te bekijken waarin verschillende afwegingen gemaakt worden tussen performantie, kost en snelheid.

Op basis van de resultaten bekomen in dit doctoraatsonderzoek worden een aantal richtlijnen voorgesteld voor optimalisaties op systeemniveau en parameterselecties op basis van toepassingkarakteristieken en -vereisten. Dit effent de weg voor een bredere industriële toepassing van hyperspectrale beeldverwerkingstechnologie.

List of Abbreviations

AOTF	Acousto Optic Tunable Filters
CNN	Convolutional Neural Network
CVF	Continuous Variable Filter
FWHM	Full Width Half Max
HSI	Hyperspectral Imaging
LCTF	Liquid Crystal Tunable Filter
LDA	Linear Discriminant Analysis
LED	Light Emitting Diode
LVF	Linear Variable Filter
MF	Median Filtering
NIR	Near infrared
QDA	Quadratic Discriminant Analysis
RGB	Red Green Blue
SAM	Spectral Angle Mapper
SNR	Signal to Noise Ratio
SWIR	Short wavelength infrared
UAV	Unmanned Aerial Vehicle
VGA	Video Graphics Array
VIS	Visible
VNIR	Visible and near infrared

Contents

Acknowledgements.....	i
Abstract.....	iii
Beknopte samenvatting.....	v
List of Abbreviations	vii
Contents.....	ix
1 Introduction	1
1.1 Potential and applications of Hyperspectral Imaging.....	4
1.2 Challenges in Hyperspectral Imaging.....	6
1.3 Key elements in a hyperspectral imaging system.....	7
1.3.1 Sample presentation.....	8
1.3.2 Illumination system.....	9
1.3.3 Imaging hardware/ hyperspectral cameras.....	12
1.3.4 Hyperspectral image analysis.....	20
1.4 Research goals and thesis outline.....	25
2 Wavelength-range as a system parameter in hyperspectral imaging for textile recycling	27
2.1 Introduction	28
2.2 Materials and Methods.....	28
2.2.1 Camera systems	28
2.2.2 Materials and methods.....	29
2.3 Results and discussions.....	35
2.3.1 Test 1: Hierarchical classification for material discrimination.....	35
2.3.2 Test 2: Extended test for one color category.....	36
2.3.3 Test 3: Proof-of-concept conveyor belt demo.....	39
2.3.4 Test 4: Denim versus non-denim discrimination	39
2.4 Conclusions	41
3 Exploiting the spatial dimension to increase performance in fast ingredient quantification with hyperspectral imaging.....	43
3.1 Introduction	44
3.2 Materials and Methods.....	46
3.2.1 Hyperspectral imaging setup	46
3.2.2 Multigrain flour samples.....	46
3.2.3 Preprocessing and classification methods.....	48

3.2.4	Image spatial post-processing.....	49
3.2.5	Estimation of abundance per seed ingredient.....	49
3.2.6	Estimation of non-seed ingredients.....	50
3.2.7	Waveband selection.....	51
3.2.8	Comparison with RGB image discrimination accuracy	51
3.3	Results and discussion	51
3.4	Conclusions	59
4	Illumination as a key element in hyperspectral imaging	61
4.1	Introduction	62
4.2	Materials and Methods.....	62
4.2.1	Camera System	62
4.2.2	Illumination Systems.....	62
4.2.3	Sample selection and processing pipeline	66
4.3	Analysis and results.....	66
4.3.1	Evaluation of HDR and the tunable LED system	66
4.3.2	Evaluation of a fixed LED bar system	69
4.4	Conclusions	73
5	Joint evaluation of the combined effect of illumination, camera hardware and analysis methods	75
5.1	Introduction	76
5.2	Materials and Methods.....	79
5.2.1	Materials	79
5.2.2	Illumination systems	79
5.2.3	Camera systems	80
5.2.4	Analysis methods	81
5.3	Results and Discussions	86
5.3.1	Impact of illumination system	86
5.3.2	Impact of classifier and camera system	86
5.3.3	Impact of pre-processing steps.....	88
5.4	Conclusions	95
6	Adding wavelength range to the joint system evaluation of hardware, illumination, and data analysis.....	97
6.1	Materials and Methods.....	98
6.1.1	Camera systems	98
6.1.2	Sample selection and processing pipeline	99

6.2	Results and discussion	100
6.3	Conclusion.....	102
7	Conclusions and future work	103
	References	109
	List of publications	125
	Biography	127

Chapter 1

Introduction

A worldwide growing population together with its increasing demand for food has led to a forecast of food scarcity to feed future population. This motivates the need for a more efficient and sustainable way of producing and consuming food (Kakani et al., 2020). Last but not least, food quality and safety need to be guaranteed. To achieve this, further automation in food processing and agro-food sectors play an important role. In this respect, the Fourth industrial revolution (or Industry 4.0), is enhancing the automation and control mechanisms in food production processes by allowing real time data monitoring and tracking of the product status. This revolution is fueled by modern smart technology such as artificial intelligence and the internet of things (Vaidya et al., 2018), (“Fourth Industrial Revolution”, 2020). As food sorting is still largely done through visual inspection, computer vision is widely investigated for automating this process (Brosnan et al., 2004), (Patel et al., 2012), (Kakani et al., 2020).

This information technology provides opportunities for feeding and clothing this growing population in a more sustainable way. Indeed, Industrial production processes account for a considerable share of the overall pollution and are accountable for many environmental problems (“Sustainable production and consumption”, 2020). One example is the fashion industry, which uses a huge quantity of raw materials and generates a substantial amount of waste in its production process (Toprak et al., 2017). Moreover, only a small fraction of wearable textiles is recycled, while most of the used textile ends landfilled or incinerated, with a high environmental impact (Sandin et al., 2018). Therefore, a great deal of effort has been directed to better waste management and product recycling. In this respect, computer vision also plays an important role in the recycling industry (Tomaselli, 2019, Wang et al, 2020).

The origins of **computer vision** date back to the 1960s and since then it has experienced considerable growth in diverse fields such as medical diagnostics, factory automation, remote sensing, and the food industry. Automatic inspection systems based on the combination of digital cameras and computers have proven to be successful for objective measurement and quality assessment in the agricultural and food production sectors (Timmermans et al., 1996), (Brosnan et al., 2004). Its main advantages are that it is more efficient, objective, non-invasive and it offers a fast and automatic tool to replace human visual inspection. To do so, a computer vision system includes a physical image sensor with which images are captured, and dedicated computing hardware and software to process and analyse the images to perform a predefined visual task. Traditionally, the image analysis performed was based on image characteristics such as color, shape or geometry, which were combined in an ad hoc algorithm elaborated by an expert. More recently, advances in machine learning, such as deep learning and convolutional neural networks, have largely automated this process and expanded the possibilities of computer vision for object detection or recognition (Kakani et al., 2020). Another technology with many applications in food quality control is Near InfraRed Spectroscopy (NIRS). This technology exploits the wavelength dependent conversion of electromagnetic energy into molecular vibrations to obtain a spectroscopic fingerprint in the wavelength range from 750 to 2500nm. This was the first part of the electromagnetic spectrum discovered outside the visible range (Pasquini, 2018).

The potential of point spectroscopy for the agri-food sector was discovered in the 1960s with the work of Karl Norris, which promoted advances in instrument manufacturing and analytical tools. Nowadays, it has become the preferred quality control method in the food industry because it offers multiple advantages over traditional chemical techniques (Manley et al., 2018). Its main advantages are being a non-invasive tool, not requiring chemical treatment of the sample and allowing fast and accurate chemical analysis. However, a disadvantage of point spectroscopy is the lack of imaging capabilities, which limits the acquired fingerprint to a local or average value and thus ignores the spatial heterogeneity. Some of the most important applications of near infrared point spectroscopy in the food and feed industry are, for instance, food quality assessment, process control (Manley et al., 2018), food safety and authenticity (Qin et al., 2017).

Hyperspectral imaging combines the characteristics of computer vision and point spectroscopy by obtaining an image with both spatial and spectral information. This technique enables therefore to analyse the chemical composition of materials and simultaneously visualize their spatial distribution (Kamruzzaman et al., 2012). In Figure 1-1, the trade-off offered by hyperspectral imaging in terms of spectral and spatial resolution is illustrated. Some of the advantages of hyperspectral imaging over point spectroscopy are that it allows visualization of feature distribution over a product, better dealing with heterogeneous products since more representative samples can be acquired and faster inspection over a batch of products. The first hyperspectral imager was developed in the 1970s for Earth remote sensing. By the late 1980s several commercial hyperspectral imagers were available on the market (Goetz, 2011). Since then, it has been a rapidly growing market with applications in remote sensing, medical imaging, forensics, and agri-food processing.

The main disadvantages of hyperspectral imaging with respect to point spectroscopy or traditional colour imaging are related to the higher amount of data that has to be stored and processed. Moreover, the cost of hyperspectral cameras is typically higher than the one of colour cameras, and this for a lower spatial resolution. In addition, hyperspectral cameras generally require higher light intensity than colour imaging, which can result in higher integration and acquisition times.

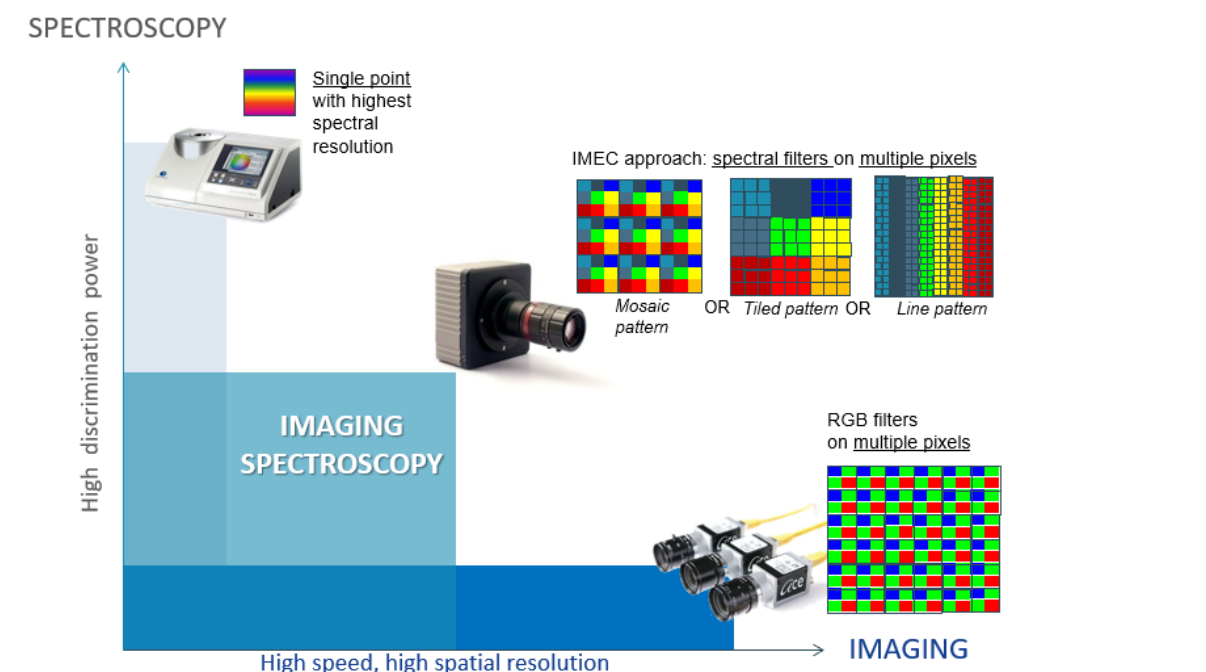


Figure 1-1: Schematic illustration of different configurations for hyperspectral imaging and their position as a method between point spectroscopy and RGB imaging. - Courtesy of Imec

Colour imaging acquires three broad spectral bands corresponding to the ranges of the electromagnetic spectrum which humans perceive as Red, Green and Blue. Hyperspectral imaging subdivides these broad bands into many more narrow bands and can potentially go beyond the visible light domain (400-750 nm) extending for instance to the infrared domain (750 nm – 1000 μm) or the ultra-violet range (10-400 nm). This greatly increases the amount of information from an image and provides for every pixel in the image a full spectrum, indicating how the light is reflected in the pixel for a range of wavelengths. Figure 1-2 shows the distribution of the full electromagnetic spectrum. The visible portion of the electromagnetic spectrum extends from 400 nm to 750 nm. It is only a very small part of the overall range of wavelengths in the spectrum. The infrared range includes a broad range of wavelengths from 750 nm to 10⁶nm. The part of the range closest to the visible spectrum is called near infrared (750 – 1000 nm), the 1000-3000 nm range is denominated as short-wave infrared (SWIR) and the 3000-8000nm as mid-wave infrared (MWIR). The longer wavelength parts of the infrared spectrum are called long-wave infrared (LWIR) in the (8-15 μm) and far infrared (FIR) from 15 to 1000 μm.

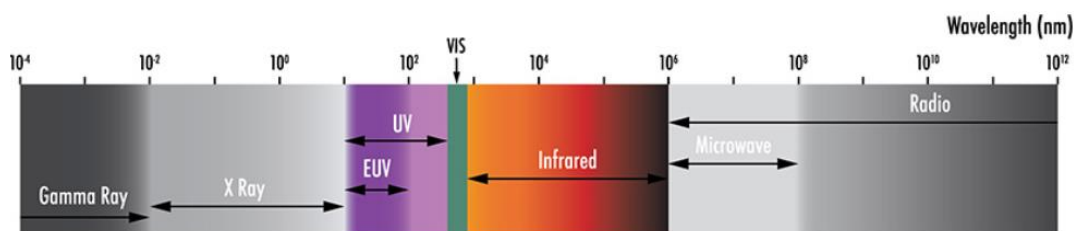


Figure 1-2: The electromagnetic spectrum (“Hyperspectral and Multispectral Imaging”, 2021)

The hyperspectral image data can thus be perceived as a three-dimensional data cube, where every two-dimensional band image provides information about a specific reflected band. This is schematically illustrated in Figure 1-3.

**HYPERSPECTRAL IMAGING:
A COMBINATION OF SPECTROSCOPY AND IMAGING**

Improves machine vision by using spectral information of surface material being imaged

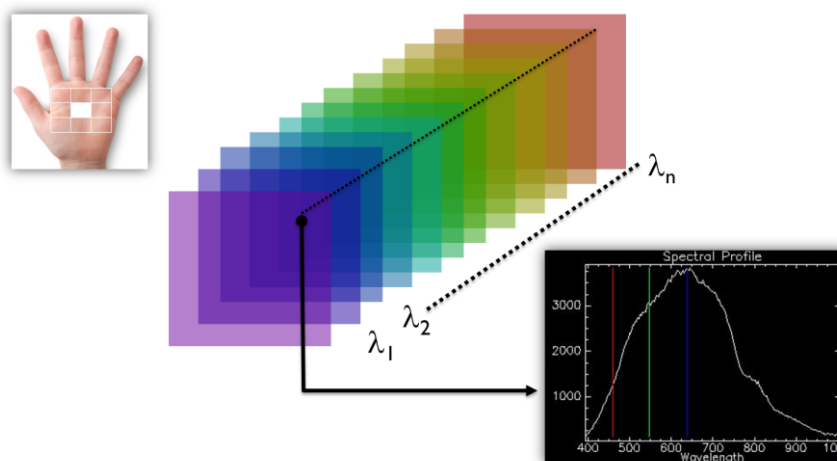


Figure 1-3: In hyperspectral imaging, n different band images are acquired, such that for every pixel in the image a spectrum is obtained. - Courtesy of Imec.

Acquiring the spectrum or spectral signature for every pixel in the image has the potential to greatly increase the material information and discrimination capabilities with respect to traditional RGB machine vision.

Like other spectroscopy techniques, hyperspectral imaging can be performed in transmittance, transreflectance, or reflectance mode. These terms refer to different geometric arrangements of the radiation beam, sample, and detection system (camera, spectrometer) used to measure the spectral information of the sample. These three modes are schematically illustrated in Figure 1-4 (Skvaril et al., 2017).

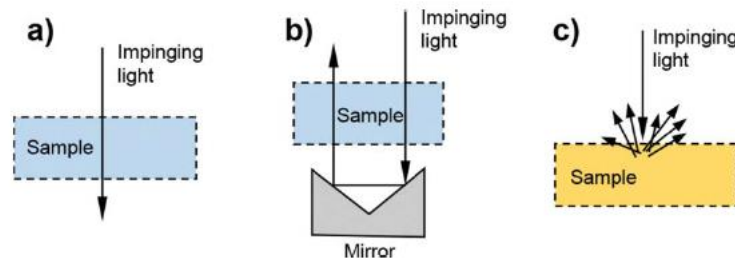


Figure 1-4: Measurement modes in hyperspectral imaging/NIR spectroscopy: a) Transmittance b) Transreflectance c) Diffuse reflectance. (Skvaril et al., 2017)

In transmission mode we acquire the light that has travelled through the sample. In transreflectance mode, a reflector is placed at the back of the sample to send all transmitted light back through the sample to be collected with the reflected light. When no mirror element is used this is also called interactance. Finally, in diffuse reflectance mode, the portion of the incident light reflected by the sample is quantified as a function of the wavelength. As most agrofood samples are highly turbid, diffuse reflectance imaging is most widely used for quality inspection of agrofood samples (Lu et al., 2020).

1.1 Potential and applications of Hyperspectral Imaging

Some key advantages of hyperspectral imaging are that it is a non-invasive, non-contact and non-destructive technology, which makes it suitable for product inspection applications such as food inspection (Amigo et al., 2013) or industrial recycling of plastics (Bonifazi et al., 2019), (Serranti, 2019) or textiles (Blanch et al., 2016), (Mäkelä et al., 2020).

In (Khan et al., 2018) several applications are presented where hyperspectral imaging has gained high interest in the recent years: namely food inspection, forensic science, medical surgery and diagnosis and military applications. This growing interest was fuelled by technological advances in hyperspectral instrumentation as well as in computer technology. Hyperspectral cameras of lower size and cost factor providing faster acquisition and increased resolution have become available in the last decade (West et al., 2019). In addition, processing devices are becoming increasingly more powerful to process the large amount of data acquired by hyperspectral imagers (Traore, 2017), (Plaza et al., 2011). Finally, the recent advances in machine learning and deep learning are also providing powerful means for processing these images (Gewali et al., 2018), (Paoletti et al., 2019).

In terms of market, agriculture, military surveillance, environmental monitoring, food processing, and remote sensing are the major application domains for hyperspectral imaging (“Hyperspectral imaging market: Key insights”, 2018). In this respect, the use of hyperspectral imaging in these fields is

forecasted to have a cumulative annual growth rate of around 10% in the coming years (“Hyperspectral imaging market: growth, trends, and forecast (2019-2024)”, 2019).

The high number of band responses provided by hyperspectral imaging allows to quantify the biological and chemical properties of materials. Therefore, there is a high number of applications in remote sensing for agriculture such as identification of crop species, soil analysis, crop management, detection of plant stress and diseases (Vinod et al., 2017). The growing adoption of Unmanned Aerial Vehicles (UAVs) across the countries, backed up by a more flexible government regulation in the use of UAVs, is also propelling the market growth in fields such as surveillance, remote sensing and precision agriculture. In this respect, the development of smaller and lighter hyperspectral cameras is also promoting the use of hyperspectral imaging on UAVs for remote sensing application (“Smallest hyperspectral camera”, 2014), (Lanaras et al, 2018) and precision agriculture (Van de Vijver et al., 2020).

One of the application fields where hyperspectral imaging has experienced a high growth is food quality and safety inspection (“Hyperspectral imaging market: growth, trends and forecast”, 2019), (Amigo et al., 2013), (Sun, 2010). Hyperspectral imaging technique has been identified as a promising tool as a fast and reliable method for food inspection with the additional advantage of being non-destructive and non-invasive. In this respect, there is a growing need for efficient food control to reduce the food waste (caused partly by traditional destructive methods) (Ramanan et al., 2018). In fact, a third of all food produced in the world is wasted. In this respect, the authors in (Ramanan et al., 2018) believe that hyperspectral imaging can help reduce the food losses at production and supply level to ensure sustainable production patterns. It is believed that non-invasive, rapid, objective techniques for monitoring food products, such as hyperspectral imaging, are essential to improve the sorting and distribution processes. Therefore, a very important aspect in food control is food (and feed) quality assessment (Fernandez-Pierna et al., 2014), (Fernandez-Pierna et al., 2020), process control (Manley et al., 2018), and food safety and authenticity (Flemal et al., 2017), (Shen et al., 2020).

The potential for fast product inspection in hyperspectral imaging is not limited to food inspection, but extendable to a variety of products. In this respect, research has been done as well to evaluate the feasibility of hyperspectral imaging for the sorting/recycling industry. In (Moroni et al., 2015) the authors demonstrate that a two-band relation in the 1100-1700 nm range can discriminate between PVC and PET plastics with 100% accuracy. In (Bonifazi et al., 2019) 8 different types of plastic polymers are accurately discriminated with hyperspectral imaging in the 1000-2500 nm range.

In addition to the mentioned applications there are several fields where hyperspectral imaging is showing its potential. Hyperspectral Imaging has for instance been used for detection of biological traces in forensic evidence (Malegori et al, 2020) or forensic examination such as document forgery detection (Edelman et al, 2012). In addition, it has been successfully used for art inspection, for instance pigment determination in paintings (Daniel et al, 2016) or artwork authentication (Polak et al, 2017) or medical surgery and diagnosis such as tumor detection (Liu et al, 2012) or measurement of tissue oxygenation during surgery (Olweny et al, 2013). Last but not least, in (Krupnik et al, 2019) a review is made on the use of hyperspectral imaging for mining applications such as close-range material exploration in mines and quarries.

1.2 Challenges in Hyperspectral Imaging

Despite the high potential of hyperspectral imaging for a wide variety of applications, this technology has not yet been widely adopted by industry (“Hyperspectral imaging market”, 2018), (“Hyperspectral imaging market – growth, trends and forecast (2019-2024)”, 2019). There are several challenges to be tackled for this to happen.

One important challenge of hyperspectral imaging is that it generates high volumes of data that need to be processed (Bioucas-Dias et al., 2013). In fact, a high number of band responses comes with considerable data redundancy. A data cube of high spatial resolution and hundreds of band responses can easily represent Giga Bytes (GB) of data for one single hyperspectral image. In addition, expertise is needed to process and interpret this high volume of hyperspectral data (“Hyperspectral imaging market”, 2018). In this respect, machine learning techniques are frequently used to address hyperspectral data processing.

Next to this, there are other technical challenges such as the use of adequate illumination systems (Katrašnik et al., 2013). For instance, for product inspection on a conveyor belt, hyperspectral cameras generally require higher intensity illumination than colour-based cameras. With traditional halogen-based systems this implies generating a considerable amount of heat, which is undesirable in the food industry.

Finally, a second main challenge remains the cost of hyperspectral cameras, which is still considerably higher than that of traditional colour cameras. In addition, it is still challenging for them to meet the acquisition speed or spatial resolution required in industrial inspection systems, typically of around 3 m/s in terms of conveyor belt speed (He et al., 2018).

In this respect, it is important to benchmark hyperspectral imaging with respect to colour imaging for any given application. Colour cameras are cheaper than hyperspectral cameras, allowing for high-speed acquisition and available in high spatial resolution and compact form factors. Therefore, they must be considered as the preferred alternative to hyperspectral imaging whenever a traditional RGB camera can meet the application requirements in terms of discrimination power. Additionally, traditional computer vision with a colour camera may represent a compromise offering reduced (but potentially enough) discrimination power at a reduced cost or increased speed for instance.

1.3 Key elements in a hyperspectral imaging system

This section introduces the key elements of a hyperspectral imaging system, while the following sections describe each of these elements and how state-of-the-art research has addressed them. The remaining research challenges and gaps concerning each of these system elements and the full system will be identified. In addition, we will explain how this thesis is tackling the identified challenges in the different chapters.

The key elements of a hyperspectral system are basically identical to those of a generic computer vision system: illumination, a camera, an image capture board (frame grabber or digitiser), computer hardware and software (Wang et al., 2002), (Brosnan et al., 2004).

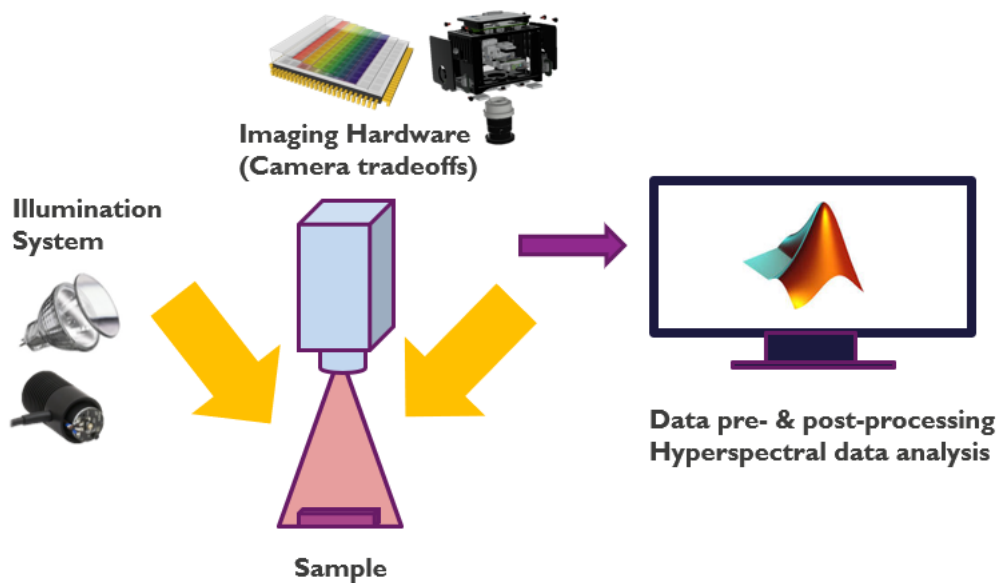


Figure 1-5: Components of a hyperspectral imaging system

Figure 1-5 illustrates the key elements that we can find in a hyperspectral imaging system: lights (in other words an illumination system), the imaging hardware (in this case a hyperspectral camera and lens system), computer hardware and software (namely pre/post-processing and analysis methods used) and finally, the samples considered (type and number of samples, background used...).

All these elements in the hyperspectral system play a key role in determining the final discrimination accuracy. In the remainder of this section the relevance of each of these elements is discussed in more detail.

1.3.1 Sample presentation

The way a sample is presented to the hyperspectral system, for instance in terms of background choice, can have a considerable impact on the system performance. Despite the relevance of the background choice as a mean to increase discrimination when samples are for instance translucent or in general to help avoid shades or specular effects, very few works exist in literature focusing on these aspects. In (Signoroni et al., 2020) the authors analyze the effect of how different background choices and the illumination set up impact the object spectral signature. It is concluded that proximity to light sources or non-homogeneous light distribution can cause unwanted glare. Moreover, white backgrounds tend to produce more glare as well than black backgrounds, and this particularly on darker objects. In (Herrero et al., 2019) it is shown that the material of the petri dish used (polystyrene or glass) interferes with agar measurements. A method is therefore developed based on orthogonal projection to reduce the measurement interference of the petri dish material. Indeed, when imaging translucent material there is a clear impact or spectral mixing with that of the background underneath. In (Mindermann, 2018) it is shown how the spectral signature of ink and background paper material is mixed, which may hamper the discrimination power of hyperspectral imaging. To reduce this impact of the background some methods such as Independent Component Analysis or Canonical Variance Analysis were successfully used. Glossy surfaces with high reflection also pose a challenge for hyperspectral imaging. To avoid this problem, Nguyen et al. (2016) used polarised light to block the specular reflections on glossy surfaces of aubergines and apples. It was shown that the use of polarised light increases the spectral signal-to-noise ratio from 1.1 to 3 times depending on the wavelength region. In a similar manner, to deal with the glossy surface of fish skin, (Folkestad et al, 2008) used an interactance system that blocks the light that is reflected on the surface and only measures the light that has penetrated sufficiently into the fish muscle before being reflected. This allowed better prediction of muscle pigment concentration through the skin in live or whole fish. Similarly, Wold et al. (2006) used an interactance system to estimate with high accuracy moisture in dried salted coalfish (bacalao). In this study, it was shown that interactance measurements outperformed reflectance measurements, thanks to the deeper penetration of light into the sample.

In summary, one important aspect of the sample presentation is the choice of the background to avoid spectral interferences or unwanted glares and shades. When the sample itself is glossy or specular, we can partially deal with this by a careful choice of the illumination system and optical components. Sample presentation is not the focus of this thesis. However, the background considerations made to avoid the above-mentioned issues are addressed in the following chapters.

1.3.2 Illumination system

The level and quality of illumination has a high impact on any vision system, including the human visual system. The appearance of an object and its features of interest can dramatically change with the lighting used. Therefore, the image quality and overall system accuracy is highly dependent on the illumination used (Sarkar, 1991), (Novini, 1995), (Brosnan et al., 2004). For instance, Gunasekaran (1996) found that suitable lighting can reduce unwanted reflections, shadows, and image noise.

The illumination system is a key element for any imaging system, but in the case of hyperspectral imaging it plays an even bigger role than for traditional machine vision systems with color imaging (Herrala, 2020).

When designing an illumination system, three important aspects must be considered:

- **Light intensity:** hyperspectral imaging requires brighter illumination than color imaging. Since hyperspectral imaging systems split the reflected light in many more narrow wavebands than RGB cameras, the overall intensity is distributed over multiple narrow bands. This makes the fraction of the illumination power that reaches each detector element much smaller (Herrala, 2020). The way to compensate for this is to use longer integration/exposure times or to increase the illumination power on the sample.
- **Spectral distribution:** to be able to measure the reflected/transmitted light over a specific wavelength range we should use a light source which emits in the desired wavelength range. In this respect, the illumination should emit continuously and with sufficient power over the wavelength range that we want to measure, this may be the full visual-near infrared range (400-1000 nm) or a portion of the short-wave infrared range (1000-1700 nm). In any case, it is also preferable that the energy is homogeneously distributed over the spectra, to achieve a more balanced Signal to Noise Ratio (SNR) over the full measured wavelength range. Specifically, in camera systems where all wavelengths are captured simultaneously (and therefore with the same exposure time) an energy unbalanced light spectrum may cause the sensor to saturate at some bands while being underexposed at other wavelengths. This is the case in the camera systems that will be presented in Section 1.3.3.
- **Spatial distribution:** achieving a homogeneous spatial distribution of the light energy is also very important. This means that the incident light at each position of the imaged area should have the same spectral response and intensity. In addition, shadows and specular reflections should be avoided in the illuminated area. This is, in practice, very difficult to achieve with a single light source. The use of multiple light sources instead of one helps to increase the spatial uniformity if they are positioned carefully (Gunasekaran, 1996) (Keresztes et al., 2016).
It is important to note that in the case of line scan imaging where one line is imaged at a time it is easier to achieve homogeneous illumination over the scanned line with a bar type light. However, with Snapshot cameras (e.g Mosaic sensors in Section 1.3.3) or Snapshot-alike acquisition (e.g Snapscan camera in Section 1.3.3) homogeneous spatial illumination is required over a broader area than for line scan systems. This is considerably more challenging to achieve.

Traditionally, halogen lighting has been used since it emits radiation over the spectral range where NIR cameras are sensitive, as shown in Figure 1-6. However, some disadvantages of halogen lighting are that they have a low optical efficiency and emit over a broader range than the one sensed by NIR cameras. Consequently, halogen light sources are power hungry and generate a considerable amount

of heat which may increase the sample temperature. For specific hyperspectral applications, such as food inspection, medical imaging, and art inspection this is very undesirable.

In this sense, LED lighting could be a good alternative since it is less power hungry and generates very little heat. However, as illustrated in Figure 1-7, the emission spectrum of a LED is not flat over the full wavelength range covered by a VNIR or SWIR camera. Moreover, their light intensity is also lower than that of halogen sources. For all these reasons their use has been scarce so far, and halogen lighting systems remain widely adopted in hyperspectral imaging.

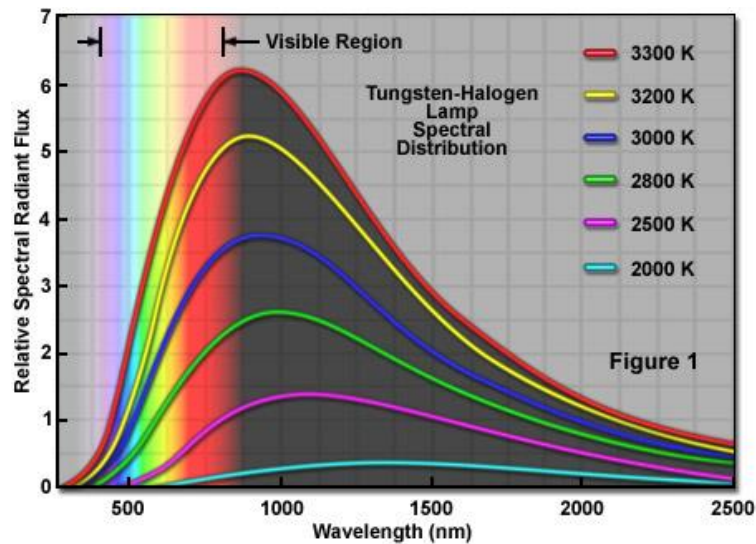


Figure 1-6: Energy distribution of Halogen light source (Davidson, 2015)

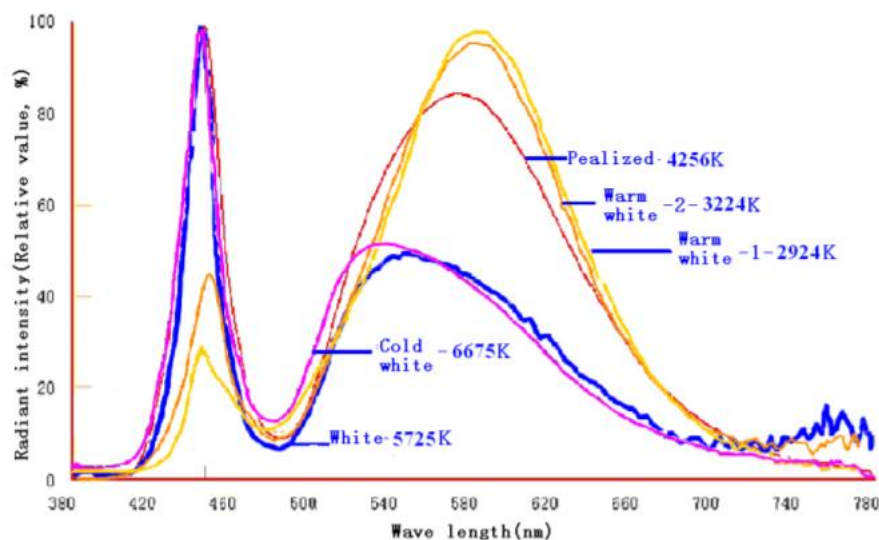


Figure 1-7: Spectral distribution of different kinds of LED lights (Kim et al., 2016)

More recently, LED lighting technology is experiencing considerable advances that enable the use of LED illumination for hyperspectral imaging systems. This is achieved by adding phosphors or quantum dots which absorb photons emitted by the LED and re-emit photons at longer wavelengths (Mills, 2005), (Goeltner, 2020). This way, LED manufacturers such as (CVR lighting, Ltd 2015), (Effilux LED lighting, 2009) or (Metaphase Technologies Inc) are now providing LED light sources with emission in

the 400-900 nm range) without band gaps, therefore, better matching the requirements of hyperspectral systems. Figure 1-8 illustrates the energy distribution over the spectrum for an Effilux LED bar. We can see that it succeeds in covering in a continuous way most of the 400-1000 nm of the visual-near infrared range, but still contains some clear peaks and valleys related to the emission peaks of the LEDs and phosphors.

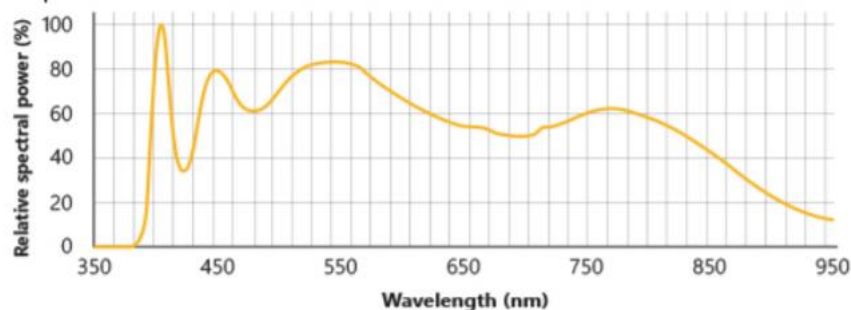


Figure 1-8: Energy distribution of Effilux LED bar ("Effi-flex", 2020)

The illumination unit in an HSI system has a considerable impact on the system performance (Peter, 2015; Sawyer et al., 2017). Nevertheless, most researchers have dedicated considerably less effort to improve the illumination systems used than to develop more advanced machine learning techniques. As a broad-spectrum illumination is desired for hyperspectral imaging, halogen-tungsten illumination is generally used together with hyperspectral systems (Keresztes et al., 2016), (Lu et al., 2020). With the increasing availability of LEDs with different spectral characteristics, some research has also focused on exploring the suitability of LED illumination systems. To this end, Peter (2015) developed several LED ring illumination systems for 680, 780 and 800nm and tested these for a skin imaging application system, relating viewing angles to the number of LEDs required for uniform area illumination. However, they did not report on any benchmarking against halogen systems. Lawrence et al. (2007) compared a traditional halogen system with a LED system for fecal contamination detection obtaining a detection accuracy of 99% for both systems. Kutrašnik et al. (2013) presented a method to compare lighting systems based on spatial-intensity and spatial-spectral non-uniformity measures. They aimed to avoid specular reflections, shadows, and shades, but did not consider a specific application for testing and benchmarking. Pan et al., (2017) explored the impact of different illumination patterns (reflectance, transmittance, and semi-transmittance) on the hollowness classification of white radish. The best classification accuracy of two-class hollowness, 97% on the prediction set, was reached with transmittance imaging. Carstensen (2018) presented a LED based system for a food control application in combination with a color camera but did not benchmark it against halogen systems. Sawyer et al. (2017) compared the uniformity of halogen and LED based illumination systems for a biomedical application but did not report their impact on the discrimination power.

From the above review of the state of the art it is clear that few researchers have investigated the impact of different illumination systems for a specific application case and in a quantitative way. Moreover, the effect of the illumination system has not yet been studied jointly with other system parameters such as camera hardware or analysis method employed. Chapter 2 of this thesis will investigate the impact of illumination in hyperspectral systems as a key system component.

1.3.3 Imaging hardware/ hyperspectral cameras

Hyperspectral image data can be acquired in different ways, known as spatial scanning, spectral/wavelength scanning, spatio-spectral scanning, and non-scanning (or snapshot) imaging (“Hyperspectral Imaging”, 2021), (Hagen et al., 2013). In Figure 1-9 these different acquisition methods are illustrated.

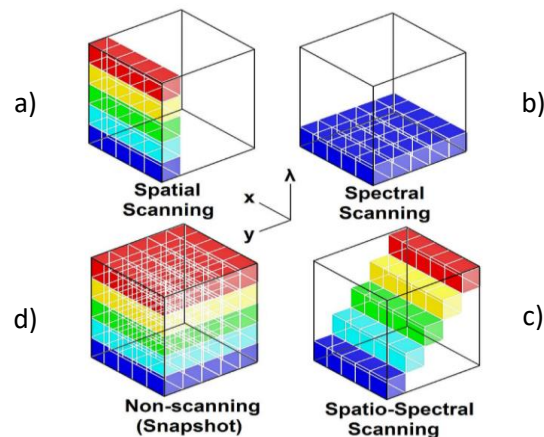


Figure 1-9: The portions of the datacube collected during a single detector integration period for a) spatial scanning, b) spectral scanning, c) spatio-spectral scanning and d) snapshot acquisition. (“Hyperspectral Imaging”, 2021)

In **spatial scanning**, each two-dimensional sensor output corresponds to a full slit spectrum. A strip of the scene is projected onto a slit, which is dispersed by a prism or a grating. The image is acquired line by line in a push broom manner (Elmasry et al., 2012), (Behmann et al., 2018), (Ortega et al., 2019), and a scanning movement is required to capture a full hyperspectral 3d cube. Traditional hyperspectral cameras performing spatial scanning are based on a prism grating system, relatively bulky and expensive (due to the required internal optical elements).

In **spectral scanning**, the full image is acquired for an individual waveband at a time. This way, each 2-D sensor output represents a single band image of the scene. These devices are typically based on optical band-pass filters, which can be tunable or fixed. An example of such tunable filter system is a filter wheel system, shown in Figure 1-10, where a rotating wheel is synchronized with the camera acquisition per filter. Such systems offer a reduced number of filters and their acquisition speed is limited to the mechanical rotation speed.

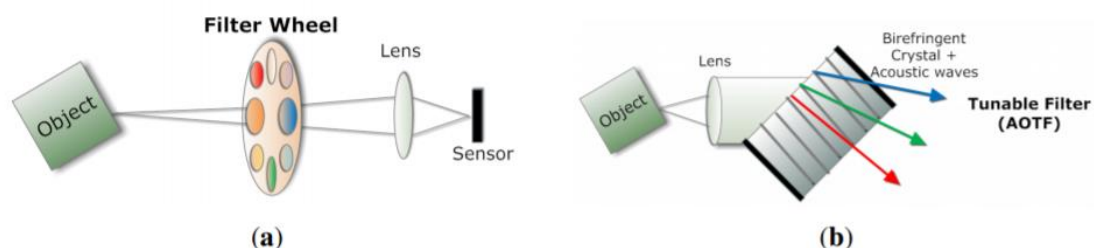


Figure 1-10: Schemes of a) Filter wheel with optical bandpass filters and b) AOTF where sound waves are used to diffract and shift the frequency of light (Lapray et al, 2014)

Among electronically-tunable filters, the two most used ones are liquid crystal tunable filters (LCTF) and acousto-optic tunable filters (AOTF). HSI techniques based on Acousto Optic Tunable Filters

(AOTF) and Liquid Crystal Tunable Filters (LCTF) (Abdlaty et al., 2018) require polarized light to achieve spectral selectivity. For this reason, their use is limited in low light applications, since their throughput is at most 40%, lower than the 60–90% typically reached by thin film band-pass filters.

Spatio-spectral scanning yields a series of thin, diagonal slices of the data cube, as shown in Figure 1-9. Each acquired image is a 'rainbow-colored' spatial map of the scene, where different lines correspond to different wavelength responses. Therefore, to acquire the spectrum of a given object point, scanning is needed. Examples of spatio-spectral scanning systems are Imec line-scan (Gonzalez et al., 2016) and Snapscan camera systems, (Pichette et al., 2017). In both spectral and spatio-spectral scanning careful alignment of the camera sensor and the translational movement is required to reconstruct an accurate spectrum with all bands available in all sensor pixel positions (Gutierrez et al., 2019). An example of a tunable filter system is the hyperspectral camera concept of (Ahlberg et al., 2017) where a Continuous Variable Filter (CVF), a.k.a Linear Variable Filter (LVF) of Delta Film (Fabricius et al., 2014) is used. The 18 bands in the VNIR range are acquired with the translational movement of the UAV and used to reconstruct the 3D structure in the scene.

Finally, in **non-scanning or snapshot hyperspectral** systems the full 3D hyperspectral data cube, with multiple bands per image point, is captured at once, without the need for scanning. Lapray et al, (2014) provide a good review of the different technologies used to develop snapshot multispectral and hyperspectral systems. One of the first methods to be used to implement a snapshot spectral imager, limited to 3 or 4 bands, was beam-splitting, as shown in Figure 1-11.

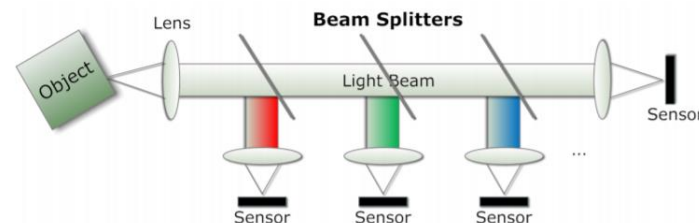


Figure 1-11: Multi-spectral snapshot system with three beam splitters.

Another way to implement snapshot imagers is by means of a lenslet array, which in combination with a filter array inserted in front of the lenslet array or image sensor allows to duplicate and project the image of each lenslet on the corresponding area of the sensor. One example is shown in (Hubold et al., 2018) where a Continuous Variable Filter (CVF) of Delta Film is used together with a microlens array to provide simultaneous snapshot acquisition of 66 bands in the VNIR range (450-880 nm) with a spatial resolution of 400x400 pixels per band.

Another way to implement a snapshot system is by using Multi-Spectral Filter Arrays (MSFA) that integrate multiple filter elements in a mosaic pattern. This results in superpixels, where the pixels for the different wavebands are spatially separated in a mosaic arrangement. The hyperspectral filters are arranged onto individual pixels extending the Bayer colour imaging concept to hyperspectral imaging where video rate acquisition can be reached without dedicated fore-optics or linear scanning. An example of this is shown in (Geelen et al., 2015), where snapshot cameras in the visible and near-infrared ranges are showcased.

Generally, scanning acquisition systems such as spatial scanning, spectral scanning or spatio-spectral scanning can obtain hyperspectral images with high spectral and spatial resolution, but require time for the scanning. In contrast, snapshot systems trade-off between spectral and spatial resolution to be able to provide instantaneous and faster acquisition than scanning systems. While scanning systems, requiring multiple exposures, are more exposed to motion artifacts, a snapshot imager capturing a multispectral image at one single exposure, can better avoid such artifacts.

Although the potential of hyperspectral imaging has been demonstrated for several applications using laboratory setups, it is generally still a scientific tool. Indeed, most commercial hyperspectral cameras are made for the research market, e.g., remote sensing (Van der Meer, 2012), (Vinod et al., 2017) and food science (Feng et al., 2012), (Amigo et al., 2013). The adoption of hyperspectral imaging by the industry has so far been limited due to the lack of fast, compact, and cost-effective hyperspectral cameras with adequate specifications (“Hyperspectral imaging market”, 2018). Nevertheless, over the last decade there have been important technological advances in the design of the sensors and cameras, which have fuelled the growth of the hyperspectral imaging market.

“On-chip” hyperspectral camera systems

One of these advances is the development of a unique hyperspectral sensor concept in which the hyperspectral filters are monolithically integrated on top of a chip, a standard CMOS sensor. This integration is done at wafer level, where a wafer contains multiple image sensor chips, as shown in (Figure 1-12). These filters are Fabry-Perot filters (Perot et al., 1899), (Gonzalez et al., 2016), consisting of a transparent layer (cavity) with two mirrors at each side. The central wavelength of the filter will be mostly determined by the thickness of this cavity layer. The integration of these filters on the image sensors at wafer level heavily reduces the cost and improves the compactness of the hyperspectral camera.

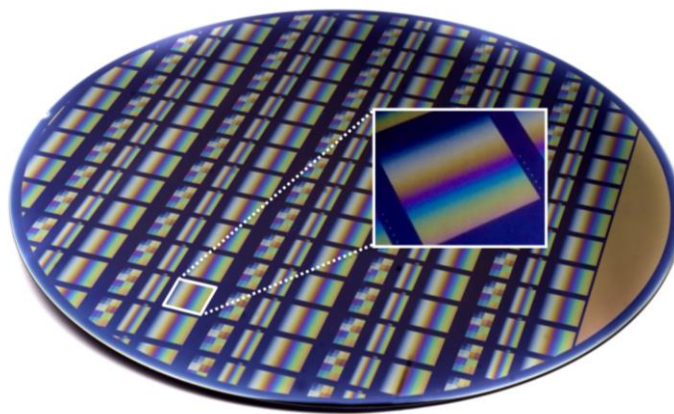


Figure 1-12: IMEC hyperspectral filter structures processed at wafer-level on top of commercial CMOS image sensor wafer (here on CMOSIS’s CMV2000 & CMV4000 sensors) - Courtesy of Imec.

This filter processing technology is based on a wedge-based, or in other words staircase-alike, filter structure. Moreover, the processing technology used allows pixel level accuracies in filter alignment. Thanks to this, the filter layout (covering different groups of pixels or depositing filters per pixel) and performance (i.e., bandwidth, FWHM, etc) can be customized to match the requirements of specific applications. The result is a compact and fast hyperspectral imager made with low-cost CMOS process technology. This technology has been demonstrated with three specific instances:

- A wedge-based **line-scan hyperspectral imager**: this is a spatial-spectral acquisition system offering 100 spectral bands in the range of 600-1000 nm or 150 bands in the 470-900 nm wavelength region (Gonzalez et al., 2016).
- A **tiled snapshot imager**: 32 spectral bands in the range of 600-1000 nm and also with FWHM of each band around 10 nm. An optical duplicator is required in this case, such as microlenses that duplicate the image onto their corresponding 32 filter tiles (Geelen et al., 2013).
- The **mosaic snapshot imager** (Geelen et al., 2015): in this sensor, the filters are arranged onto individual pixels, on a 5.5 micrometer pitch, extending the traditional Bayer color imaging concept to multi- or hyperspectral imaging at video-rates without the need for dedicated fore-

optics or linear scanning. Two mosaic sensors are available: a VIS (470-620 nm range) with a 4x4 filter repeated configuration (therefore 16 bands) and spatial resolution of 512x276 pixels, and a NIR (600-1000 nm) with a 5x5 configuration (25 bands in this NIR range) and a spatial resolution of 410x218 pixels.

Some of the already mentioned characteristics for the different sensor types are summarized in Figure 1-13:



Figure 1-13: Illustration of the different hyperspectral sensors developed by IMEC with their spatial and spectral characteristics – Image Courtesy of Imec.

The wedge layout enables the acquisition of hyperspectral images with high spectral and spatial resolution, while tiled/mosaic layouts inherently dictate a trade-off between spectral and spatial resolution. As a result, both designs will enable a different set of target applications.

The wedge layout, where the filters are arranged in a staircase-like structure over the pixel array, is useful in applications where the scene of interest has a natural translation movement (e.g., in a conveyor belt) and the hyperspectral imager will be used as a line-scanner. An application example with the wedge layout sensor is given in (Blanch et al., 2017) where a line scan camera in the visible-near infrared range is used for accurate prediction of chemical features in bones. In (Blanch et al., 2016) the same camera is showcased for textile discrimination in a recycling application.

An alternative design is a tiled layout, in which filters are laid out in rectangular or square shapes on top of (groups of) pixels. This tiled layout or mosaic layout is useful in applications where the scene of interest has objects that are dynamic or have random movements or that require **snapshot video acquisition**.

The Snapshot Mosaic cameras enable a different range of applications where no scanning can be performed such as biomedical or surveillance applications. This way, in (Li et al., 2017) a compact Mosaic camera with 16 bands in the visual range was used for retinal imaging at 20fps, enabling potential applications for monitoring of retinal diseases. In (Xiong et al., 2019) the same Mosaic camera is used for a video surveillance application, where material-aware object tracking was showcased. In (Farooq et al., 2019) this Mosaic camera was used in combination with neural networks to achieve multi-resolution lawn weed classification.

Generally, snapshot Mosaic cameras such as (Geelen et al., 2015) offer lower fidelity than line-scan sensors such as (Gonzalez et al., 2016). This is due to the mosaic filter pattern and the crosstalk between these closely placed filters (Hahn, R. et al, 2020). On the other hand, snapshot Mosaic cameras provide an increased acquisition speed and are suitable for dynamic scenarios.

In addition to previous camera systems, a new camera system concept for on-chip line scan sensors: the 'Snapscan' (Pichette et al., 2017) was introduced in 2017. This camera offers simultaneously the benefits of line scan (featured with high-speed image quality) and snapshot technologies (no translational movement required). The Snapscan camera system illustrated in Figure 1-14 is a camera system with the high spatial and spectral resolution of linescan hyperspectral imaging technology, namely 7Mpixels and 150 spectral bands. In addition, thanks to its internal translation stage, it provides the ability to acquire datasets as easily as with a snapshot camera. It provides the high spectral and spatial resolution of linescan sensors, without the need for any external scanning movement: scanning is handled internally, using a miniaturized scanning stage. Full hyperspectral images can be acquired in a few seconds. Currently, the maximal RAW spatial resolution that can be reached is 3650 x 2048px (7Mpx), with a spectral resolution of 150+ spectral bands within the 470-900 nm (visible to near-infrared, VNIR) wavelength range.

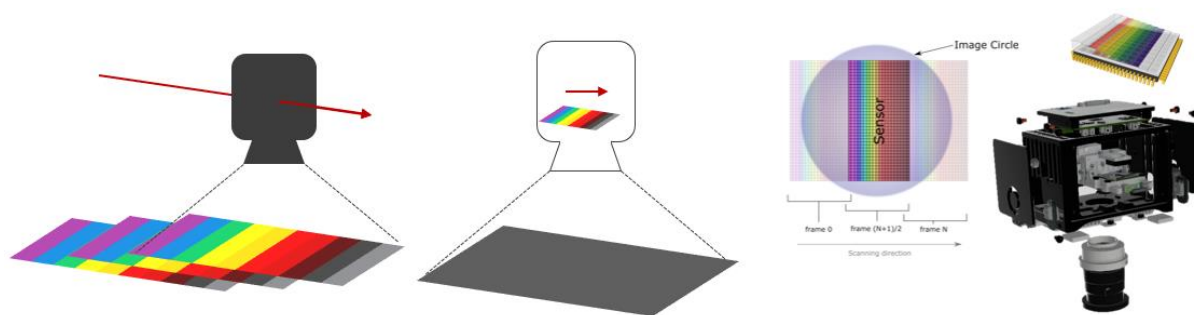


Figure 1-14: Schematic illustration of a traditional linescan imaging system (left) and the Snapscan system with internal scanning (middle and right) – Image Courtesy of Imec.

One of the advantages of internal scanning is that it is straight forward to combine this camera with a microscope setup. This way, in (Chen et al., 2019) a Snapscan camera in the 470-900 nm range has been successfully used in combination with a microscope setup to discriminate live and dead human ovarian cancer cells in a non-destructive way.

The on-chip hyperspectral imaging cameras have extended the visual-near-infrared range to cover the short-wave infrared (SWIR) range between 1100 and 1650 nm (Gonzalez et al., 2018). Similarly, Mosaic SWIR snapshot cameras have also been developed to extend this measurement concept to the SWIR range (1100-1650 nm).

In this respect, “on-chip” hyperspectral cameras, (Pichette et al., 2017), (Geelen et al., 2015), have the potential to considerably reduce the technology cost since they can be mass produced and their price scales down for high order demands.

Other advances in hyperspectral imaging cameras

Traditional hyperspectral camera manufacturers such as Specim (Herrala, 2020), have also developed more compact and portable hyperspectral cameras while still relying on push-broom technology (Behmann et al., 2018), (“Hyperspectral imaging market”, 2018).

In (Oehlschläger et al., 2018) the snapshot camera Cubert UHD 185 Firefly with 125 bands in the 450-950 nm range and a 50x50 pixel resolution has been introduced and evaluated for a remote sensing application, where accurate yield prediction of barley fields is shown. In (Bareth et al., 2014) the authors show another remote sensing application where the same compact snapshot camera achieves comparable NDVI results than a field spectrometer for crop growth monitoring.

In (West et al., 2019) the authors give an overview on the currently available Snapshot hyperspectral imagers on the market enabling its adoption by consumer market as well as its expansion in application fields such as medical imaging, forensics, and remote sensing. Snapshot devices such as the Snapshot Mosaic cameras (Geelen et al., 2015) or the PixelCam camera from Pixelteq (PixelCam) are discussed. An overview of the different commercial Snapshot camera characteristics and their prices is given, where we can see that hyperspectral cameras are becoming more cost effective.

In general, the development of snapshot cameras has helped increase acquisition speed and reduced the camera size and cost. However, the high cost and processing requirements for the large high and complex data seem to remain the limiting factors slowing down industrial adoption (“Hyperspectral imaging market”, 2018).

As previously mentioned, one of the advantages of the “on-chip” hyperspectral technology is that it can potentially be mass-producible, which could considerably reduce the cost of hyperspectral cameras. Another advantage is that cameras can have a smaller form factor since traditional optical elements such as the grating prism are substituted by filters deposited on the sensor. Note that small and light weight cameras are of key importance for UAV remote sensing applications since low weights increase the flight time. Theoretically, a transmission efficiency close to 100% can be expected from thin-film filter technology for CVF (Pust, 2016), (Geelen et al., 2015). This potentially allows lower integration times and therefore faster acquisition speeds, which helps reach industrial inspection speeds. Finally, its production process provides high flexibility in terms of customization and band distribution over patterns of pixels.

Unfortunately, the “on-chip” technology presented also has some disadvantages, such as a certain degree of sensor variability in the production process, which is addressed by adding redundancy in the design (Tack et al., 2012). Moreover, Fabry-Perot filters can suffer from higher-order responses (Tack et al., 2012), (Geelen et al., 2013) which produce a parasitic response at undesired wavelengths. In practice, this is addressed by restricting the spectral range to only those wavelengths free from higher-order responses. In addition, while the theoretical transmission efficiency is of 100%, this is not yet the case for the full transmission range (Tack et al., 2012). Finally, Fabry-Perot filters are lower complexity filters in comparison with those offered by the technology in (Pust, 2016). They offer higher flexibility in terms of filter arrangement and allow implementation of mosaic patterns, but this comes at the cost of reduced out-of-band blocking capabilities (Pust, 2016). It is important to note, nevertheless, that this is a relatively recent technology, which is still undergoing substantial technological improvements.

Trade-offs in hyperspectral camera hardware

As discussed in the previous sections, several technological advances in hyperspectral imaging cameras and sensors have been made during the last decade bringing hyperspectral imaging closer to industrial requirements in terms of lower cost and size factor, and higher acquisition speeds. However, this involves different tradeoffs at system level as shown in Figure 1-15. Developing hyperspectral camera systems of lower cost and higher acquisition speed typically comes at the expense of a lower number of available spectral bands, spatial resolution, SNR or sensor sensitivity, compared to high-end hyperspectral cameras.

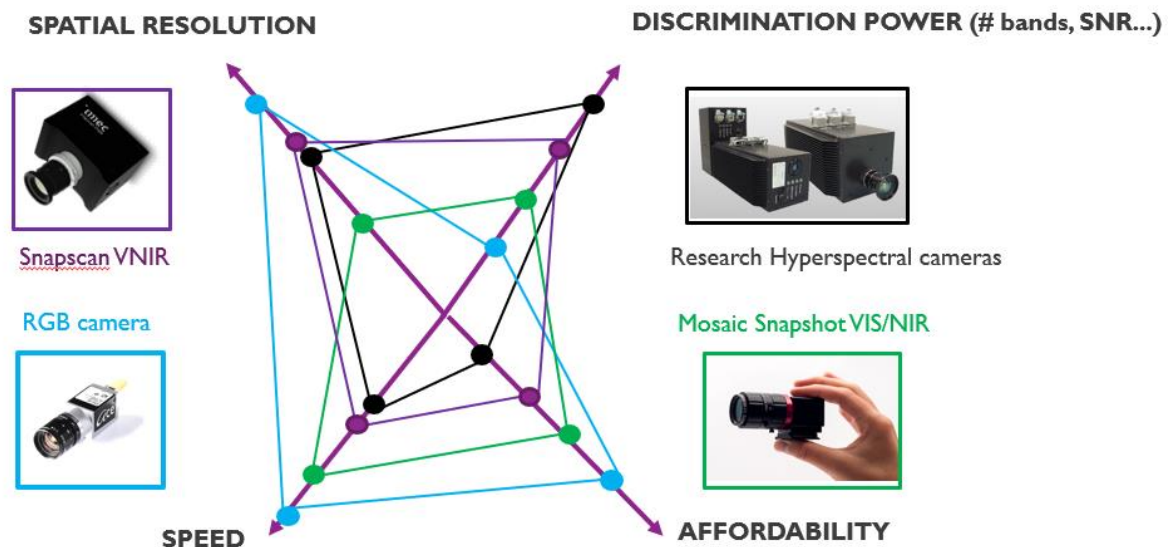


Figure 1-15: Schematic illustration of the hyperspectral camera tradeoffs

Nevertheless, the high discrimination power available in high-end scientific cameras may not be required to meet the requirements of some industrial applications. In this respect, having a camera device, which just meets the application requirements in terms of discrimination accuracy while still offering a good tradeoff in size, cost and speed can be preferable. Moreover, at system level it may be possible to compensate for a lower discrimination power by shifting the efforts to other system aspects. This way, to meet the application goals with faster cameras with lower SNR, more effort can be invested for instance in the post-processing or analysis methods. Similarly, to compensate for the lower spatial/spectral resolution available we could for instance better exploit the spatial information in the image rather than relying on individual and very discriminative point spectra.

The different camera systems presented offer different trade-offs with respect to spatial and spectral resolution, cost, and acquisition speed. This is generally the case between line scan/snapscan and mosaic snapshot systems. While line scan systems provide the highest spatial and spectral resolution available but require sequential scanning, snapshot imaging systems need to trade off some of the existing spatial and spectral resolution to achieve a higher acquisition speed or even video rates. We illustrate these different system trade-offs in Figure 1-15. In the VNIR case both available spatial resolution and camera system cost tend to be correlated.

Similarly, in the mosaic sensors a trade-off is made between the number of spectral bands and the spatial resolution available per band on the sensor. This way, the Mosaic VIS sensor capturing 16 spectral bands has a 512 x 272 spatial resolution, while the Mosaic NIR sensor captures up to 25

spectral bands and therefore offers a reduced spatial resolution of 410 x 218 pixels from the original sensor size of 2048 by 1088 pixels.

In addition, comparing different wavelength ranges such as visual-near infrared (VNIR in the 400-1000 nm range) and short-wavelength infrared (SWIR in the 1000-1700 nm range) different tradeoffs are offered as well. The SWIR range may offer more discrimination power than VNIR for specific applications, but this comes at an increased sensor cost. Moreover, they typically offer lower spatial resolution (VGA of 640x480 pixels) than the corresponding VNIR sensors.

The Devil's triangles corresponding to a hyperspectral application are shown in Figure 1-16. On the left the requirement triangle is shown, where achieving for instance high performance is generally going to increase either system cost or complexity. As mentioned before, an application may be implemented in the VNIR range or in the SWIR range, where for instance higher performance may be achieved incurring in higher system cost. On the right side a devil's triangle on performance is shown. Three aspects can be considered in terms of performance: discrimination power, spatial resolution, and acquisition speed. Typically, for the highest discrimination power and spatial resolution the acquisition speed will be lower. Similarly, for a higher acquisition speed a tradeoff must be made in discrimination power (number of bands) and spatial resolution. One example is the use of Mosaic Snapshot cameras with respect to higher resolution linescan cameras.



Figure 1-16: Devil's triangles for a hyperspectral imaging application (left) and for its performance (right)

In this thesis, we will evaluate how the different components in a hyperspectral imaging system illustrated in Figure 1-5 can be modified/selected to best fit the application and performance requirements in the Devil's triangles mentioned above.

Recent applications of "on-chip" and other compact-form hyperspectral cameras

Research in different areas has been done using on-chip hyperspectral cameras. The fast acquisition of Mosaic Snapshot cameras makes them particularly useful for dynamic applications such as surveillance (Xiong et al., 2019). These compact form factor and light cameras are also being used for remote sensing UAV applications (Lanaras et al., 2018), (Goossens et al., 2018) as well as in the agro sector (Farooq et al., 2019). In addition, both Snapscan and Mosaic cameras have proven to be suitable for medical applications in combination or not with a microscope (Luthman et al., 2018), (Li et al., 2017), (Chen et al., 2019). Finally, they have been evaluated for industrial applications such as textile recycling (Blanch et al., 2016) and for food control applications such as estimation of collagen extraction from bones (Blanch et al., 2017).

In a similar way, the use of portable compact cameras with push-broom technology has been shown in a precision agriculture application (Behmann et al., 2018), where it has been successfully applied to measure plant stress-levels and to detect mildew on barley leaves. In (Bareth et al., 2014) two compact and portable snapshot cameras, suitable for UAV platforms (<1kb) were compared to a spectrometer

spectrally and in NDVI terms for a crop monitoring application (barley canopy) showing comparable results. In (Oehlschläger et al., 2018) the same snapshot camera showed good yield prediction in barley crops outperforming the accuracy of higher resolution RGB imaging.

We can see that newly developed hyperspectral technology starts to be successfully applied in several applications ranging from precision agriculture (Bareth et al., 2014), (Oehlschläger et al., 2018), (Behmann et al., 2018) to medical (Li et al., 2017), (Luthman et al., 2018), (Chen et al., 2019). However, hyperspectral imaging has not yet been widely adopted by Industry. Moreover, current research work does not fully exploit the new trade-offs offered by these industrially oriented hyperspectral cameras. For instance, the use of different cameras is not compared for the same application. In addition, no reports were found on the most suitable illumination systems for snapshot alike cameras.

1.3.4 Hyperspectral image analysis

Hyperspectral image processing tasks can tackle a variety of imaging goals such as material classification, anomaly detection (Chang et al., 2002; Matteoli et al., 2010) or quantification/estimation of a chemical/physical property of the material (Kamruzzaman et al., 2012). In this respect, increasing the discrimination power of our hyperspectral imaging system in Figure 1-16 will generally enable an increased accuracy for any of the mentioned tasks. It will help achieve an increased classification accuracy, reduce the estimation error of a chemical property estimation model or similarly, increase the probability detection of an anomaly. In this PhD thesis we will focus on the aspect of image classification, which suits best the considered application cases.

Aims and challenges of hyperspectral image analysis.

In traditional computer vision with color imaging, the goal of image analysis is to recognize objects in the image to perform a visual task (Wang et al., 2002). Hyperspectral imaging, increases the capability of traditional color imaging by discriminating materials and obtaining more information about its chemical/physical properties, extending the potential targets of image analysis. However, it also introduces new challenges. One of the challenges relates to the high number of bands or dimensions. This results in higher computational cost and can decrease the classification performance, especially in absence of enough available training samples (Feng et al., 2017). For this reason, and since there is high redundancy present among adjacent band responses, methods for dimensionality reduction are usually applied as a pre-processing step in hyperspectral image. These aim at preserving the most relevant information while reducing the data dimensionality (Feng et al., 2017), (Kale et al., 2017).

Another challenge is the high amount of data to be processed, since the increased spatial, spectral and temporal resolution of hyperspectral images creates large 3D data cubes with multiple band responses per pixel. This increases the computational cost considerably (Bioucas-Dias et al., 2013). Finally, the presence of spectral mixing or noise associated to the measurement process makes the analysis of hyperspectral images a complex task (Bioucas-Dias et al., 2013).

The aim of this PhD research was to tackle the main challenges hampering industrial implementation in hyperspectral imaging. Besides the obvious challenge of the cost of hyperspectral imaging systems, which we are trying to deal with by using cost-effective “on-chip” hyperspectral cameras, we will also tackle some of the data analysis challenges introduced. In this respect, the use of lower resolution snapshot cameras results in a lower amount of data to be processed, despite an increase in the associated noise. Similarly, the use of spatial binning in high resolution cameras reduces the amount of data to be processed and its processing complexity, while it may still reach the required performance.

Image processing/analysis involves a series of steps which can be divided into three levels: low level processing, intermediate level processing and high-level processing (Brosnan et al., 2004).

Low level processing includes image acquisition and pre-processing. Image acquisition involves the conversion of the imaging sensor signal into a numerical form. Image pre-processing refers to the processing of the raw image for correction of some spectral distortions, such as, for instance, reflectance correction, spectral correction, or removal of noise. The aim of pre-processing is to improve the image quality or image SNR by removing image distortions or noise or by enhancing the features of interest. Typical pre-processing steps, which rely exclusively on spectral information, are for instance Standard Normal Variate (SNV) (Barnes et al., 1989), Multiplicative Standard Correction (MSC) (Helland et al., 1995) and Savitsky Golay smoothing (Savitzky et al., 1964). Many of these techniques come from the field of chemometrics where typically, point spectroscopy is used, and no spatial information is available and therefore exploited. Other pre-processing steps that reduce noise by considering spatial information of neighboring pixels are spatial binning and median filtering (Gonzalez et al., 2002).

A different type of pre-processing methods is feature selection. One type performs relevant band selection since this reduces redundancy in the spectra and can increase the performance. Some example methods are Principal Component Analysis (PCA) (Smith, 2002) or Linear Discriminant Analysis (LDA) (Naes et al., 2004). While PCA derives new variables as orthogonal linear combinations of the original variables which capture maximal variance, LDA obtains new variables from linear combinations to obtain maximal class separation. In this respect, variable reduction is much more important when it comes to hyperspectral signals than in traditional color imaging. This is due to the high redundancy present between contiguous wavelengths.

Noise removal can be implemented on the raw image as well as on the classified image. We will refer to post-processing as one type of low-level image processing with the aim to increase the quality of the classified image. Some methods that fall into this category are for instance median filtering (Gonzalez et al., 2002) and bilateral filtering (Tomasi et al., 1998). Both methods use the information from neighboring pixels.

High level analysis/ processing involves the recognition and interpretation of the image captured. This is typically done using statistical classifiers or artificial layer neural networks. These are the final processing steps that provide the required information to perform specific visual tasks. While some high-level analysis methods rely purely on the spectral information per pixel, some others exploit the spatial information available in the image as well. Therefore, classifiers can be categorized according to this into pixel-based (spectral-based), object-based and image-based (or spatial-based) (Oliveri et al., 2019). In traditional color imaging, typically object recognition is performed with image-based/spatial-based analysis. Therefore, not only the intensity level per pixel is used but also the spatial relation between pixels: object shape, texture, context, and geometrical properties (Brosnan et al., 2004). In contrast, in the field of spectroscopy many chemometric tools were developed for pixel-based analysis of multivariate signals. Since hyperspectral imaging offers both pixel spectral information and spatial information the analysis methods applied were inherited from both color imaging and spectroscopy analysis methods.

Pixel-based analysis

Pixel –based processing methods are those machine learning classifiers that work based on each individual pixel spectrum. This way, the discrimination/classification is done based on the spectral information per pixel and disregarding the spatial information in the image. Typical pixel-based classifiers are Linear Discriminant Analysis (LDA), Quadratic Discriminant Analysis (QDA) (Naes et al., 2004), Spectral Angle Mapper (SAM) (Kruse et al., 1993) and Support Vector Machines (SVM) (Hsu, C-W et al., 2016).

Boelt et al, 2018 used linear discriminant analysis for the discrimination of sugar beet seeds in maturity levels and reported discrimination with 95% accuracy. Mahesh et al, 2011 showed that five Canadian wheat classes could be discriminated by quadratic discriminant analysis at 82-99% accuracy, independently of its moisture levels. Similarly, QDA could classify moisture contents with accuracies of 91-99% independent of the wheat class.

In addition to these classifiers, Support Vector Machines are another common choice as pixel-based classifier. SVM is based on statistical learning theory and one of its main advantages is that it can offer high performance even when few samples are available for training. For this reason, it has been widely used in remote sensing applications (Melgani et al., 2004), (Camps-Valls et al., 2005), (Chen et al., 2013). In (Guo et al., 2019) the authors show that a combination of SVM with a guided filter further optimized the classification map reaching an accuracy over 90% in a remote sensing application. In (Dong et al., 2011), SVMs were combined with a low complexity PCA with the purpose of reducing classification complexity for satellite images. After dimension reduction with PCA, the classification and mapping time could be dramatically reduced while retaining good accuracy. In (Bonah et al., 2020) Support Vector Machines reached over 94% accuracy in bacterial discrimination when combined with Linear Discriminant Analysis (LDA) as pre-processing step and optimal band selection. In (Feng et al., 2019) the authors reviewed several applications in the food analysis and control domain, where SVMs have also been widely used for pixel-based analysis. In this review, (He et al. 2016) showed for instance discrimination of 4 varieties of maize seeds with SVM models achieving an overall accuracy of 98.3%.

In (Park et al., 2007) hyperspectral imaging and Spectral Angle Mapper were used to discriminate the type and source of faecal contaminants on poultry carcasses with over 90% accuracy. In (Petropoulos et al., 2013) SAM is compared with object-based approaches for mapping land use characteristics in remote sensing. Object-based outperformed SAM by over 7% in mean accuracy.

Object-based analysis

One way to introduce spatial information in the classification/discrimination process is to base the analysis on objects instead of individual pixels. In this respect, object-based analysis inherits from traditional color imaging analysis methods (Brosnan et al., 2004) where an image is segmented into objects so that different features (such as width, length, shape, average intensity/spectral value...) can be extracted per object. Segmentation is typically done after creating a virtual image with maximal contrast or a binary image from which objects can be segmented (Sun, 2000).

In this respect, Extended Morphological Profile (EMP) is a technique that has been often used in remote sensing applications where objects have typically distinct morphologies (e.g square for buildings, lines for roads...). Therefore, adding the morphological information of the object to the pixels belonging to the object provides additional information to the spectra, which increases the discrimination (Benediktsson et al., 2005).

Object-based classification can considerably increase the classification accuracy as shown in works by (Trang et al., 2016) where object-based and pixel-based classification schemes were compared in a remote sensing application. Some researchers have proposed methods to increase discrimination power by combining/fusing pixel-based and object-based features such as (Liao et al., 2014), (Gewali et al., 2018) or (Chen et al., 2019). Typically, spectral and object features are stacked together as input vector to for instance SVM classifiers (Gewali et al., 2018), (Chen et al., 2019). In this respect, Liao et al., (2014) suggested that an accuracy improvement around 3% can be obtained with graph-based feature fusion and the SVM classifier when compared to traditional stacking.

Another possible approach is to implement first pixel-based classification and only after this make use of the available spatial information. This was done in (Hu et al., 2018) by applying morphological operations on the SVM classified image, where it increased the pixel-based classification accuracy by up to 10%.

While object-based analysis can potentially increase the accuracy with respect to pixel-based analysis it relies strongly on performing a correct segmentation of the image, which is not a trivial task. Moreover, Object-based methods require a significant computational effort for image classification (Amini et al., 2018). In addition, the quality of the object segmentation is highly dependent on the parameters chosen in the object segmentation method and automation of the parameter selection remains a challenging task (Dragut et al., 2014).

Image-based analysis

We refer here to image-based processing as those algorithms that jointly exploit spatial and spectral information without necessarily being object-specific.

In this sense, approaches combining spectral and spatial information in a true joint spatial-spectral image analysis have recently been exploited. The most recent approach is based on deep learning techniques, and specifically for image analysis convolutional neural networks have been successfully used (Gewali et al., 2018), (Paoletti et al., 2019). A convolutional neural network is a supervised classification approach in which truly joint spatial-spectral analysis can be performed. For every pixel in the image not only a classification label is provided but also the spectra of all surrounding pixels in a block area. In the CNN different convolutional filters can be applied onto the image, each of those filters extracts spatial information of different kinds. Since hyperspectral imaging has an additional wavelength dimension with respect to color imaging, these filters can be three dimensional extracting spectral features simultaneously with spatial features in an input block.

All previous analysis methods, pixel-based, object-based, or image-based have **advantages and disadvantages with respect to each other**. While Convolutional Neural Networks may reach high classification performance, they also have some drawbacks in terms of their computational cost, and lack of insight in the internal classification mechanism (once the CNN reaches 2-3 layers). Moreover, they need a high amount of training data and are easily prone to overfitting due to the high number of parameters to be trained. Traditional pixel-based classifiers (such as SVM, QDC...) are generally simpler to implement and require a lower amount of training data. However, they do not exploit the spatial relation between neighboring pixels and can therefore yield lower classification results.

Recently, several researchers have investigated the added value of deep learning with traditional research cameras as well as with Snapshot cameras (Fotiadou et al., 2017), (Farooq et al., 2019). Although most of the work on convolutional neural networks is related to remote sensing (Chen et al., 2016; Paoletti et al., 2017; Deng et al. 2018), lately more attention has been dedicated to food processing applications as well. In (Al-Sarayreh et al., 2018) a 3D-CNN has been used to detect meat

adulteration with both spatio-spectral features, outperforming a pixel based SVM classification. Wang et al. (2018) used deep CNNs to detect internal mechanical damage of blueberries using hyperspectral transmittance data.

While there is some research that compares pixel-based and image-based methods for specific applications (Liao et al., 2014), no system wide studies were found that compare these analysis methods as well as the impact of pre- and post-processing. Similarly, the most suitable processing method for different camera tradeoffs and the impact of an illumination system have not yet been considered together. Therefore, the relative impact/relevance of each factor in the system is not known as there is no such system study available where all system elements were evaluated together.

1.4 Research goals and thesis outline

So far, the adoption of hyperspectral systems by industry has encountered several challenges, which are also linked to the key elements presented. First, the hyperspectral imaging hardware available is still too expensive and cannot reach the acquisition speeds required by some applications of industrial inspection. Secondly, hyperspectral imaging produces a high amount of data to be processed, where expertise in analysis techniques is often required. Finally, there is a need for more suitable illumination systems, since halogen systems produce too much heat for industrial inspection and light is not homogeneously distributed over the wavelength range to which the camera is sensitive.

We can see from the analysis of the state-of-the-art that there have been new advances in camera developments to try to suit industrial needs such as a reduced cost. This way, on-chip hyperspectral cameras have been evaluated with promising results for multiple applications (remote sensing, agricultural and medical sectors...). There has been considerable development in image analysis methods such as deep learning, which increase the capabilities of hyperspectral imaging applications. However, this increases the required computation power and the required level of expertise to process hyperspectral images. No reports were found on the impact of the lighting system on such snapshot cameras, where illuminating a surface in a homogeneous way becomes more challenging. In addition, little work has been done to explore different camera spatial-spectral trade-offs or different processing and analysis methods suitable for them. Finally, there are very few authors who have considered all these system aspects jointly, identifying their relative impact and determining optimal configurations for each application case.

It is hypothesized here that the illumination is a key factor, even more important and challenging for these snapshot alike cameras, where a whole surface as field of view, instead of a line, needs to be homogeneously illuminated. Moreover, the impact of illumination must be evaluated jointly with other system aspects such as spatial-spectral camera trade-offs provided by different cameras, and pre-, post- processing methods and data analysis methods of different complexity-performance trade-offs. Therefore, a joint and complete system evaluation is proposed to be able to determine the most optimal configurations and trade-offs that meet the application requirements in a cost-effective way. To this end, the different aspects of the full hyperspectral system with on-chip cameras will be investigated. To assess the impact of the different key elements we have described above; we will use two different application cases:

1. A textile sorting application where different textile materials need to be discriminated.
2. A food quality application case, namely ingredient discrimination and quantification in a flour mix, where several seeds and non-seed ingredients need to be classified and quantified.

The textile sorting application was chosen to show the tradeoffs inherent to the choice of wavelength range. Most researchers in literature have focused on textile discrimination in the SWIR range (1000-2500 nm range) (T4T), (Chen et al., 2020), (Mäkelä et al., 2020). We investigate textile discrimination in the visual near-infrared range (400-1000 nm) and show the tradeoffs made to make this feasible.

The reason for choosing the seed ingredient discrimination case is that this application consists of seed and non-seed ingredients, which are challenging in terms of both spectral discrimination (similar spectra and relatively high intra-class variation) and spatial discrimination (small size and heterogeneous in shape). Choosing a challenging application allows us to better assess the impact of a better illumination system, a more advanced analysis technique or a higher resolution camera on the resulting classification accuracy. On the contrary, an easy enough application case, showing high classification accuracy already with a suboptimal illumination system, a low-resolution camera or a

basic classifier would not show the potential of an improved system aspect. The remainder of the manuscript is illustrated in Figure 1-17, and it is organized as follows:

In Chapter 2 we show how an a-priori sub-optimal wavelength range can be successfully used for a textile discrimination application with the benefit of lower cost camera hardware and higher spatial resolution. Since different application scenarios demand different tradeoffs, the camera hardware (snapshot or line scan system) is adapted accordingly. Similarly, we show how the data processing pipeline can be modified to meet real-time constraints in a proof-of-concept implementation.

Chapter 3 shows how the accuracy of pixel-based analysis can be increased by an object-based post-spatial processing step. This allows to meet the goals of a seed quantification application that requires high spatial resolution. Band selection and benchmarking with respect to color imaging is also performed.

Chapter 4 focuses on the impact of different illumination systems and how they can be optimized with respect to on-chip snapshot hyperspectral cameras. This is demonstrated on the same application of seed discrimination used in Chapter 3.

In chapter 5 we investigate trade-offs between different camera systems (high resolution Snapscan, Mosaic snapshots) where different range and spatial-spectral resolutions are available. In addition, this chapter compares pixel-based and image-based analysis and jointly evaluates the impact of pre- and post-processing methods. Moreover, all previous elements are evaluated together with different illumination systems. This combined evaluation of all key elements of a hyperspectral system allows us to derive suitable system configurations and trade-offs for the considered application.

Chapter 6 adds the wavelength range dimension to the system parameters explored in Chapter 5, extending the overall system performance-cost trade-offs.

Finally, Chapter 7 draws conclusions and presents suggestions for further research and implementation perspectives.

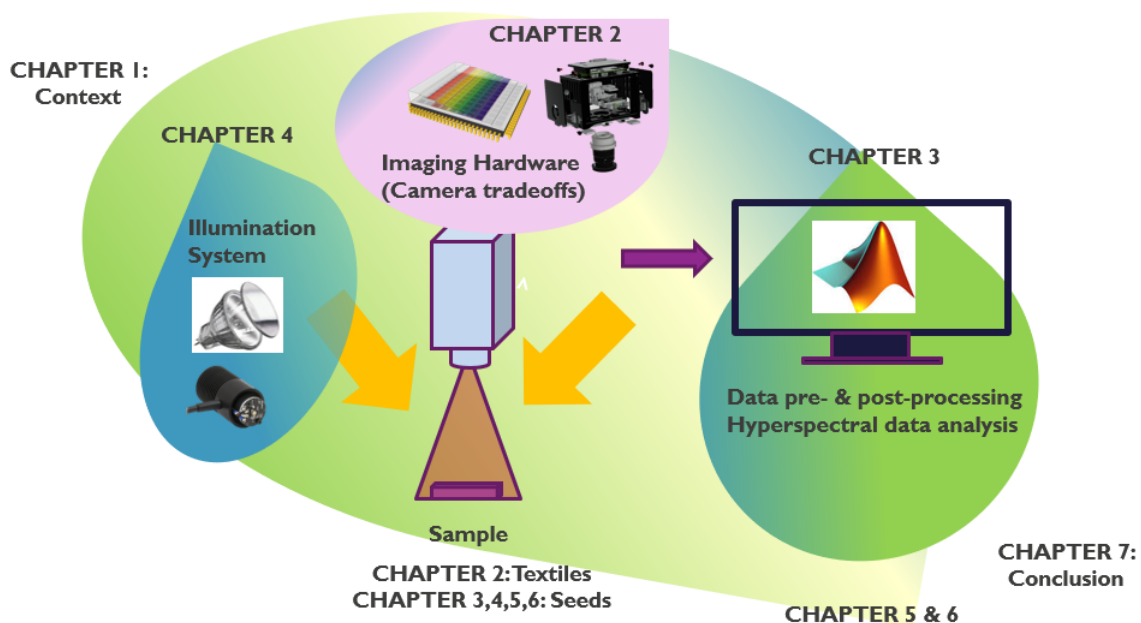


Figure 1-17: Schematic illustration of the topics covered in the different chapters and their interactions

Chapter 2

Wavelength-range as a system parameter in hyperspectral imaging for textile recycling

As it has been introduced in Figure 1-16 of previous chapter, we are generally faced with a Devil's triangle when we intend to meet the application requirements in a hyperspectral imaging system. This means that we cannot optimize all system requirements at the same time. For instance, we cannot maximize performance while simultaneously minimizing system cost and complexity.

In this chapter, an application case is introduced where the aim is to minimize/reduce the system cost while still meeting performance and complexity requirements. We therefore investigate the available system parameters that act upon our application requirements of cost, performance, and complexity.

This chapter shows how the choice of camera hardware, and more specifically of wavelength range, can be the key system parameter to consider when reducing the system cost. An implementation meeting the application requirement in terms of discrimination accuracy may be feasible in different wavelength ranges, offering then different system tradeoffs. In particular, we focus on a textile sorting application, where typically the SWIR range (1000-2500nm) is used. In contrast, we explore the use of the VNIR range (400-1000nm) for this application and show that by trading off some discrimination accuracy we enable other system tradeoffs with lower cost camera hardware in the VNIR range and higher spatial resolution available. To be able to deal with an a-priori sub-optimal wavelength range in this application a different data analysis method had to be implemented, where hierarchical classification is required to meet our application requirements in terms of performance. In a similar manner, we show how tradeoffs are implemented in the processing pipeline for demo purposes. This way, a lower complexity processing pipeline is put in place so that the required performance can still be met while enabling real-time processing in a proof-of-concept implementation. Finally, we introduce a Genetic algorithm-based method for band relevance selection, which provides us with the most relevant bands for discrimination in our last experiment. In this case, with the aim to reduce complexity and potentially enable lower spectral resolution imagers of lower cost.

This chapter is adapted from:

Blanch, C.; Saeys, W.; and Lambrechts, A.; "Hyperspectral imaging for textile sorting in the visual-near infrared range", in *Journal of Spectral Imaging* 8, 2019. <https://doi.org/10.1255/jsi.2019.a17>

2.1 Introduction

The textile sector uses a huge quantity of raw materials and produces a substantial amount of waste. This is partly due to the fact that only a small number of wearable textiles is recycled. Most of these textiles are landfilled or incinerated, with a high environmental impact. The European project RESYNTEX (Resyntex) aims at designing and developing an industrial symbiosis between the unwearable blends (wool, cotton, synthetic polymers) of garment textile waste, and the chemical industry. To enable chemical recycling, sorting of textile material according to material/blend is required first. In this respect Hyperspectral Imaging has a great potential for material discrimination. However, the adoption of hyperspectral imaging by the industry has so far been limited due to the lack of fast, compact and cost-effective hyperspectral cameras with adequate specifications. To bridge the gap between research and industry Imec has developed a unique hyperspectral sensor concept in which the spectral unit is monolithically integrated on top of a standard CMOS sensor at wafer level. This heavily reduces the cost and improves the compactness and speed of the hyperspectral camera, enabling the adoption of hyperspectral technology by industry. Therefore, we evaluate the use of the Imec line-scan 150 sensors (Gonzalez et al., 2016) providing us with 150 bands in the 450-950 nm range for the purpose of textile discrimination. Most of state-of-the-art work on textile discrimination so far has focused on textile sorting in the SWIR range (1000-2500 nm) (T4T), (Fibersort), (Chen et al., 2020), (Mäkelä et al., 2020). We have explored instead the feasibility for textile discrimination in the VIS-NIR range covered by Imec sensors since our VNIR cameras allow for cheaper and more compact inspection devices. In addition to this, we have investigated the potential for sorting blue denim textile with respect to other blue cotton textile since this is a required step for some recycling processes. To our knowledge there is currently no state-of-the-art work on denim discrimination in the VNIR range. In (Yeom, 2014) discrimination in SWIR of pure cotton versus denim is addressed and very few samples are considered. In (Suzuki et al., 2001) and (Morgan et al., 2004) the authors focus on discrimination of single textile fibers with indigo dye and this is done with UV-VIS light in either transmittance (Suzuki et al., 2001) or based on fluorescence (Morgan et al., 2004).

2.2 Materials and Methods

2.2.1 Camera systems

The imaging system used for all tests in this study is shown in Figure 2-1, with an Adimec hyperspectral camera and a translation stage where the textile pieces are placed. The Imec line scan sensor acquires 150 bands in the 450-950 nm range. Its spectral unit is integrated in the standard CMOS sensor at wafer level, which reduces its cost and increases the acquisition speed. This way, for standard halogen-based illumination (325W) the system can reach a speed of 1080 lines per second.

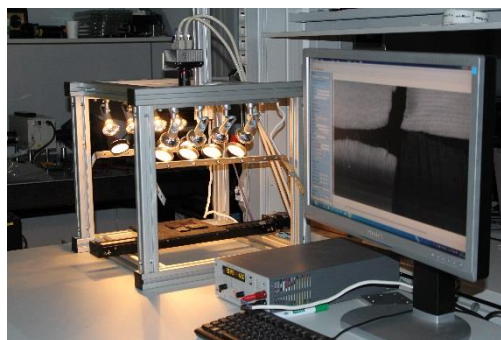


Figure 2-1: Imec hyperspectral system with Adimec linescan camera on translational stage

For the proof-of-concept setup we use the same type of line scan sensor, but this time integrated in a Ximea camera (Ximea), instead of the Adimec camera of the hyperspectral imaging setup of Figure 2-2. The main reason for choosing the Ximea camera in the demo setup is that it connects via USB 3.0 cable to any laptop and does not require CameraLink interface or frame grabber connection to a desktop PC as the Adimec camera. This allows an easier development for demo purposes.

The dimensions of our conveyor belt are approximately 11 by 50 cm, the camera is placed at 70 cm on top of the conveyor belt, with a lens of 35 mm. Next section explains the hierarchical classification method used for textile sorting based on our hyperspectral imaging setup.

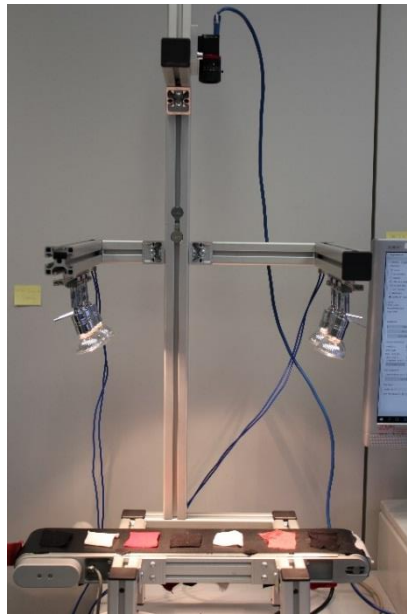


Figure 2-2: Conveyor belt proof-of-concept setup

2.2.2 Materials and methods

This section describes the materials and methods used for the different experimental tests performed. These tests are summarized in Table 2-1 and further explained in this section.

Table 2-1: Summary of tests performed with its corresponding camera system, sample set and analysis method used.

Experimental Test	Camera system	Textile set	Analysis method
Test 1: Reduced textile set	Adimec (450-900 nm)	Set of 50 textile pieces of different materials in 4 colors	Color classification: Lab based and Material classification: QDC/SVM
Test 2: Extended textile set for one color category	Adimec (600-1000 nm)	Set of 100 black textile pieces of different materials	Material classification (SVM)
Test 3: Proof-of-concept implementation	Ximea (600-1000 nm)	Set of 16 textile pieces in black, red and white	PCA + QDC for both color and material classification
Test 4: Denim discrimination	Adimec (450-900 nm)	27 non-denim and 13 denim textile pieces	QDC classification Genetic Algorithm for band selection

Test 1: Hierarchical classification for textile material discrimination

While in the SWIR range the impact of the color tint on the textile spectra is very low, in the VIS-NIR range the color impact is very high. This highly increases the intra-class variability per material type and increases the difficulty for material classification. Figure 2-3 shows how the average spectra of different colors of 100% cotton samples highly varies showing therefore a strong impact of the color tint. We display the reflectance spectra scaled back to its digital number (2 to the power of 10 bits in this case). Similarly, Figure 2-4 shows another example of the strong impact of the textile color on the measured spectra. In this case we show spectra of several textile samples in two color types: red and blue. For each of the colors 3 materials are considered: 100% cotton, 100% polyester and 100% silk. As we can see, the spectra of same color and different material has a more similar appearance than spectra of same material and different color.

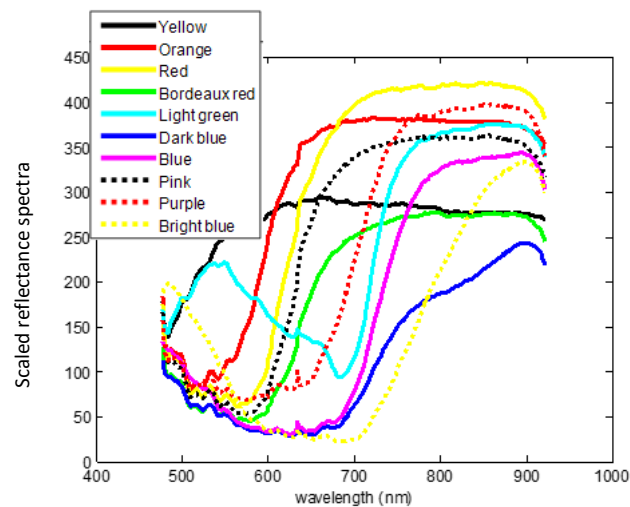


Figure 2-3: Color impact for different colored cotton on scaled reflectance spectra

We deal with this color influence by implementing hierarchical classification, in which color classification is followed by material classification per color category. Therefore, we focus on testing mainly 4 color categories: black, white, blue and red, for which we have samples available for most of the different materials considered (cotton, polyester, wool, viscose, polyamide, silk, acrylic and cotton blends). All samples are extracted from waste textile garments provided by our partner in Resyntex project SOEX (Soex). To facilitate the scan process with our camera system we cut the textile garments received in approximately 5x5 cm samples with the typical thickness of the sample ranging between one and a few mm. Since some of the textiles are thin there can be an impact of the background material on the acquired spectrum of the textile sample. To avoid this, we use a black velvet background material of flat and low spectral response over the whole range. At this stage our set of available samples was rather limited (~ 50 for all four colors altogether), consisting of 1-3 samples at most per each color and material category.

Not only the color tint has a strong impact on the spectra in the 400-1000 nm range, but there is also an impact of the textile material considered in the spectra. This results in the fact that even for identical color there will be differences in the measured spectra (otherwise no material discrimination would be feasible), this phenomenon is called metamerism (“Metamerism (color)”, 2021) and refers to different spectral signatures showing in the visual domain as the same color.

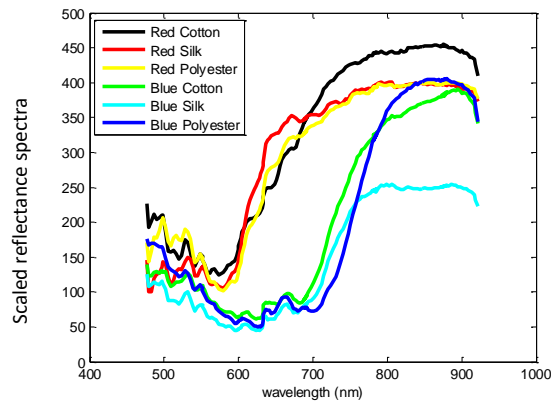


Figure 2-4: Scaled reflectance with combined material and color impact

Due to this metamerism, it is advisable to approach color classification by translating the spectra into three color parameters typically considered for colorimetry: the CIE 'L', 'a' and 'b' parameters ("CIE 1931 Color Space", 2021). These parameters represent all possible colors since they mimic the way our eyes interpret color. The three coordinates of CIELAB represent the lightness of the color ($L = 0$ yields black and $L = 100$ indicates diffuse white; specular white may be higher), its position between red/magenta and green (a^* , negative values indicate green while positive values indicate red) and its position between yellow and blue (b^* , negative values indicate blue and positive values indicate yellow). The L,a,b parameters are computed from the spectral signature as given in the equations in ("CIE LAB"), ("CIE 1931 Color Space"). With these equations the L,a,b values can be computed based on the given spectrum, S , the illuminant function I , (here assumed D65 standard for average daylight ("D65 illuminant")) and the CIE observer functions, x, y, z , ("CIE 1931 Color Space") given by Figure 2-5 corresponding to a 10 degree viewing angle ("CIE Standard Observers"). These observer functions, x , y and z are the numerical description of the chromatic response of the observer, mimicking the tristimulus response of the human eye to blue, green and red colors respectively.

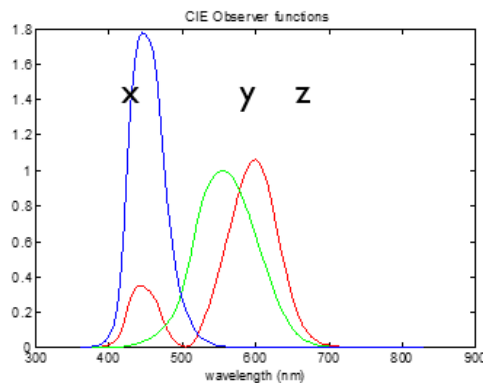


Figure 2-5: Sensitivity in CIE observer functions

Based on the L,a,b values we can then group colors in the color space according to pre-defined color categories. Since we do not have a high variety in sample color content, we choose 18 color categories coming from our training set. The categories selected within the available color samples are: 'Black', 'Grey', 'White', 'Darkblue', 'Blue', 'Lightblue', 'Turquoise', 'Green', 'Darkgreen', 'Bordeaux', 'Red', 'Orange', 'Yellow', 'Pink', 'Fucsia', 'Flesh', 'Purple', 'Darkpurple' and 'Beige'. The purpose of this selection of this high number of colors is to test the accuracy of our color classifier. However, a color classification into a lower basic category may be sufficient to perform material classification afterwards. Color classification is then performed by means of L,a,b parameter computation of the

measured spectrum and selection of L,a,b value with closest Euclidean distance from the colors available in the library.

To do so we first use a training set of different textile colors to build a library. This training set must contain different color samples that are representative for all the color categories identified. The library of Lab values is built by computing the mean Lab value of the textile samples in that category. Finally, to validate this approach, we use a test set with a different set of samples than the ones used as training set. We compute the mean Lab value for each textile piece in the test set and compare it with the available library Lab values. The one with the closest Euclidean Distance (“Euclidean Distance”) is selected as the most reassembling color (or corresponding color label). When a color in the test set is not present in the available color library then the most similar color (in Lab values) will be selected.

After color classification is made, material classification is then performed per color category. From the spectra gathered for each textile sample and color we use 50% as training set for the classifier and the remaining 50% as testing set. Ground truth is available since we only use materials for which we know its composition. We use the Quadratic Discriminant Classifier (Naes et al., 2004) implemented in the Perclass software (PerClass BV 2008-2019). Support Vector machines (Hsu, 2016) also showed similar discrimination capabilities.

Test 2: Extended test for black color category

We have extended previous material discrimination test for one color category: black textiles. We now test a set covering almost 100 different black textile pieces coming from a real and representative waste textile sample of around 1ton of cloth items. In this ton of waste textile, specifically textile garments such as trousers or t-shirts, we found a relative abundance of material, as given in Table 2-2. This means that for example out of the 100 textile samples 33 of them correspond to pure cotton while only 1 to acrylic. The statistic or relative abundance found in these samples corresponds as well with the ones found in literature (Étude de Caractérisation des TLC, 2014) and can be considered therefore representative for typical garment waste. We start testing with black color items since it is expected to be an abundant color in the fashion industry (Bain, 2018).

The material composition abundance among all our samples is given in percentages in Table 2-2:

Table 2-2: Relative abundance in extended black set

Pure	(%)	Blend	(%)
Cotton	33%	Cotton & PET	18 %
Viscose	8%	PET & Cotton	6.8%
PET	4.5%	Cotton & Viscose	3.4%
Polyamide	4.5%	Viscose & PA	2.2%
Wool	2.2%	Acrylic & PA	2.2%
Acrylic	1.1%	Cotton & PA	2.2%
Silk	1.1%	Acrylic & Wool	2.2%
Rayon	1.1%	Acrylic & Cotton	1.1%
Linen	1.1%	Wool & PET	1.1%

In this case, due to the increased number of materials, the classifier that performs best is an SVM classifier with RBF Kernel (SVM, PerClass). Training samples are based on spectral means of 200-pixel regions of every cloth item. The averaging is done in order to reduce the noise level, reduce the intra-class variability and reduce the SVM training time simultaneously. As in previous experiment we train with 50% of the available mean spectra but 12 independent textile samples are also kept for validation

(5 for cotton, 1 for viscose, 1 for cotton & viscose, 1 for polyester, 1 for wool, 1 for polyamide, 2 for cotton & polyester). Since cellulose materials (such as cotton and viscose) are treated together in the recycling process we can group both in a common class.

Note also that cellulose material (cotton & viscose), both as pure and in a blend (often with polyester) accounts for almost 70% of the textile waste. Cellulose is therefore, in pure form and in blend, one of the most economically relevant materials for textile recycling processes. The rest of pure materials such as polyester, polyamide, wool and silk account for around 15% of the total waste and they are as well quite relevant materials for further recycling. Other minor blends (e.g acrylic and polyamide blends with any other material) have very low presence and are discarded from this study due to its low relevance for the recycling processes. Blends of polyamide and acrylic are more difficult to process for recycling and in addition, not economically viable due to its very low abundance. We label all these materials in the 'Other material' category.

Test 3: Proof-of-concept implementation

We show a proof-of-concept implementation with the purpose to demonstrate real-time capability of textile discrimination with hyperspectral imaging. To achieve this, we need a modified processing pipeline better suiting our real-time constraints. We use the hierarchical classification scheme, composed of color classification first and second, material classification per color. To do so, we select a subset of the previously mentioned samples and place them on a small conveyor belt. Due to the limited space on the conveyor belt, we restrict ourselves to a subset of 16 of the previous samples. Figure 2-6 below shows the materials used in the demo and their composition.



Figure 2-6: Textile materials included in the demo set

As already explained, textile sorting in the VNIR range requires a hierarchical classification approach to deal with color interference in the VNIR spectrum:

- Color classification to establish the textile color category
- Material classification within each color category

We add a first additional step which consists in classifying background versus objects. This allows us to later do some filtering or majority count vote at object level, which corrects a few misclassifications on individual pixels. After object discrimination, color classification is performed on the object pixel. Depending on the color label obtained the corresponding material classifier per color category is used. The result is a classifier label indicating a material type regardless of the textile color.

Depending on the classification label attached to each pixel of the image a different color is shown on the screen. The colors used per classified label are green for polyester, blue for wool, pink for silk, yellow for cotton and red for viscose.

Both Lab-based classifier for color classification and QDC and SVM classifiers trained and presented in the previous section for material classification could have been used to classify the textiles in the

proof-of-concept implementation. However, to be able to meet real-time classification in our implementation, we need to adapt our processing pipeline. For this purpose, we skip LAB parameter computation for the color classification stage since this is a costly processing step. Instead, we modify previously presented step in color classification by training a QDC classifier directly from the spectra, to discriminate between red, white, and black color textiles, regardless of the material. For robust discrimination of a high number of colors, LAB parameter computation might be required, but for the three colors considered our simplified pipeline provides an accurate and more cost-effective discrimination, helping us reach real-time constraints. Second, to speed-up classification we use Principal Component Analysis as a preprocessing step for both color and material classifiers. Principal Component Analysis (Smith, 2002) reduces the spectral input dimensionality of the input, which is here mainly required to increase speed performance. This way, as the classification module is implemented on a reduced dimensionality the classification speed increases, helping us reach our real-time classification goal. Therefore, in our proof-of-concept implementation each classifier module consists in Principal Component Analysis extraction followed by a Quadratic Discriminant Classifier (Naes et al., 2004), as implemented in the perClass hyperspectral analysis software (PerClass BV 2008-2019). Training of the classification algorithms is done offline. After training, a combined executable file of the classifier (PCA + QDC) is created so that it can be used inline in the proof-of-concept application. In addition, an object level-based majority count vote is implemented for further accuracy increase.

Test 4: Denim discrimination

Denim textiles are mainly composed of cellulose and constitute around 15% of the total waste stream. Therefore, denim processing is very relevant for the recycling industry.

The most common denim textile is indigo denim, in which the warp thread is dyed, while the weft thread is left white. In the textile recycling process de-coloration of textiles is generally required prior to any further chemical processing of the raw textile components (cotton/polyester/wool...). In this respect, since the indigo dye used in denim materials requires a specific de-coloration process, the separation of blue denim material prior to de-coloration becomes a useful step. For this purpose, we tested the discrimination possibilities as well of VIS-NIR hyperspectral to separate blue denim with respect to any other blue textile types. Note that in terms of composition both denim and other cotton/polyester blends can be very similar.

To test denim discrimination, we have used 27 non-denim textiles and 13 denim textiles. Non-denim textiles are mostly polyester and cotton blends, some very similar in composition to Denim. As in previous tests the samples originate from textile garments (trousers mainly) and are cut to roughly 5x5 cm. Additionally, a black velvet material with low and flat spectral response is used as background to minimize spectral interference from the background. We consider 4 classes: 'Background', 'Denim', 'Other' (i.e blue textile but non-denim) and 'Paper' (label attached to our textile samples). For denim discrimination we train a QDC classifier, since this classifier has shown good performance in previous textile discrimination tests as compared to linear classifiers, with 10.000-pixel spectra per class, out of which 50% are used for training and the other 50% for testing. In addition, we use as independent validation samples 2 pieces of denim textile and 3 pieces of non-denim. For this purpose, they are kept out of the training set.

To find then the most discriminative bands in our wavelength range we use a Genetic Algorithm (Holland, 1992) in combination with our classifier. The aim is to find a near-optimal number of reduced bands providing still high accuracy classification. We use our own implementation of a genetic

algorithm, based on our previous work in (Blanch et al., 2012) and code it in Matlab 2015 (The Mathworks, Natick, MA, USA).

The behavior of the Genetic Algorithm is summarized here and in Figure 2-7:

- For a desired number of subset bands/wavelengths (e.g 3...) an initial ‘population’ of individuals is created. Every ‘individual’ consists of a specific set of random band selections (e.g. [630 nm, 770 nm, 900 nm]). We use a population of 20 individuals where an individual with a uniform band selection over the range is also included in the initial population. This is done to avoid missing any band ranges and make sure that solutions covering the whole range are explored.
- For each individual solution (band selection) the fitness function of the Genetic Algorithm is computed as the mean classification accuracy obtained for that band subset on a fixed training and testing set.
- We use an elitist selection of the fittest individuals, together with the crossover and mutation mechanisms, as described in our previous work in (Blanch et al., 2012). In this case, we use a crossover rate of 0.8 and a mutation rate of 0.6 and we focus on an algorithm optimizing a single objective, given by our fitness function as the mean classification accuracy achieved.

The Genetic Algorithm iterates for a given number of iterations where the best ‘individual’ or band subset is kept. In our case 10 iterations are sufficient for convergence and different runs of the algorithm show good repeatability of results.

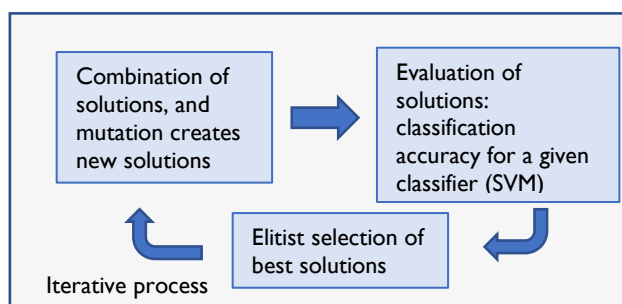


Figure 2-7: Schematics of Genetic Algorithm

2.3 Results and discussions

2.3.1 Test 1: Hierarchical classification for material discrimination

Table 2-3 shows an example of color classification results when applied on a test set of wool materials with a specific Lab value (left column) who gets assigned to the closest Lab value in the library (right column).

Table 2-3: Real color of wool (left) and assigned color classification label based on Lab values (right).

Wool real colour	L	a	b	Classifier label	L	a	b
Black	29.0	-8.0	-7.4	Black	34.5	-12.2	-12.8
Red	58.2	14.3	-17.2	Red	54.2	16.9	-12.9
Light green	60.4	-6.0	02.2	Beige	69.5	-5.9	-4.1
Beige	63.0	-0.7	-4.2	Beige	69.5	-5.9	-4.1
Blue	40.9	-8.1	-10.8	Dark blue	43.1	-7.0	-10.2

The color classification results are generally good. Only for a few colors that are not so well represented in current library there are slight deviations from the actual color and the color label attached by the classifier. This is due to the limited number of categories considered so far. This way, for instance ‘light green’ wool material ends up classified as ‘beige’ (see Table 2-3). Extending the color library to include some lighter shades of green and blue would increase the accuracy of color classification in this case.

For each textile color category, material classification is performed. Figure 2-8 shows the material classification results for a ‘red’ set of materials.

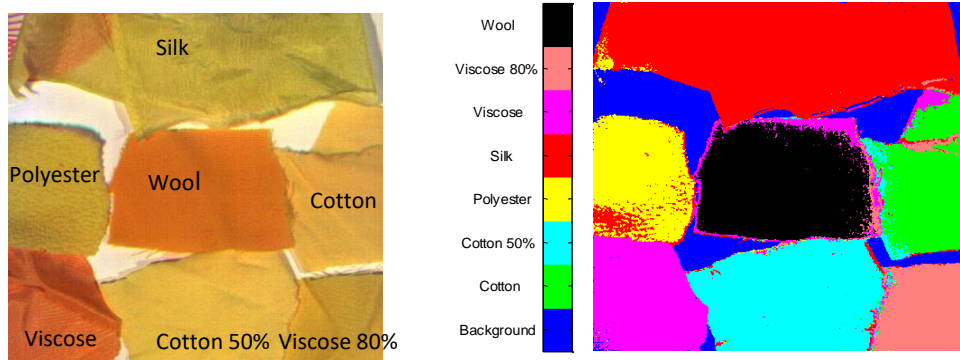


Figure 2-8: False color image of red textiles (left) and corresponding classified image (right).

While at pixel level there are few miss-classifications at object level the classification is 100% accurate. Similar results are obtained for other color categories tested and summarized in Table 2-4 where the classification accuracy per material and color set is indicated.

Table 2-4: Material pixel classification accuracy per color

Color set	Black	White	Blue	Red
100% Cotton	100%	93%	92.5%	91.5%
100% PET	100%	95%	100%	95%
100% Wool	100%	100%	90%	95%
100% Viscose	97.5%	100%	-	92.5%
100% Polyamide	100%	100%	75%	100%
100% Silk	100%	100%	90%	100%
100% Acrylic	-	90%	100%	100%
80% Cotton	-	60%	88%	70%
60% Cotton	100%	90%	-	85%

2.3.2 Test 2: Extended test for one color category

When inspecting the spectral signature of different black materials, we first notice that some pure and blend materials have an unusual and very low reflectance along the whole VNIR range. Figure 2-9 shows such an example where the spectral signature of multiple black cotton samples is compared. Note that cotton item 11 has a distinctively low reflectance spectra as compared to all other black cotton samples. We observe this phenomenon in less than 10% of the samples of cotton/viscose/cotton blend. The reason for this different signature is not known although it is also found in literature and treated as outlier (Haran, 2008). It is not due to the impact of the background underneath, but one possible explanation could be the dye applied onto the cloth item. For the

purpose of the analysis, we consider these materials as outliers that are identified and discarded prior to material classification. Since cellulose materials (such as cotton and viscose) are treated together in the recycling process we can group both in a common class. The trained classifier results in a 100% accuracy of classification for the textile samples from the training set.

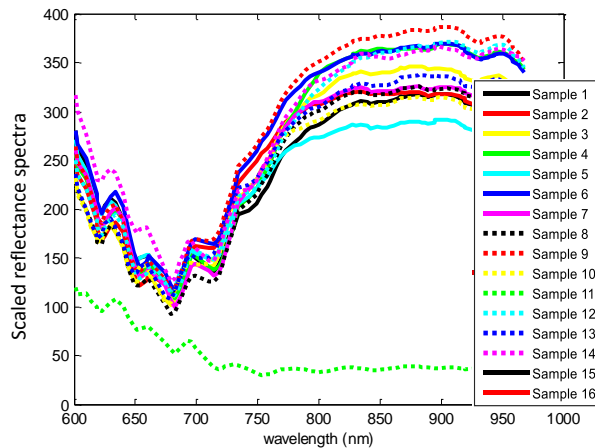


Figure 2-9: Scaled reflectance spectra of pure cotton samples

Figure 2-10 shows a classified image for black textiles in the training set. At pixel level there are few miss-classifications, but we can see that at object level all different materials can be well discriminated. This initial version of the hyperspectral sensor suffered from a bit of ghosting effect at the sides of it. This can be seen particularly at the bottom left corner, interfering with the classification of the cotton and viscose samples.

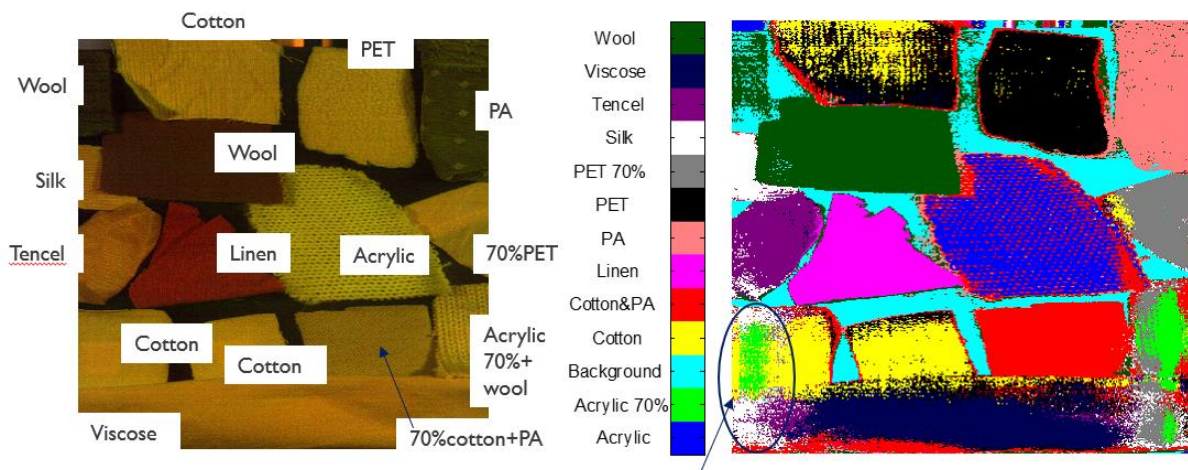


Figure 2-10: False color image (left) and Classified image (right) for different black textile composition. A ghosting effect could be appreciated at the sides of the image in this early version of the sensor (bottom left corner).

To test the generalization capabilities of the classifier we use an independent test set of samples and focus on the most relevant materials for the recycling processes, namely cellulose, polyester, cellulose blends, polyamide and wool. We therefore use an independent test set containing the following materials and number of cloth items: 5 cotton items, 1 viscose, 1 polyester, 1 polyamide, 1 wool and 3 cotton blends (1 cotton/viscose, 1 cotton/pet and 1 pet/cotton). The classification accuracy on the independent test set is shown in Table 2-5:

Table 2-5: Classification accuracy on test set

Test set material	Accuracy (%)
Cotton/Viscose	68%
PET	70%
Polyamide	100%
Wool	100%
Cotton&PET	Miss-classified 50% as cotton and 40% PET
PET&Cotton	Miss-classified as cotton

As we can see, the classification accuracy of most of the samples is reasonably high, especially pure samples. However, the 2 cotton and polyester blends are miss-classified. The cotton & PET blend spectral averages get miss-classified as either pure cotton or pure PET, which is at least consistent with the blend content. The 'PET & Cotton' blend gets miss-classified as cotton. The intra-class variability of cotton & polyester blends may require a higher number of samples within the training set for the classifier to achieve good generalization capabilities.

In this respect, mixed textile classes such as polyester and cotton blends, with either polyester in higher percentage ('PET & cotton') or cotton as main constituent ('Cotton & PET') are considered separate classes, even though they could be considered a mix class where the specific fraction of cotton/polyester could be potentially estimated. For instance, Rodgers et al. (2009) used pre-processing and partial least square regression (PLSR) to estimate the degree of cotton and polyester in textile blends in the SWIR range (1000-2500 nm) with an accuracy over 90%. In our case, we did not have a high enough number of blend samples to perform this kind of analysis. Therefore, and since that sufficed the requirements of our recycling process, we preferred to separate blends in two main groups, those of higher cotton and those of higher polyester content. Another approach to deal with class mixtures would be using soft labels. For example, Come et al. (2008) proposed a model to estimate mixtures based on the use of soft labels where a probability of class membership is assigned.

It is recommended to extend the total number of textile samples considered in this study to obtain a more representative training sample of existing textiles and provide a robust validation. However, we were limited to the available black samples in 1 ton of clothes within one single color category, due to the material discrimination per color category required in the VNIR range.

We leave for future work as well the discrimination within extended sample sets in other color categories (white, blue, grey...) where a more robust discrimination may be feasible than for black color items. In addition, in the textile market we can find combinations of textile blends as well of more than two components (e.g blends of cotton, polyamide and acrylic) which further increases the variability within textile samples. Covering all this textile variability and identifying these blends or its major components would be required to develop a system that can sort all these types of textiles.

Finally, knowledge on the chemical recycling process of the different materials could help us tune the classification scheme. For instance, we know that viscose and cotton are treated together as cellulose material, which therefore can be grouped in the same class. Cotton blends can also be added to the cellulose stream but are initially sorted to better estimate the process yield. Moreover, we know that in the cellulose processing the presence of other textile types such as polyester or cotton blends is not jeopardizing, therefore miss-classifications of other materials into those is not critical, but only affecting slightly the yield estimation. Similarly, the processing of proteins from wool or silk is not affected greatly by other materials. On the contrary, the processing of Polyester or Polyamide requires

a pure flow with no other textiles present. In general acrylics are not processed but should be better removed from the previous flows. Although we can expect lower robustness in the VNIR range (400-1000 nm) with respect to the SWIR range (1000-2500 nm), the VNIR range is still a relevant one since it allows for compact and faster inspection methods. Moreover, we believe it provides better discrimination capabilities than SWIR for denim textiles, as we will explain in the following sections.

2.3.3 Test 3: Proof-of-concept conveyor belt demo

The effect of majority count vote at object level can be seen in Figure 10a/b. This step cleans small miss-classifications present in a few pixels (usually at borders, creases) as seen in the screen shots of 10a and 10b. With the additionally implemented object level majority vote the accuracy becomes 100% on each textile. Without this additional step the accuracy is somewhere above 90% of pixels with correct classification on each textile.

The classification speed of our current demo implementation is around 8 cm/s. This is a fast-enough speed to appreciate the textile pieces moving fast on the conveyor belt while still being able to visualize and control the classified output comfortably.

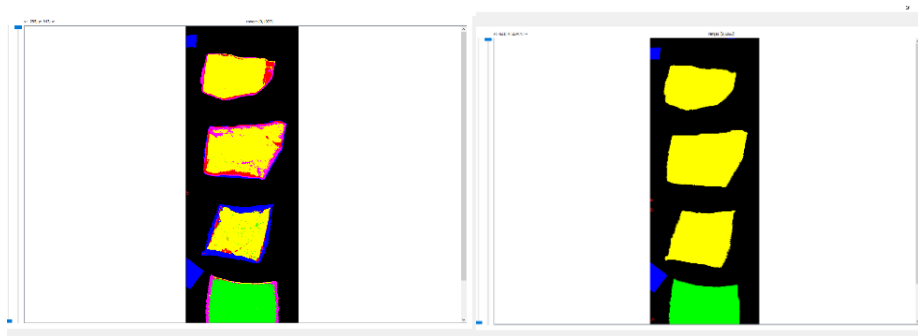


Figure 2-11a and b: Classification output at pixel level (left) and after object-level majority vote (right). Each color indicates a different material class.

However, there is still quite some room for parallelization and memory efficient optimizations. This would lead to considerably higher conveyor and classification speeds since our camera and conveyor belt system can easily deal with up to 80cm/s or 0.8 m/s, which would be enough for processing 1 cloth item/s.

The initial pilot system in the Resyntex project expects to reach speeds of 100kg/h of processed textiles. This is equivalent to 500 tons/year or 1 cloth item every 10 seconds (assuming a 300gr item on average). In the system under preparation each textile item will be processed separately and, according to the acquired spectra, sorted in a corresponding basket by an air-separator system.

2.3.4 Test 4: Denim versus non-denim discrimination

The tests performed to assess the discrimination capacity of VNIR range for blue denim textiles versus all other non-denim blue textiles show that accurate discrimination is feasible. Non-denim textiles are mostly polyester and cotton blends, some very similar in composition to Denim. Table 2-6 shows the pixel classification accuracy obtained in the 470-900 nm range. We train the classifier to discriminate the background and paper label for better visualization of the classified image but show here the accuracy of the relevant classes of denim and non-denim ('Other textile class').

Table 2-6: Model performance for discriminating denim versus non-denim

Test set material	Accuracy (%)
Blue Denim	98%
Other (Blue non-denim)	97%

All 5 textiles in our independent test set (3 non-denim and 2 denim) are accurately classified for over 90% of the pixels. An example of output of a classified textile image is shown in Figure 2-12 with the independent validation denim sample highlighted. Accurate discrimination of denim versus non-denim textiles can be seen, even in cases where the color tint is very similar.

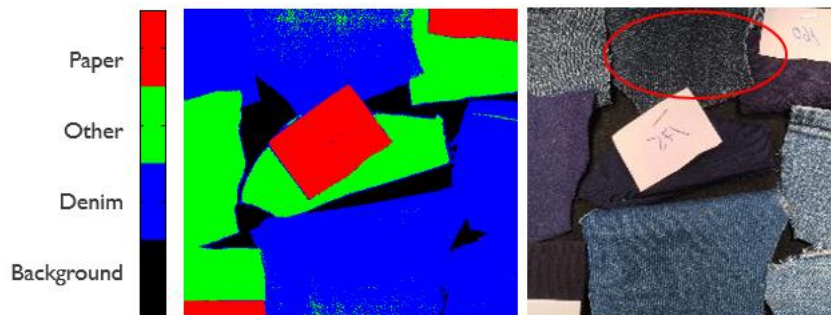


Figure 2-12: RGB image (right) and classified image (left) for denim/non-denim mix

The band relevance study performed with a Genetic Algorithm results in a selected subset of 3 bands (624, 696 and 884 nm) for which a discrimination accuracy of 90% can be obtained for both our denim & non denim set of blue textiles. Note that the found to be most discriminative wavelengths do not belong to the blue range of the spectra (450-595 nm) but closer to the visible range limit (700 and almost 900 nm) and one band in the red range of the spectrum (~ 624 nm).

Higher spectral ranges, such as SWIR going from 1000 nm on to 1700 or 2500 nm are more agnostic from the color influence. This has the advantage of suffering lower or no interference from the textile color and being therefore more robust for material identification regardless of the color. However, in the case of blue denim discrimination this is a disadvantage since the chemical composition of denim is very similar to those of non-denim textiles, namely a cotton and polyester blend where cotton is in higher percentage. This, together with the good discrimination achieved in our tests, makes us believe that the VNIR range is more useful for the step of denim textile discrimination prior to textile recycling processes.

2.4 Conclusions

The feasibility study performed over a variety of pure textile materials (cotton, viscose, polyester, wool, silk and polyamides) and blends (cotton and polyester, viscose and polyester) is promising and seems to indicate that material discrimination can be performed by means of hyperspectral imaging in the VIS-NIR range. Achieving the required performance in this range, which has generally lower discrimination power for this application than the SWIR range, involved using a different data analysis approach. In order to guarantee a robust sorting system for all textiles varieties it is advisable to include a more extensive sample set in the training phase, as well as more textile mixes. In the same spectral range, we have also assessed that good discrimination between blue denim and blue non-denim textiles can be made, which is a required step prior to textile discoloration.

Being able to sort textiles in the VNIR range brings many advantages since it offers higher spatial resolution, cheaper and more compact cameras than the traditional SWIR range. Moreover, the VNIR range enables sorting of blue denim, an abundant and relevant component of textile waste that could be difficult to sort in the SWIR range.

Chapter 3

Exploiting the spatial dimension to increase performance in fast ingredient quantification with hyperspectral imaging

In this chapter, we introduce our second application case: detection and quantification of seed ingredients in a flour mix. This is an offline application case, so cost and complexity requirements are not so challenging in our Devil's triangle. Our priority is to meet the required performance in this application, which is expressed as accuracy in seed count. With respect to the Performance devil's triangle (right of Figure 3-1) we can see that acquisition speed is not a priority here, while discrimination power and spatial resolution are relevant parameters for our quality inspection and quantification of small seeds and other ingredients. For this reason, we choose a high spatial-spectral resolution camera. However, benchmarking with respect to color imaging is still advisable since a color camera might be more cost-effective if performance is not compromised.

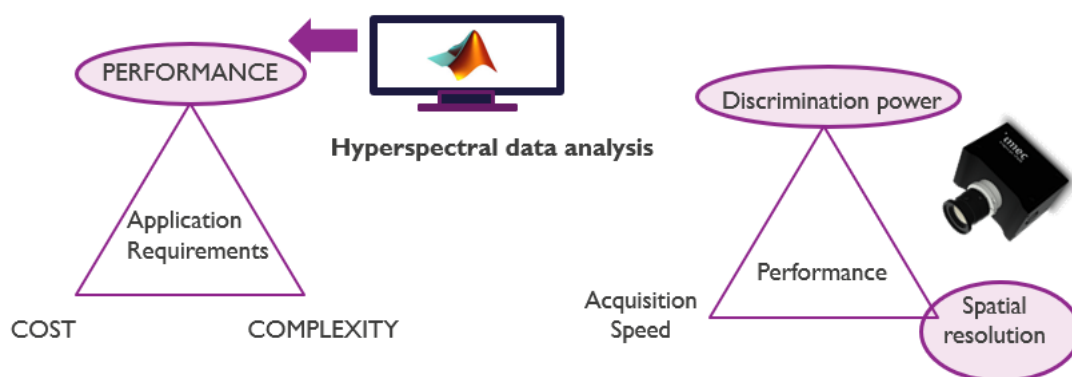


Figure 3-1: Devil's triangles illustrating the trade-offs with respect to application and performance requirements.

An intermediate goal of this application is to have high discrimination power in terms of spectral discrimination to be able to identify the different ingredients. However, the final goal is to be able to accurately quantify each ingredient abundance. Therefore, we need to satisfy the first goal (ingredient discrimination) with just enough performance to meet the final goal (ingredient quantification) with the required accuracy. That means, for instance, that a 70%-pixel discrimination accuracy might be sufficient to meet a 95% seed quantification accuracy. We will also investigate if the use of data preprocessing and the integration of spatial information in additional post-processing can increase the overall system performance sufficiently to reach our application targets.

This chapter is adapted from:

Blanch, C., Saeys, W. & Lambrechts, A. "Fast ingredient quantification in multigrain flour mixes using hyperspectral imaging", in *Journal of Food Control*, vol. 118, 2020.
<https://doi.org/10.1016/j.foodcont.2020.107366>

3.1 Introduction

Multigrain bread is a type of bread prepared with two or more types of grain. Grains used include barley, flax, millet, oats, wheat, and whole-wheat flour, among others. Some variants also include edible seeds in their preparation, such as flaxseed, quinoa, pumpkin seeds, and sunflower seeds. Sharkma et al (2008) have shown that multi-grain bread has higher nutritional value in proteins, fibers, antioxidants when compared to traditional wheat bread. Other researchers have shown that whole grain bread has been shown to have an impact on reducing cholesterol and triglycerides in the body (Giacco, 2010; Talaei, 2013). This makes it a healthy alternative to traditional wheat bread. Due to the uptake of the healthy lifestyle concept, multigrain bread is becoming increasingly popular with consumers and it is becoming a main driver for growth in the bread segment (Bakery products market-growth, trends and forecast 2019-2024).

Flour milling and bread baking have become sophisticated processes with a high level of process technology, high volume, and efficient production. Quality Control, whether on-line or through sampling and laboratory analysis, is therefore becoming ever more important to achieve consistent ingredients, process conditions and products so as to guarantee its nutritional value and maintain customer satisfaction. To this end, several standard quality control methods are described ranging from wheat kernel inspection to chemical property analysis such as moisture or ash content (D. Shelton et al., 2004).

In the case of multigrain flour mixes, it is important to verify that the different ingredients are present in the desired range. This requires the analysis of a subsample of the flour batch where all seed and non-seed ingredients have to be discriminated and then quantified to assess whether their presence in the mix is according to the recipe. This quality inspection is currently done manually, and the procedure involves manual sieving with multiple sieve sizes to separate the different seeds/ingredients and then weight each sorted ingredient independently. This is very time-consuming and as a result only a very small amount of the flour batch is typically inspected.

The commercially available automatic seed counting machines cannot solve this quantification problem, because these devices only measure one seed type at a time. Therefore, to quantify the ingredients in a multi-grain mix with these systems the seeds should be sorted first and measured separately. This is a cumbersome process. Moreover, more heterogeneous and fractionable ingredients such as wheat or barley flakes may not be addressed with these machines.

Machine vision is already widely used for food quality analysis (K. Patel et al., 2012). More specifically, in the flour industry, machine vision with color imaging has been used for cake crumb color analysis according to the type of flour used (F. Rezaghli et al., 2017) or for wheat kernel inspection, and brown versus yellow flax seed sorting (T.C. Pearson et al., 2013). (F. Kurtulmus et al., 2015) reported an accuracy of 84% in the identification of different pepper seed varieties for machine vision with color cameras. Similarly, P.M Szczypiński et al, (2015) classified barley seed varieties based on shape, color and texture features with accuracies between 67 and 86%.

Hyperspectral imaging, combining spectroscopy and imaging, adds an extra dimension to machine vision techniques by providing images at a larger number of more narrow wavebands. Thanks to its higher discriminating power, it is gaining attention as a non-destructive, real-time detection tool for food quality analysis and control (Amigo et al., 2013; H.Huang et al., 2014; D. Lorente et al., 2011). Specifically for flour inspection, it has been shown to provide peanut contaminant detection in flour (A.Herrero et al., 2015; X. Zhao et al., 2018) and measurement of chemical properties such as protein

(Caporaso et al., 2018), sugar or azodicarbonamide (Wang et al, 2018). Most reported studies on flour inspection with hyperspectral technology focused on the SWIR range (1000 to 2500 nm), which contains the most detailed chemical information.

Additionally, the use of hyperspectral imaging in the VNIR range has been shown to increase further the discrimination power for seed quality assessment. Ma et al. (2015) obtained a classification accuracy of 97% for sunflower seed quality inspection with hyperspectral imaging in the VNIR range. Vu et al. (2016) reported that adding VNIR spectral information to shape-based features increased the classification accuracy for rice seed varieties up to 84%. Boelt et al. (2018) reported on the application of hyperspectral imaging for sugar beet seed maturity level discrimination with 95% accuracy. Finally, Carstensen (2018) proposed a spectral imaging system in the VNIR range for discrimination of durum wheat versus common wheat seed reaching 99% accuracy. Most previous studies focused on viability or quality prediction for one type of seed and show the added value of hyperspectral imaging (combining spectral information and spatial/shape information).

Feng et al. (2019) presented an extensive review on existing studies with hyperspectral imaging for seed quality and safety inspection. Most of the reviewed work on seed discrimination with hyperspectral imaging uses the spectra either from ROIs in bulk samples (Zhang et al., 2012, Kong et al., 2013) scanning one seed type per image, or by extracting the mean spectrum from a ROI of each individual seed (Sun et al., 2016). Vermeulen et al. (2018) showed that 99% classification accuracy between durum and common wheat kernels could be achieved by combining spectral and morphological features. Choudhary et al. (2009) and Manley et al. (2011) worked with spectra at pixel level, but with lower resolution imaging in the SWIR range. In all reviewed studies, each image was of a specific seed class/variety and different types were never mixed in one single image. Therefore, the aim of this study was to identify multiple seed and non-seed ingredients in one scan, while the spectra of each individual pixel are used for discrimination.

To be able to accurately discriminate these similar looking seed or grain ingredients it is expected that more spectral information is required than the R, G and B channels used in color imaging. Moreover, we focus here on an industrial inspection application that requires high spatial resolution since we need to inspect sufficient amount of multi-ingredient flour mix (imaging enough seeds/flakes per scan) and this mix often consists of small seeds (e.g poppy, chia...). For this reason, it was assumed that the additional chemical information provided by the SWIR range would not be as relevant as having the high spatial resolution available in the VNIR range.

In addition, for industrial inspection we need high acquisition speed to sample enough product, while retaining enough discrimination power. From previous studies, only Carstensen et al., (2018) addressed fast and high-resolution imaging in the VNIR range. However, this was done for a maximum of 20 spectral bands and to discriminate between only two wheat varieties.

In contrast, in our industrial application we need fast acquisition of multiple seed and non-seed ingredients simultaneously. These seeds will be of different varieties and adjacent to each other, which further challenges accurate discrimination and quantification requiring high spatial and spectral resolution. Moreover, to be able to estimate component abundance in weight we need to assume similar thickness for some ingredients such as flakes. However, in practice, we can expect a variability of around 30% in the flake thickness, as reported for oat (Rosentrater et al., 2018) or for other types of flakes (Mathison et al., 1997), (Schwandt et al., 2017).

To the best of our knowledge our study is the first to focus on the use of hyperspectral imaging for accurate seed type discrimination and quantification in a multiple seed and flake type mix in industrial inspection.

3.2 Materials and Methods

3.2.1 Hyperspectral imaging setup

Figure 3-2 shows the imaging system used: a snapscan camera (Pichette et al., 2017), which offers both high spatial resolution (up to 7Mpixels) and high spectral resolution (150 bands) over the wavelength range of 470 to 900 nm. Thanks to its internal translation stage, there is no need for an external scanning movement. Scanning is handled internally, performing data-set acquisition as easily as with a snapshot camera. Full hyperspectral images can be acquired in less than 10 seconds.



Figure 3-2: Imed Snapscan System with Snapscan camera USB-connected to laptop

3.2.2 Multigrain flour samples

Table 3-1 shows two typical flour formulas that we replicate in our tests. We can see that the most abundant ingredient is wheat flour, while the seed ingredients are present in small percentages. In this respect, the quality inspection of ingredients requires that the estimation error on the mass fraction is below 1%.

Note that the relative abundance of wheat flour cannot be estimated based on a hyperspectral image since no 3D or depth information from the layer of wheat flour can be obtained. Therefore, it was decided to sieve the flour away from the flour-mix. This allows to weight the flour separately and prevents flour from covering other ingredients and making them undetectable for the hyperspectral camera.

Table 3-1a: Composition of flour mix formula 1

Ingredients	Sunflower seeds	Wheat bran	Yellow millet	Red millet	Poppy seeds	Sesame seeds	Brown linseed	Corn crispy	Wheat flour
Percentage(%)	1.75	4.00	2.00	2.00	1.75	2.00	2.00	1.75	84.75

Table 3-1b: Composition of flour mix formula 2

Ingredients	Oat flakes	Cracked wheat	Barley flake	Linseed	Corn crispy	Wheatflour
Percentage (%)	5.00	2.50	5.00	2.50	3.75	81.25

We created five flour mix samples of 5 g for formula 1 by weighting the different ingredients to respect their mass fractions listed in Table 3-1 and b. The error on the weight measurement from our device being around 0.01 gr. We then mixed the ingredients in a petri dish, sieved away the flour and imaged the petri dishes with the hyperspectral camera. For formula 2 we also created five mixes, but in this case, we varied this time the absolute weight of non-seed ingredients. An area of roughly 2000x2000 pixels (4Mpixels) was imaged to match the size of the petri dish. Since some of the ingredients in this application can be very small (such as the poppy seeds), an imager with high spatial resolution is required. Figure 3-4 shows a close-up of a complete image of Formula 1 ingredients in Figure 3-3.

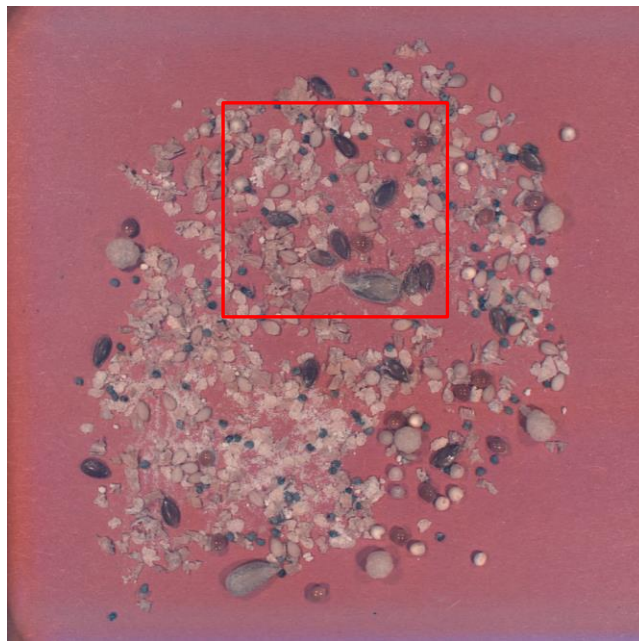


Figure 3-3: Image of Formula 1 with indicated cropped portion for Figure 3-4

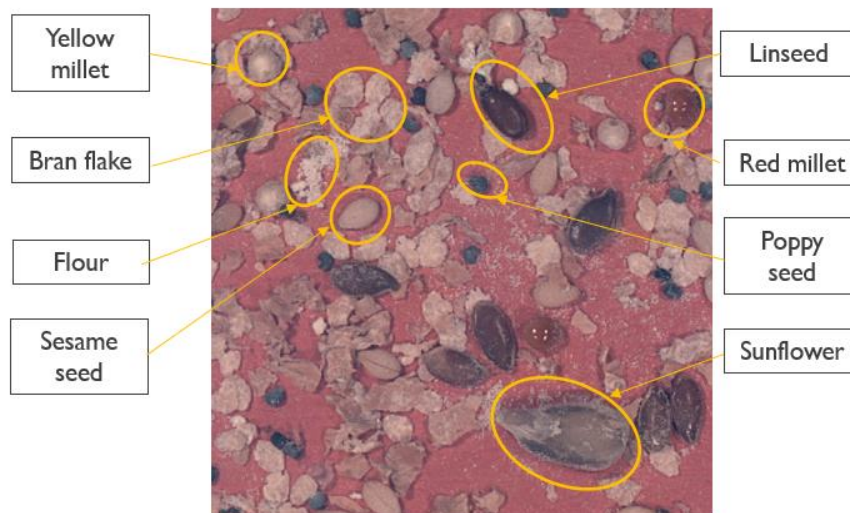


Figure 3-4: Crop of Formula 1 image with indicated ingredients.

As previously mentioned, we have sampled 5 g of formula 1 for every petri dish and used 5 petri dishes per recipe. In this respect, the suitable amount of recipe ingredients to be inspected from the produced formulas is unknown but it depends on the homogeneity degree of each ingredient. In this sense, the more homogeneous the ingredients the lower amount required to achieve representative sampling of it. In our case, the reference implementation for this application is human visual

assessment based on a single petri dish, followed by manual sieving, and counting of each separate ingredient. Therefore, the use of an automated imaging system for discrimination and quantification offers clear advantages: a higher speed automation of the quantification process and with it an increased capacity for product sampling.

3.2.3 Preprocessing and classification methods

We first define a ground truth by creating masks selecting different seed types. From the masks 1000 spectral pixels are randomly selected, corresponding to roughly 20% of the available ingredient pixels in the full image. Out of these 1000 spectra per ingredient type, 50% were randomly selected for training and the remaining 50% for validation. These sets were then used to compare the different feature selection and well-known classification methods in the PerClass software tool (PerClass BV 2008-2019). The classification performance is then validated on the full image and on four independent images.

The number of pixels selected to calibrate our classification algorithm provides good accuracy on all test images provided. In this respect, Zhao et al. (2018) evaluated the impact of the number of samples used for the calibration process in maize seed identification. While in our work each pixel is considered a training sample, in their study, each full seed is considered a training sample for SVM classification. Zhao et al show that although bigger calibration sets increase the classification accuracy on the test set, from a certain size on, 1000 seeds per maize variety in their case, there is no further accuracy increase. In our application, 500 pixels for each different ingredient class was sufficient to achieve high accuracy values on the test set without the need to further increase the calibration set. Nevertheless, we are aware that a lower number of training samples would have not reached the same accuracy on the test set. Similarly, having enough test samples is required to accurately evaluate the generalization capabilities of the algorithm.

As feature selection method we used either none, Linear Discriminant Analysis (LDA) or Principal Component Analysis (PCA) (Smith et al., 2002). For PCA we selected the number of components that captured 99% of the variance, this allowed us to keep 9 PCA components and provided better results than targeting lower variance or higher (100% retains all bands).

The following classification methods available in the PerClass software tool were tested for discriminating the different ingredients based on their spectra:

- Linear Discriminant Analysis (LDA) or Linear Discriminant Classifier (LDC) (Naes et al., 2004), assuming normal densities for our classes.
- Quadratic Discriminant Classifier (QDC), also known as Quadratic Discriminant Analysis (Naes et al., 2004) assuming as well normal densities for our spectral classes.
- Support Vector Machines (SVM) (Hsu et al., 2016): with an RBF Kernel selection and a grid search of sigma and C parameters.
- Random forest (RF) (Yiu, 2019) with the default value of 20 trees, considering a subset of 20% of features at each node
- Artificial Neural Networks (ANN) (Han et al., 2012): a feed-forward network with 30 hidden neurons was selected and 5000 iterations allowed.

3.2.4 Image spatial post-processing

Some of the recipe ingredients such as all seed types (linseed, sunflower, poppy, millet...) are very homogeneous in shape and size. Therefore, both an average number of pixels per seed and an average weight per seed can be estimated for a given camera-object distance, lens type and image spatial resolution. These are summarized in our case in Table 3-2.

Table 3-2: Pixel-weight relation for different seeds

Ingredient	Weight/seed (g)	Pixels/seed
Sunflower seeds	0.03-0.05	3000
Yellow millet	0.0066	330
Red millet	0.0066	400
Brown linseed	0.0066	1000
Sesame seeds	0.0014	400
Poppy seeds	0.0006	120
Corn crispies	0.0175	2000

We used formula 1 (Table 3.1a) to study seed discrimination and quantification, while formula 2 (Table 3.1b) was used to study the quantification of non-seed ingredients. For each formula we used one image for training and four images as independent test set for validation. Non-seed ingredients, such as wheat bran or even barley flakes, are heterogeneous in size and shape. This makes it difficult to obtain an average weight or pixel number. Their abundance estimation will be explained in more detail in the following section.

3.2.5 Estimation of abundance per seed ingredient

Since the seeds are very homogeneous in size and shape, we assume that its abundance in grams can be safely estimated from the number of seeds present in the classified/labelled image. As we will later see, the presence of miss-classified pixels can make the seed count challenging. In order to correct these miss-classifications we perform some additional spatial imaging post-processing step. This step cleans the classified mask images and helps obtain a more accurate seed count.

The additional image processing proposed is done in Matlab 2015 (The Mathworks, Natick, MA, USA) and consists of a combination of the following common morphological operations in this order:

- **Area open:** the operation of area opening removes from a binary image all connected components (objects) that have fewer than P specified pixels, defining the cluster size to be removed. The default connectivity for pixels to belong to an object is 8 for two dimensions.
- **Area fill:** a morphological operation with the purpose to fill small pixel holes in objects/seeds by setting a pixel to 1 if five or more pixels in its 3x3 neighborhood are 1's.
- **Object count:** this operation counts all 8-connected objects (Ghuneim, Pixel connectivity) in the image. With this final step the total seed count is extracted.

The first step in our spatial post-processing consists of removing clusters of miss-classified pixels. Our P parameter tuning allows to specify the object size to be considered as miss-classification and removed from the image. Parameter P is related both to the expected size of the seed as well as to the proportion of expected miss-classified pixels. On one hand, this parameter must be roughly below 50% the pixel size of the target seed to avoid eliminating partially eroded seeds or half seeds present in the image. This is particularly the case for sunflower and linseeds, which tend to fracture. On the other hand, the P parameter must be large enough to safely eliminate miss-classified shades/borders

coming from non-target seeds. This is typically obtained with values around 10-20% the pixel size of the target seed. In the case of sesame and millet seeds, where there are more miss-classified pixels but no fractured seeds, values up to 40% the size of the seed were found to be suitable.

Table 3-3 shows the selected P parameter, found experimentally, and validated over several independent images, where P parameter can be set to 30% of the seed size for sunflower and linseed, while P parameters of 40% the seed size are required for sesame and yellow millet but are also suitable for the remaining seed ingredients.

Table 3-3: ' P ' parameter selection versus average seed size in pixels

	Sunflower	Corn	Linseed	Sesame	Millet	Red millet	Poppy
Average size S	3000	2000	1000	400	330	400	120
P parameter	$0.3*S=900$	$0.4*S=800$	$0.3*S=300$	$0.4*S=160$	$0.4*S=130$	$0.4*S=160$	$0.4*S=50$

The estimation of some seed types requires additional post-processing. This is the case of millet, where a higher number of miss-classifications occur, and an additional step is added to count only circular shaped objects.

- **Find circular shapes:** This algorithm, based on the circular Hough transform, detects circular shapes within a predefined diameter range. For our images, the range was set from 8 to 20 pixels.

Another seed that requires an additional post-processing is the poppy seed. Its spectral discrimination is very accurate, but their seeds often cluster together and can be mistakenly counted as one single object or seed. Therefore, instead of an object count we use in this case:

- **Pixel-count based estimation:** this step divides the total number of pixels labelled as 'poppy seed' by the average size of a poppy seed (here 120 pixels). This quotient provides then a more accurate estimation of the total number of seeds when clustered.

3.2.6 Estimation of non-seed ingredients

The size and shape heterogeneity of non-seed ingredients such as flakes or bran (from oat, barley or wheat) makes it more challenging to estimate the weight/percentile abundance based on the number of flakes or pieces. In this case, considering the number of total pixels labeled as a specific cereal gives a better indication of its actual weight. To do so we assume a similar thickness for these ingredient flakes. Since multiple flakes are imaged simultaneously, we will see that on average a good estimation of the weight in grams can be obtained from the pixel count.

A total of five petri dishes with different abundances of non-heterogeneous ingredients (such as flakes), corresponding to the flour mix in formula 2, were also imaged and then classified. One image was used for training and the remaining four for testing.

3.2.7 Waveband selection

To identify the most discriminative bands in the VNIR wavelength range a Genetic Algorithm was used (Holland, 1992), in combination with our best performing classifier: LDA as feature selection followed by QDC. The aim was to find a near-optimal number of reduced bands providing still high classification accuracy. This information could be used for instance to enable customizing the hyperspectral sensor or alternatively to process less bands and simplify the classification process. We use our own implementation of a genetic algorithm, based on our previous work in (Blanch et al., 2012) and code it in Matlab 2015 (The Mathworks, Natick, MA, USA).

The behavior of the Genetic Algorithm is schematically illustrated in Figure 2-7 of Section 2.2.2.

- For a desired number of subset bands/wavelengths (e.g 3...) an initial 'population' of individuals is created. Every 'individual' consists of a specific set of random band selections (e.g. [630nm, 770nm, 900nm]). An individual with a uniform selection is also included in the initial population.
- For each individual solution (band selection) the fitness function of the Genetic Algorithm is computed as the mean classification accuracy obtained for that band subset on a fixed training and testing set.
- The Genetic Algorithm iterates for a given number of iterations. In each generation (iteration) the best performing 'individual' or band subsets are kept breeding new generations.

Our LDA+QDC classifier is trained on 50% of our random sample selection and tested on the remaining 50%.

3.2.8 Comparison with RGB image discrimination accuracy

To benchmark hyperspectral imaging in the VNIR range (460-900nm) with respect to regular color imaging cameras we create RGB images from our hyperspectral image. This way, we can compare both imaging systems under the same system conditions: illumination, lens, and identical sample selection.

To obtain the corresponding RGB image from the hyperspectral image we use XYZ parameter computation (Goodman, 2012) from our hyperspectral image. The CIE XYZ color space is a device-invariant representation of color. From the given spectrum, S , the illuminant function, I , (here assumed E standard of theoretical equal energy radiator (Goodman, 2012)) and the CIE color matching functions, we can obtain X, Y and Z color values. We can then transform these X, Y, Z values to RGB color components (International Colour Consortium 1999, sRGB).

3.3 Results and discussion

Figure 3-5 shows the mean reflectance spectra of the different ingredients in Table 3-1, where we can see that some ingredients have a visually similar mean spectrum (e.g wheat bran and sesame). Table 3-4 summarizes the classification accuracies obtained for the validation set of said ingredients. The different feature selection and classification methods are compared using the exact same set of training and validation samples.

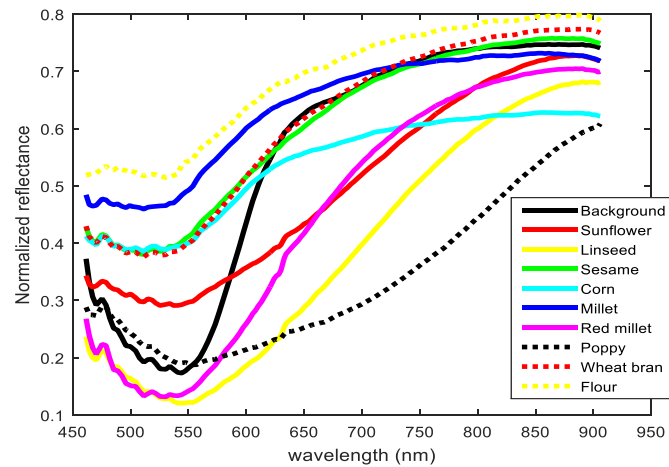


Figure 3-5: Mean reflectance spectra for the ingredients in the seed mixes

Table 3-4: Classification performances at pixel level for different combinations of feature selection and classifier

Feature selection	Classifier	Minimum accuracy (%)	Mean accuracy (%)
PCA	QDC	66.8%	91.8%
PCA	SVM	68.1%	91.4%
LDA	LDC	61.4%	90.3%
LDA	QDC	75.0%	93.0%
LDA	SVM	49.9%	87.6%
LDA	RF	68.6%	92.0%
None	ANN	53.4%	89.1%

We can see that the combination of Linear Discriminant Analysis (LDA) as feature selection step and Quadratic Discriminant Analysis (QDC perClass) as classification method outperforms all other methods in terms of minimum and mean accuracies. It is interesting to notice for instance that PCA as feature selection method provides in this case a significant lower accuracy than LDA as feature selection to QDC. However, for the SVM classifier it is PCA that performs best. While the mean accuracy is comparable for all classification methods, it is for the challenging classes (minimum class accuracy) where we can see LDA+QDC clearly outperforming all other methods. Moreover, its computational time is lower than for more advanced classifiers such as Support Vector Machines (SVM) or random forest (RF). The normalized confusion matrix for LDA+QDC classifier and the seed ingredients given in Table 3-1 is shown in Table 3-5 below.

Table 3-5: Confusion matrix for LDA+QDC classifications of the ingredients in formula 1

	Decisions											
	1:1	2:2	3:3	4:4	5:5	6:6	7:7	8:8	9:9	10:10	11:11	sum
Background	0.99	0	0	0	0	0.00	0	0	0.00	0	0.00	1.00
Sunflower	0	0.98	0.01	0.00	0	0.00	0	0	0.01	0	0	1.00
Linseed	0	0.02	0.97	0	0	0	0	0	0.01	0	0.00	1.00
Sesame	0	0.00	0	0.90	0	0.01	0	0	0.09	0	0	1.00
Corn	0	0	0	0	0.95	0.04	0	0	0.00	0	0	1.00
Millet	0	0	0	0.04	0.13	0.75	0	0	0.08	0.01	0	1.00
Red millet	0	0	0.00	0	0	0	0.98	0	0.01	0	0	1.00
Poppy	0	0	0	0	0	0	0	1.00	0	0	0	1.00
Wheat bran	0.00	0.00	0	0.09	0	0.03	0	0	0.86	0.03	0	1.00
Flour	0	0	0	0	0	0.09	0	0	0.17	0.74	0	1.00

Values shown are fractions of one, where one is equivalent to 100% of the pixels correctly classified. The left column shows real class labels while the upper row shows decisions or labels attached by the classifier. Values in the main diagonal mean correctly labeled samples while values outside the diagonal are miss-classifications between classes. We can see that, although classifications accuracies are generally high (over 75%) pixel miss-classifications can be expected. This way, corn and millet are sometimes miss-classified due to their spectral similarity. This can also happen between wheat bran and sesame. In Figure 3-6, a small crop of the original image acquired for the ingredients in Formula 1 and the corresponding classified image is illustrated. We can see that, after sieving, some remaining small amount of flour may be detected and classified. We can as well observe how small miss-classifications happen on seed parts, especially for millet and corn, which suffer miss-classifications with each other. These miss-classifications interfere with the individual seed recovery/count required for ingredient quantification and need to be corrected by post-processing.

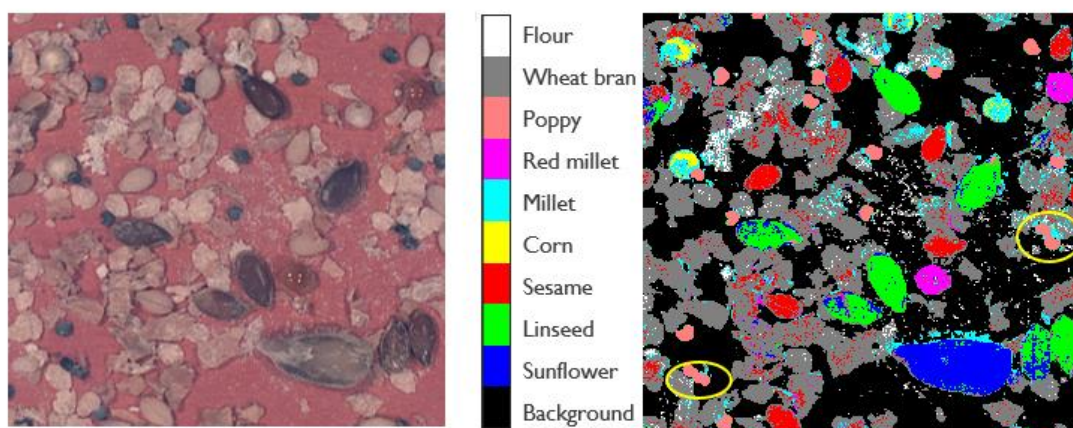


Figure 3-6: Close-up RGB image of a seed (left) and the corresponding classified image obtained with QDC applied to LDA features (right)

Figure 3-7 shows the resulting original and spatially post-processed masks for sesame (top), yellow millet (middle) and poppy seeds (bottom). The middle row shows for instance the mask of pixels classified as millet, where quite some pixel miss-classifications occur. Small miss-classifications are in general efficiently removed by the morphological operations described in Section 3.2.5. We can see now in Figure 3-7 (right) that pixels corresponding to the real seeds (four millet seeds) can be identified

better. Occasionally, however, some seed portions may be eroded away, or a small cluster of miss-classified pixels may persist. In the case of poppy seeds (bottom row), the classification accuracy is already high, and fewer miss-classifications are present. However, to deal with seed clusters, the total pixel count step is required.

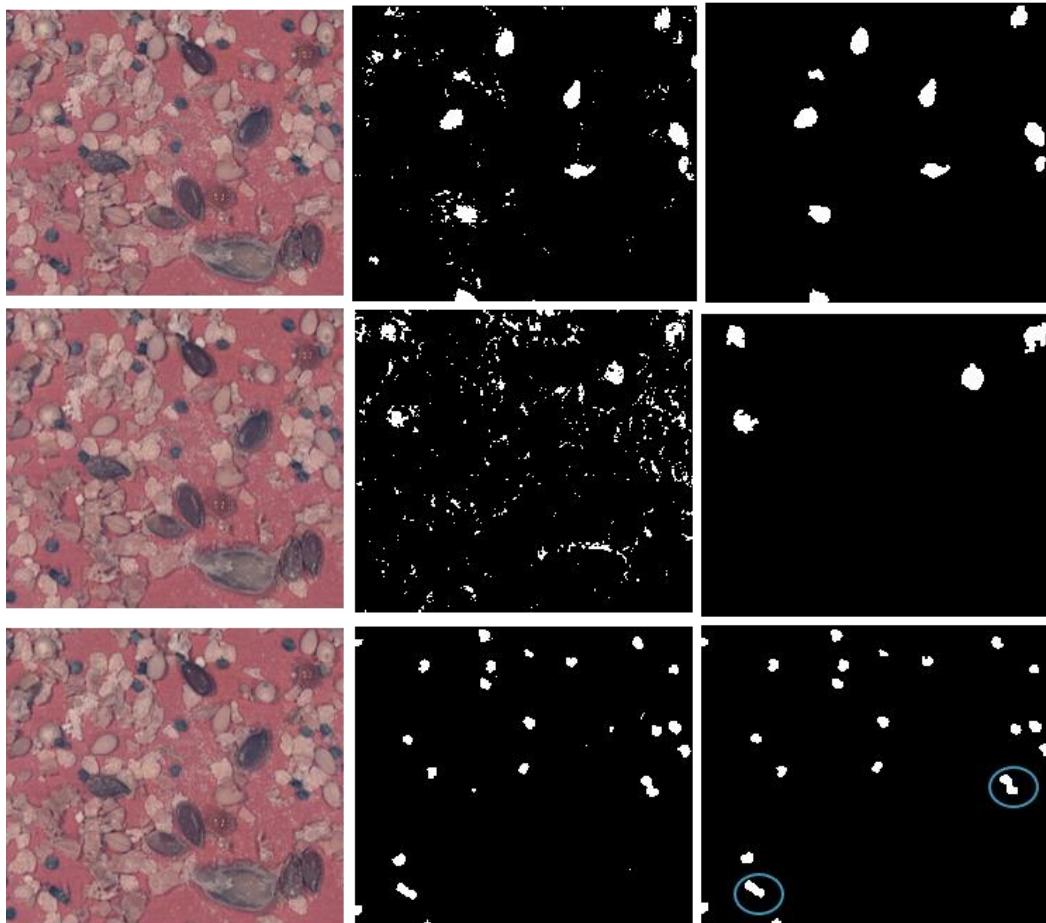


Figure 3-7: Close-up color images of seed mixes (left), with corresponding classification masks (middle) and spatially post-processed classification masks (right) for sesame (top row), yellow millet (middle row) and poppy seeds (bottom row) with circled seed clusters.

Table 3-6 shows the final seed count obtained for the full-size petri dish of Figure 3-6, as well as the abundance estimation errors in relative and absolute terms. The relative error per ingredient has been computed from the number of estimated and actual seeds. For instance, 15 seeds are detected out of the 16 linseeds, resulting in a 6.25% relative error. To compute the absolute error, we considered the specific abundance of linseeds in the flour mix. Since linseed constitutes 2% of the mix, the absolute error has been computed as $6.25\% * 2\%$, which corresponds to an absolute error of 0.12%. We can see in Table 3-6 that yellow millet has the highest estimation error (16% relative error). All other seed types are estimated accurately with relative estimation errors below 10%. Our industrial application requires that the absolute estimation error is below 1%. This way, a seed of 5% abundance in the flour mix can be estimated in the 4-6% range with up to 20% relative estimation error. Therefore, for the ingredients in Table 3-1, all present at a maximum of 5%, we are within the required 1% absolute error even in the case of a 20% relative error.

Table 3-6: Final seed count accuracy for the seed ingredients in Formula 1

Ingredient	Perc (%)	Actual # seeds	Estimated # seeds	Relative error (%)	Absolute error (%)
Sunflower	1.75	2	2	0.00	0.00
Linseed	2.00	16	15	6.25	0.12
Corn	1.75	5	5	0.00	0.00
Red millet	2.00	14	14	0.00	0.00
Yellow millet	2.00	22	26	18.18	0.36
Sesame	2.00	37	34	8.10	0.16
Poppy seed	1.75	113	106	6.19	0.11

Our classification and quantification method, trained on one image, has been validated over four independent test images from petri dishes of the same formula 1. The results are summarized in Table 3-7.

Table 3-7: Final seed count accuracy for the seed ingredients in Formula 1, average over validation dishes

Ingredient	Perc (%)	Relative % error per validation dish				Mean relative error (%)	Mean absolute error (%)
		<i>Dish 1</i>	<i>Dish 2</i>	<i>Dish 3</i>	<i>Dish 4</i>		
Sunflower	1.75	0.00	0.00	0.00	0.00	0.00	0.00
Corn	1.75	0.00	0.00	0.00	0.00	0.00	0.00
Linseed	2.00	0.00	6.25	6.25	6.25	4.68	0.09
Sesame	2.00	5.41	0.00	0.00	8.11	3.38	0.07
Yellow millet	2.00	4.54	22.72	4.54	9.09	10.22	0.20
Red millet	2.00	0.00	8.33	15.38	8.33	8.01	0.16
Poppy seed	1.75	8.84	10.61	6.19	7.96	8.40	0.13

As we can see, all ingredient estimates are below the 1% absolute error required, except for the more challenging ingredient, yellow millet, in one of the test images (dish 2). In this case, a relative error of 22% (higher than 20%) translates in an absolute error above 1% for seeds with higher abundance than 10%. However, typically seed abundance in a flour mix is lower than 10%, in particular for small size seeds such as millet. It is also interesting to note that the relative errors for different images of the same recipe can vary. This is probably related to seed distribution, where some ingredients can end up clustered, occluded or imaged at a different angle. Therefore, by averaging over different images of the same recipe we can also expect to reduce our estimation error, as it can be seen in the mean error over the 4 test dishes in Table 3-7.

By performing hyperspectral imaging followed by spatial post-processing, and averaging over images, we have achieved relative errors below 10%, equivalent to a discrimination/quantification accuracy over 90%. This high seed discrimination accuracy has been reported as well in literature by combining hyperspectral and texture/spatial information. This way, Sun et al, (2016) also found that combining hyperspectral imaging in the VNIR range and spatial information (such as texture/morphology) achieves the highest discrimination accuracy (98% versus 86% for only texture based), for black bean varieties. Similar conclusions are drawn for maize variety discrimination in (Zhang et al., 2012) where combining textural information with VNIR hyperspectral achieves 98.8% accuracy on 100x100 pixel ROIs from bulk samples. Choudhary et al, (2009) showed 99% classification accuracy of 8 wheat varieties by combining wavelet texture features from ROIs with hyperspectral data in the SWIR range (900-1700nm). Manley et al, (2011) assessed the impact of kernel topography on pixel spectra from wheat, barley and sorghum kernels, but no classification results are provided.

In our work we have used a high-resolution imager in the VNIR (4Mpx with respect to 0.3Mpx in previous works) to better image multiple seed types in one scan, instead of one single type (or even one single seed) per image. Sun et al. (2016), Zhang et al. (2012) limited their spectral information to

the mean spectra from manually pre-defined ROIs. In contrast to this, we have used pixel-based spectral analysis.

Moreover, we have combined hyperspectral and spatial/shape information in a different way than previous approaches. In previous works this was done by extracting texture features from defined ROIs covering bulk samples (Zhang et al., 2012) or single seeds (Sun et al., 2016), or by more complex wavelet analysis (Choudhary et al., 2009). Instead, we have done this by applying a few morphological steps such as erosion on the already pixel-based classified image. We have shown that this combination of pixel-based spectral analysis and spatial post-processing can reach high discrimination and quantification accuracy.

Implementing an object segmentation approach can be useful to increase object discrimination, as shown in the work of Gewali et al. (2018) and Chen et al. (2019). Some researchers have included shape information for seed discrimination such as Sun et al. (2016) and Huang et al. (2016), who used morphological/shape features to increase the discrimination power for both black beans and corn, respectively. In those works, each seed was either imaged separately or placed separated from each other to ease the segmentation task. A similar approach could be helpful for some of our seed objects with homogeneous and distinctive shape features, such as millet, linseed, or sesame seeds. However, occasionally these seeds can be partially fractured or occluded by neighbouring seeds, which distorts their shape. Moreover, we have non-seed ingredients as well that are very heterogeneous in shape and size, such as soy grit, soy mill, wheat bran or any type of flake (barley, oat). For this kind of ingredients such a segmentation approach would be more difficult to implement, and the shape features would remain very heterogeneous within a class.

Non-seed ingredient estimation based on pixel count

We related the number of pixels labelled by the classifier as a specific ingredient with its absolute weight in grams. Table 3-8 shows an example of such measured relation for barley flakes and wheat bran in different weights, with a confidence level given for our weight measurement error.

Table 3-8: Corresponding weight and number of pixels for barley (left) and bran (right) ingredients for different images of Formula 2

Formula 2	# pixels (barley flakes)	Weight	# pixels (wheat bran)	Weight
Image 1	91277	0.54+/-0.01 gr	207692	0.11+/-0.01 gr
Image 2	51685	0.31+/-0.01 gr	378763	0.23+/-0.01 gr
Image 3	131929	0.72+/-0.01 gr	114861	0.09+/-0.01 gr
Image 4	169292	0.91+/-0.01 gr	-	-
Image 5	-	-	286406	0.15+/-0.01 gr

In percentual value this error can range from 1 to 10% error depending on the total weight measured. For all weight and pixel values in Table 3-8 we obtain an average weight versus average number of pixels ratio. Based on this ratio, we then compute the estimated ingredient weight based on the number of pixels identified in each image. To extract the estimation error, we compare estimated weight and real known weight and compute both the coefficient of determination R^2 and the mean error incurred with respect to the measured weight, extracted as the RMSE of the estimation errors in percentual value.

Note that the error in the weight estimation can happen due to several factors such as:

- the error on the measurement device
- the fact that ingredients may lay on top of each other (this is particularly the case for wheat bran, which is very light and tends to overlap)
- small variations in flake thickness that may not be averaged out over this quantity of flakes.

Table 3-9 summarizes the weight estimation error incurred for each of the tested non-seed ingredients:

Table 3-9: Weight estimation error for non-seed ingredients

Ingredient	Barley flake	Wheat bran	Oat flake	Cracked wheat
Mean weight error estimation	4.6%	13.0%	5.6%	1.9%
R ² coefficient	0.98	0.91	0.76	0.99

Considering that our measurement error ranges from 1 to 10%, the mean errors obtained in the pixel to weight estimation are acceptable. For instance, on wheat bran our estimation error of 13% is only slightly higher than our measuring error (5-10%). These errors are acceptable for our industrial context that requires absolute errors within 1%. For our example recipe containing 3.75% of wheat bran this would correspond to a 0.48% absolute error (below the required error of 1%). However, for recipes with more than 10% of wheat bran the error would be 1.3%, slightly over 1%. In such case we could still reduce the estimation error by averaging over different images, spreading out the ingredients or performing the study with a higher precision weight measuring device.

From literature, we could expect up to 30% variation in flake thicknesses for oat (Rosentrater et al., 2018) and barley (Schwandt et al., 2017). Therefore, we could expect some weight variation between flakes even of the same size contributing to an increased weight estimation error. However, we have incurred in low errors of around 5% for both oat and barley flakes. Therefore, we hypothesize that by measuring several flakes simultaneously, we have also averaged out potential thickness variations between flakes.

Band analysis with Genetic Algorithm and comparison to RGB

The Genetic Algorithm is run together with our selected classification method (LDA+QDC). The results obtained are shown in Table 3-10, comparing the mean and minimum class accuracies per pixel for different band subsets.

Table 3-10: Seed discrimination accuracies as a function of the number of selected wavebands

	# bands	bands	Mean accuracy (%)	Min accuracy (%)
All bands	147	470-900nm	93.1	75.3
Best 15	15	470,492,500,518,553, ...817nm	89.9	65.2
Best 5	5	500,567,624,773,884nm	88.1	54.1
Best 3	3	492,632,842 nm	83.8	53.2
RGB	3	3 broad bands	76.9	35.9

As we can see, using all 147 available bands provides the highest mean pixel accuracy for our test set (93.1%) as well as the highest minimum pixel accuracy per class (75% corresponding to millet). However, the number of bands can be reduced to, for instance, 15 bands without heavily compromising the mean accuracy (~90%). The selected bands show that the visible range is important, for instance to discriminate red millet from yellow millet. In the case of millet, the relevant pigments

are carotenoids for yellow millet in the 450-480 nm range (Yano et al., 2017) and anthocyanins for red millet in the 450-600nm range (Kobayashi et al., 2006). Kong et al, (2013) have also shown that the selection of a reduced number of bands can still maintain high classification accuracy. In that study 100% accuracy was obtained for rice seed discrimination when all bands were used and around 90% accuracy when 12 selected bands were used. Boelt et al, (2018) and Carstensen et al, (2018) also achieved high discrimination accuracy above 90% with only 20 bands provided by their multiple LED system. Nevertheless, for some applications it may be preferable to have an initial higher number of bands available (such as 150 in our hyperspectral system) to maximize discrimination.

It is also interesting to notice that the best combination of 3 bands (492, 632 and 842nm) outperforms the use of RGB bands considerably, increasing both mean and minimum accuracies. Similar findings were obtained by (Vu et al., 2016) where rice seed variety discrimination is increased from 74% for RGB features to 84% with VNIR hyperspectral imaging.

The same classifier and spatial post-processing described for the hyperspectral image were applied to the RGB image. This results in high seed estimation error for some ingredients in Table 3-11: 1.72% absolute error for millet, and 0.65% for sesame, corresponding to 2% real abundance. Therefore, for a sesame abundance of 4% this would result in 1.3% absolute error, above the maximum allowed. We can conclude that hyperspectral imaging clearly outperforms RGB making it a promising tool for accurate and fast multi-ingredient estimation.

Table 3-11: Seed estimation accuracies for RGB broadband image

Ingredient	Percentage (%)	Actual # seeds	Estimated # seeds	Relative error (%)	Absolute error (%)
Sunflower	1.75	2	2	0.00	0.00
Linseed	2.00	16	16	0.00	0.00
Corn	1.75	5	4	20.00	0.35
Red millet	2.00	14	14	0.00	0.00
Yellow millet	2.00	22	4	81.81	1.63
Sesame	2.00	37	25	32.43	0.64
Poppy seed	1.75	113	103	8.84	0.15

For non-seed ingredients such as wheat bran the classification accuracy with hyperspectral imaging is of 86% (see Table 3-5) and with RGB bands this decreases to 63% accuracy. For this reason, we can also expect higher error in the weight estimation of non-seed ingredients since it is based on the pixel count.

3.4 Conclusions

Hyperspectral imaging in the VNIR range was shown to provide quantification of both seed and non-seed ingredients in multigrain wheat flour mixes in an automatic way and with higher accuracy than regular color imaging. Combination of spectral and spatial processing provides a total seed count with an absolute error below 1% for most ingredients. For non-seed ingredients (flakes and wheat) the estimation was done based on a total pixel count of the labelled pixels and resulted as well in the required accuracy in most cases.

This application requires relatively high spatial resolution to be able to correctly classify small ingredients, while still being able to cover a large enough area with a representative amount of different flour ingredients. For this reason, the new generation of VNIR hyperspectral cameras with high spectral and spatial resolution (up to 7 Mpixels) are considered suitable for this application. A comparison has been made with the discrimination accuracy of a hypothetical color camera with the same spatial resolution and measurement setup. Hyperspectral imaging, even with a reduced number of 15 bands, outperforms colour imaging by up to 15% in terms of the mean classification accuracy, which results in more accurate estimates for the ingredient fractions.

Chapter 4

Illumination as a key element in hyperspectral imaging

The highest priority in this chapter's devil's triangle is to optimize performance in terms of discrimination power, while reducing complexity or cost is secondary. In terms of application performance, we focus specifically on increasing the discrimination power while the spatial resolution remains the same and the acquisition speed may even be increased.

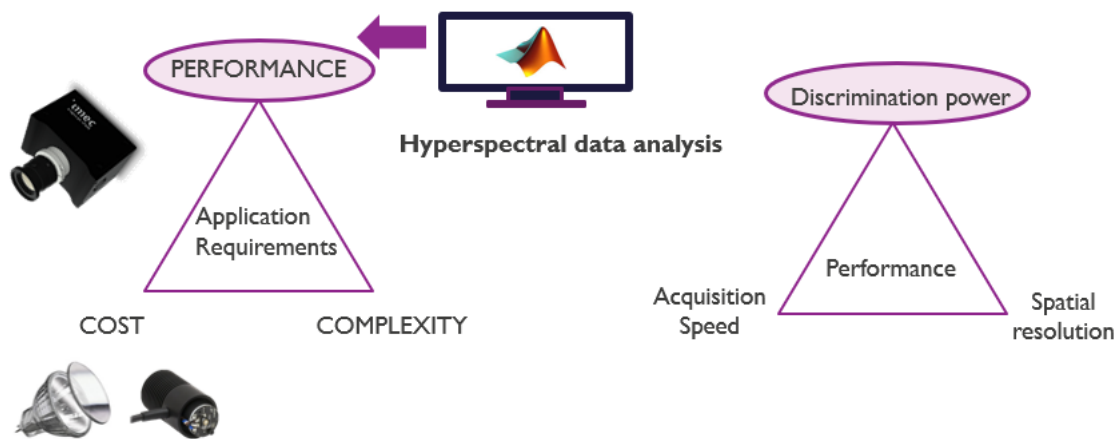


Figure 4-1: Devil's triangle of application requirements (left) and application's performance (right)

In Section 1.4 we hypothesized that the illumination is a key factor in hyperspectral systems, even more important and challenging for snapshot cameras, where a whole surface as field of view, instead of a line, needs to be homogeneously illuminated. Therefore, the impact of different illumination systems and how they can be optimized with respect to on-chip snapshot-alike hyperspectral cameras are investigated in this chapter. For this purpose, halogen illumination systems and two different led illumination systems will be compared on the same application of seed discrimination used in Chapter 3.

This chapter is partially adapted from:

Blanch, C., Luyten, H., Saeys, W., and Lambrechts, A. "Optimized custom LED illumination for hyperspectral imaging" in the *International Conference for Near Infrared Spectroscopy (ICNIRS)*, 15-20 September 2019.

4.1 Introduction

As previously indicated, the illumination system is an important element of a hyperspectral imaging system. As recent developments in LED lighting create possibilities for optimizing the illumination in an energy efficient way, we will evaluate the added value of a tunable LED system compared to a traditional halogen-based system for the case of seed ingredient quantification in flour mixes. To our knowledge, our research is the first to compare the use of a halogen versus a custom tunable LED illumination for a specific hyperspectral imaging application.

4.2 Materials and Methods

4.2.1 Camera System

We use the Snapscan camera system which was also used in Chapter 3 and illustrated in Figure 3-2. This camera system combines the high spatial and spectral resolution of imec's hyperspectral linescan sensor, in our case 7Mpixels and 150 spectral bands, and the ability to acquire datasets as easily as with a snapshot camera.

4.2.2 Illumination Systems

Halogen illumination system

We use 4 halogen Osram lamps (12v 2800k 20W). Halogen systems are broadly used in hyperspectral imaging due to its broad emission spectrum and its relatively low cost. Figure 4-3 shows the radiance spectrum of a white reference tile under halogen light. The spectrum shows here a combined effect of light source, sensor sensitivity and filter transmission efficiency. The energy is not evenly distributed over the full wavelength range, as it was illustrated in Figure 1-6 for Halogen illumination (Chapter 1). In addition to this, the hyperspectral sensor sensitivity is also wavelength dependent. Figure 4-2 shows our combined sensor and filter sensitivity, as a function of the wavelength in the 450-900 nm range (Gonzalez et al, 2016). We can see that our hyperspectral sensor is more sensitive at some wavelengths than others and this may not necessarily match our light source distribution with the result that some bands may be underexposed while others may be saturated for the same integration time for all bands.

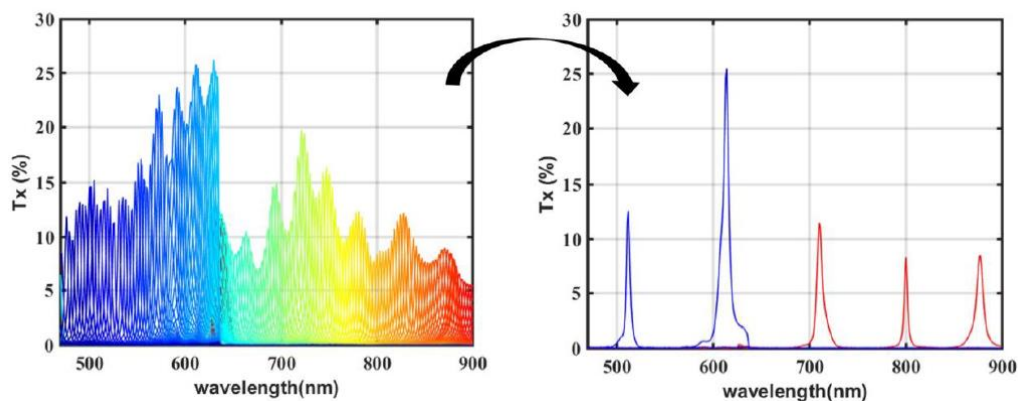


Figure 4-2: Combined transmission efficiency of filters and sensor as a function of wavelength for full filter bank (left) and transmission efficiency for five selected bands (right) (Gonzalez. et al. 2016)

Finally, the imaged materials will have a different energy response in different bands, typically stronger in the infra-red region (>700nm) than in the visible range (<700nm). All these aspects together result in an un-matched energy distribution and sensitivity. One way to deal with this is to have a more balanced light source, for which we investigate a tunable LED system from CVRL (CVRL Ltd). We can then compensate for our sensor sensitivity by tuning our LED system accordingly and potentially also for a specific object reflectance.

Another way to tackle this is to allow for multiple exposure times to be used according to the targeted wavelength range and its specific sensitivity and received energy. This is implemented in our camera as a High Dynamic Range mode.

High Dynamic Range (HDR)

Generally, the exposure time of the camera is set to a fixed value to maximize the dynamic range while avoiding pixel saturation to happen. This means that the bands of the sensor receiving the highest energy/ having highest sensitivity will saturate and limit the exposure time for the remaining bands, causing very different SNR values for different wavelength ranges in the spectral image. To overcome this, the HDR mode combines multiple frames, each acquired with a different exposure time. After acquisition of the first frame at a given exposure time, other frames are acquired with larger exposure times to provide a better signal on pixels that capture less light. The HDR mode is configured through the number of frames and longest exposure time to use. In our case we use 3 HDR frames as a good tradeoff between efficiency and acquisition speed. The optimal exposure time for each HDR frame is computed based on the exposed scene. In our case the 3 HDR frames were acquired at 13, 26 and 39 ms. Figure 4-3 shows the radiance spectrum of the white reflectance tile for the halogen system with and without HDR. We can see how HDR tries to balance the energy distribution by increasing the integration time on the visual range and reducing it for the infrared range.

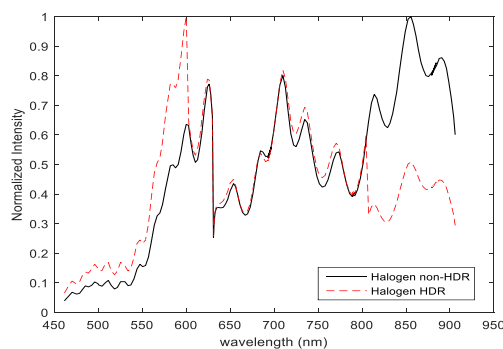


Figure 4-3: Comparison of radiance of white tile for halogen lights with and without HDR functionality

Tunable LED system

Figure 4-4 shows a sketch of the tunable-LED system prototype consisting of 4 identical LED bars in a square formation. Every LED bar consists of 3 repeated units which are 10 cm long. Every unit contains 16 LEDs of a different wavelength between 451nm and 940nm. The LED bars are controlled 2-by-2 by the same circuitry giving us 32 tunable channels (16 types of LEDs x 2 circuitries). The LEDs are placed symmetrically, with identical disposition front-rear and left-right to achieve a more homogeneous spatial distribution. The relative intensity of each LED is tuned to obtain a balanced energy distribution for our sensor.

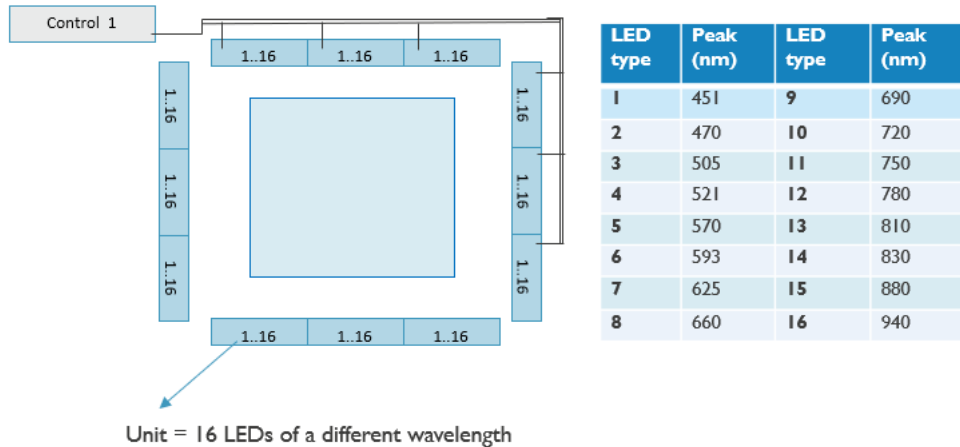


Figure 4-4: Sketch of custom tunable LED system with repeated units of 16 led types

Figure 4-5 compares the radiance spectrum of a white reference tile showing how the tunable LEDs achieve a more homogeneous spectral distribution of the energy over the different wavelengths. We can see that the LED has more energy over the blue range (400-600nm) and less energy in the infrared range from 800nm on.

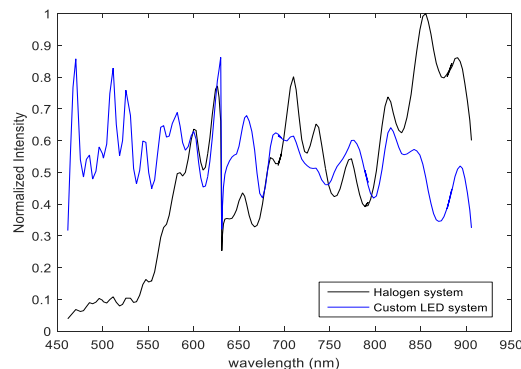


Figure 4-5: Comparison of radiance of white tile for halogen versus custom tunable LED system

Fixed LED system

We now evaluate the added value of a recently developed Fixed LED bar system of Effilux (“Effi-flex”, 2020). The Fixed LED bars can illuminate in the visible and near-infrared area, with the energy distribution provided in Figure 1-8. In the fixed LED bar case, we cannot optimize/tune portions of the spectrum intensity to match our sensor sensitivity, like in our tunable prototype. However, the spectral distribution provided in Figure 1-8 is relatively balanced over the spectrum, in any case more balanced than regular halogen lamps. Other advantages of the fixed LED system are that it can provide higher output intensity than our tunable prototype and it has a more compact factor.

We first evaluate the impact with a single bar element. Each led bar has three types of glass that can be placed in front of the lenses, as shown in Figure 4-6. These different glasses have different diffusion strengths to allow different tradeoffs in terms of light intensity and homogeneity:

- Transparent glass: allows maximum intensity with no diffusing elements and therefore lower homogeneity.
- Semi-diffuse: allows intermediate intensity and some degree of light diffusion.

- Opaline: lowest intensity but highest diffusion and homogenization



Figure 4-6: Different glasses to be used with the fixed LED bar ("Effi-flex", 2020)

We tested all three glass systems in combination with the LED bar. The integration times used to obtain maximum exposure while avoiding saturation to happen are 15 ms for the halogen system, 29 ms for the semi-diffused and 180 ms for the opaline configuration. We assumed that a more diffused component should provide us with more homogeneous illumination and potentially higher discrimination accuracy or lower spectral standard deviation. However, the associated energy loss was of factor 6 in opaline configuration with respect to semi-diffused. In addition, the improvement in terms of both spectral standard deviation and classification accuracy was marginal (below 1%) in opaline versus semi-diffuse configuration. For this reason, we considered the semi-diffuse glass to provide a good trade-off in terms of intensity and diffusion/illumination homogeneity.

The different systems, tunable led system, halogens, and fixed led bar system are shown in Figure 4-7 (left). On the right the radiance spectrum of a white reference tile is shown for Halogen versus the fixed LED bar. We can observe a higher intensity in the visible range and a lower intensity in the NIR for the LED bar.

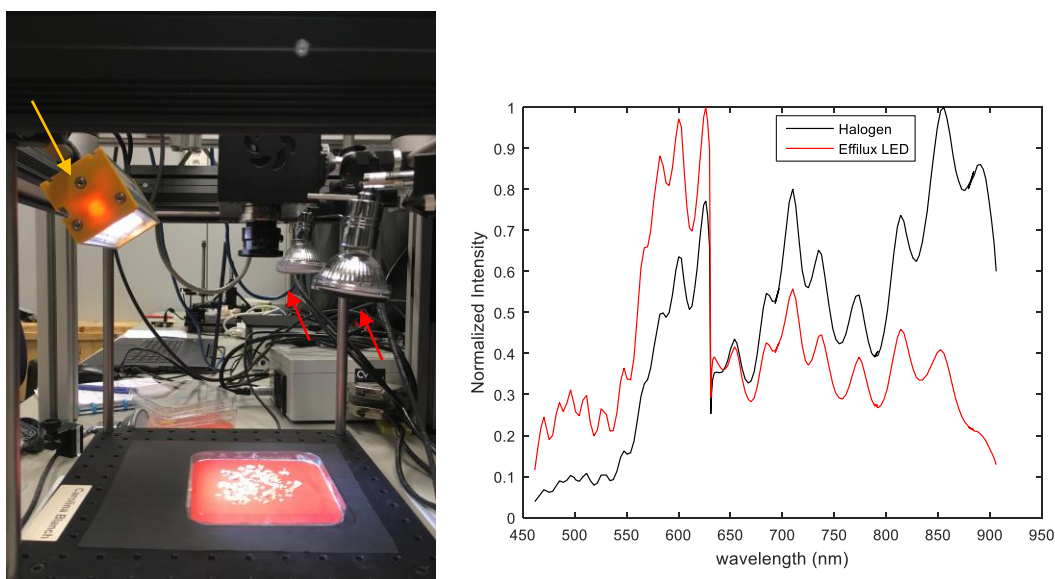


Figure 4-7: Left image: Location of Effilux bar (indicated by yellow arrow) and halogen lights (see red arrows). Right image: radiance distribution on white tile (right) comparing halogen and fixed LED bar from Effilux

In addition, we tested a LED-based system with 4 fixed LED bars, with semi-diffuse configuration, which are placed symmetrically to have more homogeneous spatial illumination. The setup is shown in Figure 4-8. In the right side we show the halogen system placed inside the fixed led one.

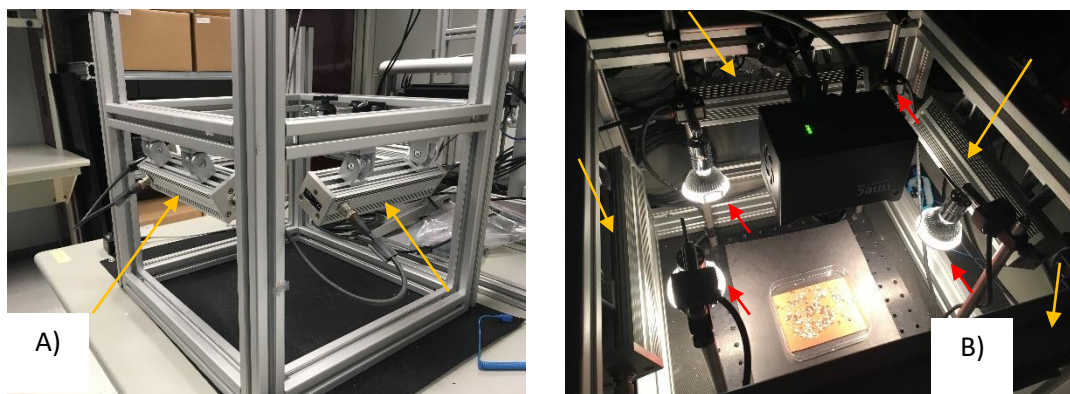


Figure 4-8: Fixed LED-based system with 4 bars placed symmetrically (A) and Fixed LED system with halogen lights inside (B). Halogen lights are indicated by red arrows while LED bars with yellow arrows.

In this respect, it is important to note that two different experimental setup conditions have been used. The first experiment aimed to compare Halogen illumination, with and without HDR, with tunable LED illumination. The second experiment aimed instead at comparing Halogen illumination with the 4-bar fixed LED system. These two experiments cannot be compared to each other in absolute numbers since the setups were not identical in terms of camera height for instance, which impacts slightly the final discrimination accuracy obtained. Therefore, the most relevant aspect here is the relative discrimination increase obtained in each of the comparisons: Halogen versus tunable LED system, and Halogen versus commercial fixed LED system.

4.2.3 Sample selection and processing pipeline

To compare the different illumination systems, we use the challenging case of seed mixture inspection, which was already introduced in Chapter 3, with the goal to accurately classify and quantify different seed types. We imaged identical seed scenes under the different illumination systems and randomly selected train and test pixel positions in the hyperspectral images. We created a mask of train/test pixel locations that we apply to HDR and LED images to guarantee identical pixel selection. We also fix all random seed generators to make all results reproducible. This way, we can make the comparison for identical train/test input and identical classifier method which illumination method yields better classification results.

For the spectral processing we used Matlab 2015 (The Mathworks, Natick, MA, USA) and the Perclass 5.2 software (PerClass BV 2008-2021, Delft, NL). Specifically, we use Linear Discriminant Analysis as a pre-processing step and Quadratic Discriminant Classifier as a classification method.

4.3 Analysis and results

4.3.1 Evaluation of HDR and the tunable LED system

Figure 4-9 shows the mean reflectance spectra obtained under the halogen illumination and the tunable LED one for a variety of seeds. We can see that with the Halogen system in the visual range (470-600nm) we have a bit more noise due to the low emission of the halogen source in this range. We can see in the mean reflectance spectra obtained under the custom tunable led system that the visible range (470-600 nm) becomes less noisy thanks to more balanced visible and infrared energy.

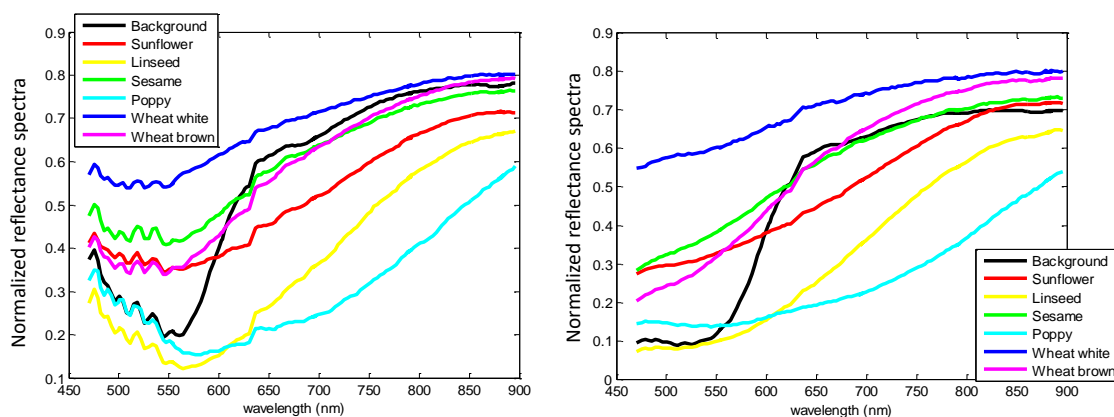


Figure 4-9: Normalized mean reflectance spectra of different seed types acquired with the halogen system (left) and tunable LED system (right)

We test the impact of the tunable LED system and the Halogen system with and without HDR functionality scanning the same scene of challenging seed ingredients for the different methods but with identical training and testing pixel locations. Table 4-1 shows the pixel-based classification accuracy for each ingredient class and the different illumination systems. We can see that the classification accuracy is lowest (60-70% in the halogen system) for some challenging ingredients such as soy grit, soy hull, yellow millet, and sesame. When the HDR method is enabled on the halogen system we can see that classification accuracy increases for the most challenging ingredients by 5 to 9% and on average for all ingredients from 80% to 84%.

Table 4-1: Comparison of pixel classification accuracy under the different illumination systems: Halogen, Halogen + HDR and Tunable LED system

	<i>Halogen system</i>	<i>Halogen with HDR</i>	<i>Tunable LED system</i>
Background	95%	96%	100%
Soy grit	64%	69%	83%
Linseed	88%	90%	91%
Corn	87%	89%	97%
Soy hull	73%	79%	81%
Millet	69%	71%	85%
Oat flake	96%	98%	98%
Sesame	67%	76%	83%
Mean accuracy	79.8%	83.5%	89.7%

By using the tunable LED illumination, we can obtain an even more noticeable improvement. With respect to Halogen with HDR, the pixel classification accuracy increases by 2 to 14% for the most challenging ingredient classes, while the average classification accuracy increases from 83.5% to 89.7%. If we now compare the discrimination power of the halogen system without HDR and the tunable LED system a more significant gain in classification accuracy is obtained: from 12 to 19% for specific ingredients and overall, the mean accuracy increases from 80.8% to 89.7%. Note that the tunable LED system does not require HDR mode since it already achieves a balanced spectral energy distribution.

For a better visualization Figure 4-10 shows the per pixel classified image, obtained under halogen lights and under custom tunable LED illumination. Zooming in on a small, circled area of the image (Figure 4-11) shows a noticeably improved classification. Higher pixel classification accuracy translates into a higher percentage of the pixels in one seed being correctly labeled. This allows better seed definition and potentially a more accurate detection of seed ingredients.

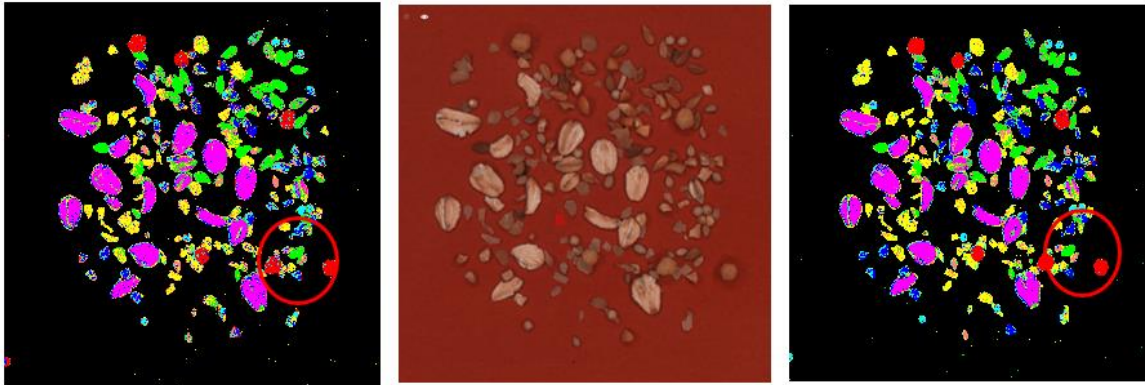


Figure 4-10: Classified images of seed mixes under halogen lights (left) and tunable LED lights (right), with false color image in the middle.

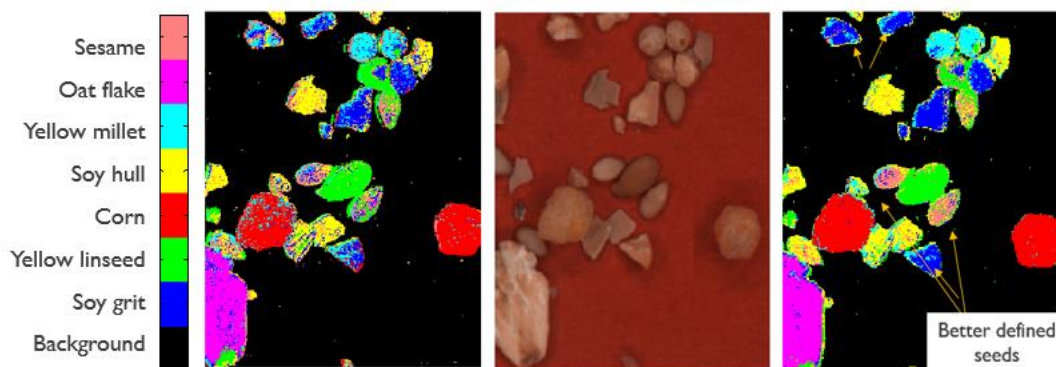


Figure 4-11: Zoomed-in area from Figure 4-10: under halogen light (left), false color image (center) and tunable LED lights (right)

Table 4-2 shows how the improved per-pixel classification accuracy translates into a better seed quantification. For this purpose, the spatial post-processing step presented in Chapter 3 has been applied for seed detection and quantification. We can see how the average ingredient quantification error decreases from 23.4% to 12.8% with tunable LED illumination. The effect is the largest for the most challenging ingredients, for soy grit with a reduction from 48% to 15% and for sesame with a reduction from 41 to 23%.

Table 4-2: Estimation error in ingredient quantification for Halogen versus Tunable LED systems

Ingredient	Actual # seeds	Halogen System		Tunable LED System	
		Estimated # seeds	Relative error (%)	Estimated # seeds	Relative error (%)
Soy grit	33	17	48%	28	15%
Linseed	30	25	16%	26	13%
Corn	6	6	0%	6	0%
Soy hull	58	37	36%	44	24%
Yellow millet	13	16	23%	15	15%
Oat flake	18	18	0%	18	0%
Sesame	17	10	41%	13	23%
Average Error			23.4%		12.8%

4.3.2 Evaluation of a fixed LED bar system

Figure 4-12 shows the mean reflectance spectra of the different ingredients for one flour mix under different halogen illumination and the fixed LED system with one bar. We can see how the more balanced energy distribution of the LED system (in this case with transparent glass) increases the SNR in the visible range of the spectra with respect to the halogen illumination.

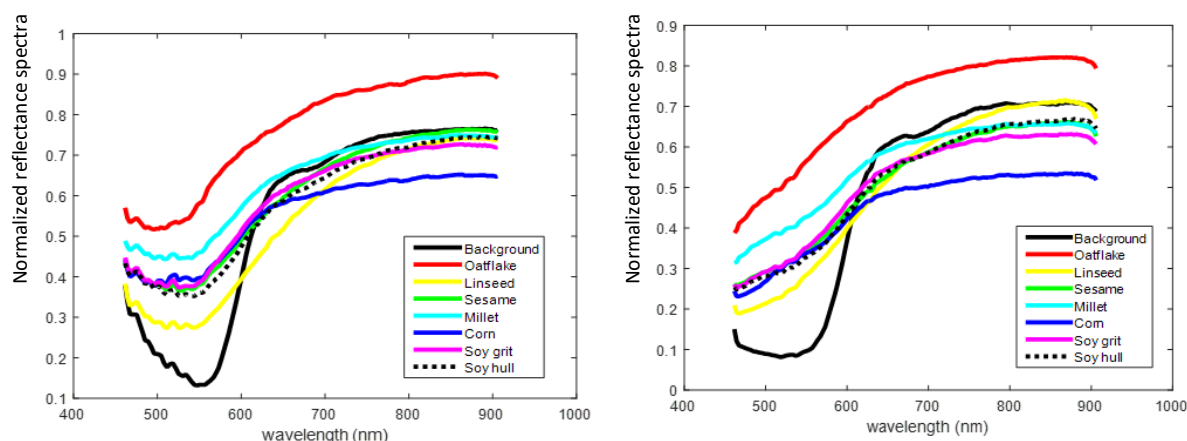


Figure 4-12: Normalized mean reflectance spectra show reduced noise in 450-550nm range under Halogen light (left) and Fixed LED (right)

Nevertheless, when we evaluate the discrimination accuracy for the exact same image, same training samples and same classification method (LDA+QDC) we do not obtain an increased discrimination accuracy under LED illumination. Table 4-3 shows the classification accuracy per pixel for the different ingredient classes. We can see that, despite the improved appearance of the spectra, the accuracy is considerably reduced with a 1-bar Fixed LED illumination (mean of 73.5%) with respect to halogen illumination (81.7%).

Table 4-3: Pixel classification accuracy for Halogen System and 1-bar Fixed LED system (semi-diffused)

	Halogen system	1-bar fixed led system
Background	99%	92%
Soy grit	68%	57%
Linseed	88%	78%
Corn	86%	70%
Soy hull	71%	70%
Millet	68%	66%
Oat flake	97%	81%
Sesame	77%	74%
Mean accuracy	81.7%	73.5%

The reason for this decreased performance with the LED bar with respect to halogen, despite higher SNR spectra in the visible range, is probably the lack of spatially homogeneous illumination with one single led bar. In this respect, the lamp placement for the halogen system, and for the tunable LED system presented in the previous section, is more symmetrical than with one single fixed LED bar, as illustrated in Figure 4-13.



Figure 4-13: Lamp positioning for the different illumination systems compared

The effect of the lack of spatially homogeneous illumination can be seen in Figure 4-14, where a small portion of the seed image is shown. We can see how under one 1 fixed LED bar sharp shades are created on the opposite side of the LED bar position. In the halogen and tunable LED systems light is coming from at least 4 directions having a more balanced distribution of the illumination. This results in similar shading effects around each seed, especially those which are thicker.

Spatially homogeneous illumination results in the seeds being equally illuminated over their entire surface, while in the 1-bar fixed LED case we can see that some parts of the seed are more illuminated than others increasing the spectral variation within a seed.



Figure 4-14: Illustration of the impact of the spatial distribution of illumination: Halogen (left), Tunable LED system (middle), Fixed LED system semi-diffuse (right). The arrows indicate the seed shadow locations.

To check this, we compute for the same pixel samples of three different ingredient classes (soy grit, linseed, and corn) the standard deviation of the spectra by averaging the standard deviation for all wavelengths in our 470-900 nm range.

This can be seen in Figure 4-15, where the mean reflectance spectrum and its standard deviation are shown. Especially in the near-infrared range we can see that the standard deviation is noticeably higher in the 1-bar fixed LED case than in the halogen system. Table 4-4 shows the comparison of the spectral standard deviation, averaged over all wavelengths, for the same samples under halogen, fixed LED system and tunable LED systems.

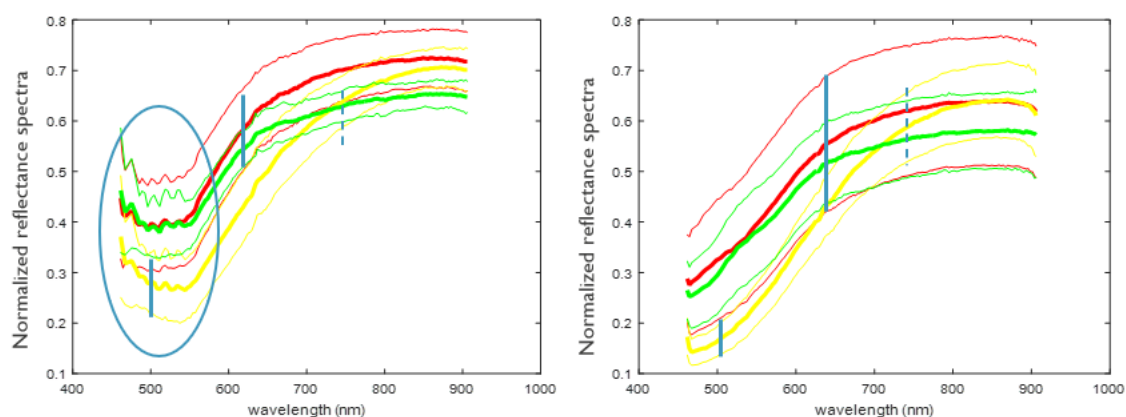


Figure 4-15: Normalized mean reflectance spectra in the (0..1) range \pm standard deviation for three ingredients: soy grit (red), linseed (green) and corn (yellow). Halogen-based illumination (left) and fixed LED based (right).

The standard deviation is the highest in the fixed system with 1 LED bar, which would explain the lowest achieved discrimination accuracy. On the tunable LED system, we achieve in general the lowest standard deviation resulting in lower intra-class variation and highest discrimination accuracy.

Table 4-4: Standard deviation of normalized reflectance spectra (0 to 1), per class for different illumination systems

Mean Standard Deviation	Halogen	Fixed LED (1 bar)	Tunable LED system
Class 1 (Soygrit)	0.072	0.127	0.074
Class 2 (Linseed)	0.056	0.059	0.037
Class 3 (Corn)	0.038	0.078	0.035

In conclusion, we can see that having a homogenous spatial distribution of the illumination can be as important or more than achieving a spectrally homogeneous energy distribution over the full range. For this reason, we now test a setup with a fixed LED system with 4 LED bars and place them more symmetrically to try to mimic what was done with the halogen and tunable LED systems. Table 4-5 shows the pixel-based class accuracies for the LDA-QDC classifier and both halogen-based systems and fixed LED-based system with 4 bars. We can see that now a slightly better performance is achieved with the LED system. This is noticeable in terms of the minimum classification accuracy, which increased from 61 to 67%. A similar integration time is used for both systems, 20 ms for the halogen-based and 25 ms for the fixed LED one. This relatively low integration time is advantageous with respect to the tunable LED-based system where roughly double integration time than halogen-based was required.

Table 4-5: Pixel classification accuracy per ingredient on images acquired with the Halogen and fixed LED systems

	Halogen system	4-bar fixed Led system
Background	99%	98%
Soy grit	67%	72%
Linseed	92%	95%
Corn	91%	94%
Soy hull	91%	90%
Millet	61%	67%
Oat flake	94%	91%
Sesame	87%	84%
Mean accuracy	85.2%	86.3%

In terms of performance, however, the fixed LED system does not reach the accuracy increase obtained by the tunable LED system, which was around 10% better in mean accuracy than the halogen-based system. This is due to the fact that the fixed LED system has a more balanced energy distribution in the VNIR range than halogen systems, but it does not fully optimize the energy distribution according to our sensor sensitivity.

Figure 4-16 shows the standard spectral deviation of three ingredient classes for the halogen system (left) and the 4-bar fixed LED system (right). We can see how the standard deviation of the spectra is always higher for the LED system. Again, despite an improved SNR in the visual range a bigger intra-class variation is obtained, which probably explains why the accuracy increase over the halogen is more limited than expected.

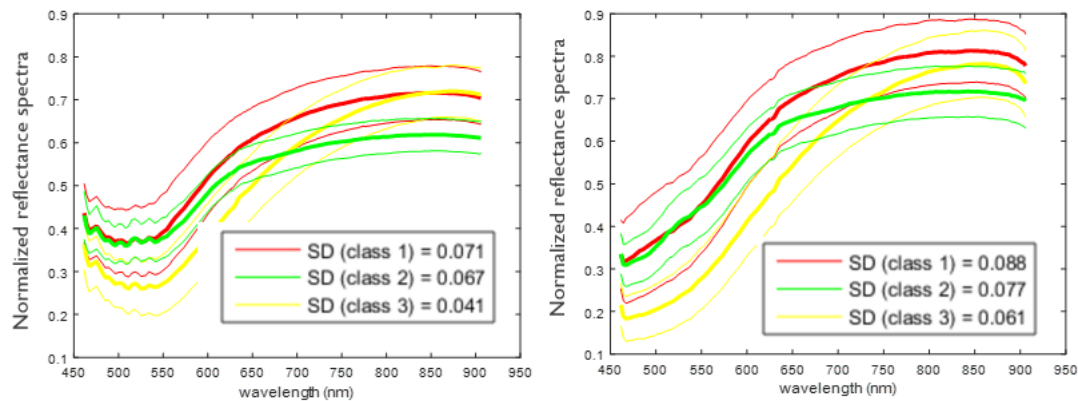


Figure 4-16: Standard deviation of normalized reflectance spectra for 3 ingredients and halogen-based illumination (left) and fixed LED based (right). The solid lines indicate the mean value with their mean \pm one standard deviation. The ingredients are: soy grit (red line), linseed (green line) and corn (yellow line)

Moreover, from the analysis in Table 4-6 of the standard deviation of the normalized radiance spectra over the full surface of a white tile, it seems the fixed LED system might not achieve an equally homogeneously spatial distribution as our tunable LED system. We can see that the spatial deviation is very similar in the fixed LED system to that in the halogen system. In particular in the lower range (460-615 nm) the standard deviation is proportionally higher in the fixed LED system, which may be a more relevant wavelength range for seed discrimination than the higher 750-900 nm range where the spectral curves flatten.

Table 4-6: Comparison of spatial homogeneity in Halogen and fixed LED systems calculated for a white tile

	Halogen	4 bar fixed LED system
Spatial Std Dev	10.29	9.9
Spatial Std Dev(mean)	0.065	0.063
StdDev (460-615nm)	1.73	3.69
StdDev (615-750nm)	3.48	3.56
StdDev (750-900nm)	5.07	2.63

4.4 Conclusions

We have compared the impact of a halogen illumination system with a tunable LED system with a more balanced energy distribution over the spectrum. In addition, we have tested the impact of a High Dynamic Range mode, which compensates for the variation in the emission spectrum of the halogen system. The use of HDR mode in combination with the halogen illumination increased the average classification accuracy from 80.8% to 84.1%, with up to 9% improvement for the most challenging ingredients. The tunable LED illumination system gave an even larger improvement increasing the average accuracy from 80.8% till 89.7% and almost 20% extra accuracy for the most challenging ingredients.

In addition, we have tested a fixed LED system with a more compact factor and with an illumination intensity more comparable to the halogen system. We have seen that an improved spectral response in the visible range is achieved due to a more balanced energy distribution over the full wavelength range. However, this is not sufficient to guarantee an increased discrimination accuracy since achieving a balanced spatial energy distribution is also a relevant aspect. A better spatial distribution of the led bars provides an increased discrimination accuracy in this respect although the performance increase was more limited than in the tunable LED case. This can be seen as well from the higher intra-class spectral standard deviation than obtained with the tunable LED system.

We can conclude that it is advisable to invest in an illumination system that provides more homogeneous spatial and spectral distribution. This is particularly the case when the information of our application resides in the spectral dimension. In this case, lack of spatial homogeneity increases intra-class variation for different image locations, which can negatively impact our discrimination power, in particular for pixel-based analysis. In contrast, an analysis based on shape and spatial information would be more robust to these spatial variations. However, even in the case that more information is present in the spatial domain than in the spectral one, having spatially homogeneous illumination is important. This was shown as well in Chapter 1 for computer vision systems using regular color imaging.

Chapter 5

Joint evaluation of the combined effect of illumination, camera hardware and analysis methods

In this chapter, we test the hypothesis that all system parameters should be jointly investigated. In this respect, system parameters such as camera hardware, illumination system and data analysis methods need to be considered. This should allow us to explore different tradeoffs at system level to find the best combination of system parameters.

Figure 5-1 shows the Devil's triangle for our hyperspectral system. In this chapter we are going to focus on the three corners of this triangle, exploring therefore all tradeoffs available between these three application aspects. In this respect, camera hardware and illumination system are system parameters with an impact on cost and performance, while data analysis methods typically have a larger impact on performance and system complexity.

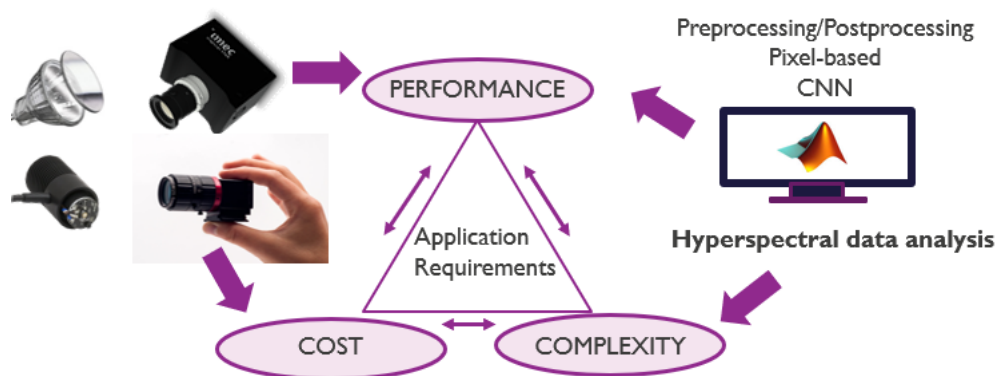


Figure 5-1: Devil's triangle in hyperspectral system's design requiring tradeoffs between performance – cost – complexity.

We show in this chapter how different system configurations can be used to offer different performance-cost-complexity tradeoffs to best match the application requirements. We also show that the same performance may be achieved with different system configurations. For example, in our specific application a configuration with a basic pixel-based classifier and a high-quality illumination system achieved the same performance as a configuration of a more basic halogen illumination with more advanced image-based processing.

Figure 5-2 illustrates the Devil's triangle in terms of application performance, where tradeoffs have to be made between spectral discrimination power, spatial resolution, and acquisition speed. To this end, we will consider multiple system parameters, which will impact each of these aspects. For instance, the use of a low spatial-spectral resolution Snapshot camera will increase the acquisition speed, but this will happen at the expense of a reduced spatial resolution and discrimination power.

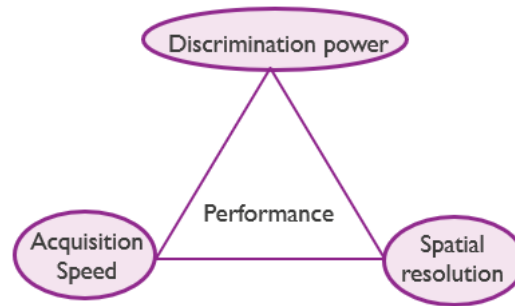


Figure 5-2: Devil's triangle representing the tradeoffs of application performance.

This chapter is adapted from:

Blanch-Pérez-del-Notario, C., Saeys, W., and Lambrechts, A. (2019, September). "Convolutional neural networks for heterogeneous ingredient discrimination with hyperspectral imaging". In 2019 10th Workshop on Hyperspectral Imaging and Signal Processing: Evolution in Remote Sensing (WHISPERS) (pp. 1-6). IEEE.

Blanch-Pérez del Notario, C., López-Molina, C., Lambrechts, A. and Saeys, W. "Hyperspectral system trade-offs for illumination, hardware and analysis methods: a case study of seed mix ingredient discrimination", in *Journal of Spectral Imaging* 9, a16 (Dec 2020).
<https://doi.org/10.1255/jsi.2020.a16>.

5.1 Introduction

Hyperspectral Imaging (HSI), which combines spectroscopy and imaging, is increasingly investigated as a non-destructive, real-time tool for food quality analysis and control (J. Amigo et al., 2013). Key factors in hyperspectral systems and in computer vision systems in general are the illumination system used (Brosnan et al., 2004), the trade-offs in the camera characteristics (spatial resolution, spectral resolution, speed and SNR) and the type of data analysis used (Signoroni et al., 2019, Lv et al., 2020), which can be broadly categorized as either pixel-based (purely spectral analysis) or space-aware (jointly exploiting the spatial and spectral information available).

While many researchers have investigated trade-offs at the level of individual system components, very few have explored the full configuration of HSI systems, either collectively optimizing all factors or exploring the potential synergies and trade-offs they involve. For example, Kerekes et al. (2003) developed a model for a hyperspectral imaging system in remote sensing relating sensor settings and processing algorithms to a probability of detection. They concluded that the number of spectral bands is the most relevant parameter for a subpixel detection application. More recently, Li et al. (2019) proposed an evaluation model based on imaging conditions, sensor parameters and data processing methods to estimate the application capability, measured as a normalized mean distance between mineral classes, in a remote sensing application. However, the joint effect of the system parameters was not analyzed. Gutierrez et al. (2019) focused on system design aspects and trade-offs in a biomedical application, where mostly optical and image acquisition aspects were considered. They focused on time inefficiencies caused by API communications and the effect of Field of View selection on the elimination of spatial distortions. While they did not analyse illumination aspects, they acknowledged their importance as a future line of work.

Indeed, the illumination of an HSI system has a considerable impact on the system performance (Peter, 2015; Sawyer et al., 2017), as previously explained in Chapter 1. In section 1.3.2 we discussed how tungsten-halogen illumination is generally used in hyperspectral systems since it provides a broad-spectrum illumination. However, with the increasing availability of LED lighting solutions with different spectral characteristics, some research has also focused on exploring the suitability of LED illumination systems. This way, Lawrence et al. (2007) compared a traditional halogen system with a LED system for a faecal contamination detection showing that similar detection accuracy of 99% could be reached for both systems. Kutrašnik et al. (2013) developed a method to compare lighting systems based on spatial-intensity and spatial-spectral non-uniformity measures. They focused on avoiding specular reflections, and shades but did not quantify the performance of these systems on a specific application. Peter (2015) developed several LED ring illumination systems for a skin imaging application system, relating viewing angles to the number of LEDs required for uniform area illumination. Sawyer et al. (2017) compared the uniformity of halogen and LED based illumination systems for a biomedical application but did not report their impact on the discrimination power. Carstensen (2018) presented a LED based system for a food control application in combination with a colour camera but did not benchmark it against halogen systems. The importance of the illumination was also highlighted by Shahrimie et al. (2016) and Mishraa et al. (2020) who focused on compensating the impact of illumination on the plant spectra in a close range indoor hyperspectral setup, depending on the distance and angle from the light source.

In Chapter 4, the discrimination power of a halogen-based and a tunable LED-based system is compared in a specific application case. We concluded that a considerable gain in discrimination power (up to 10% in mean classification accuracy) can be obtained by using a customized LED system thanks to the more balanced energy distribution.

Whereas the hardware/camera configuration is somehow limited to a list of parameters and devices, the options for data analysis strategies are very diverse (Signoroni et al., 2019, Lv et al., 2020). Imaging analysis methodologies can present very different levels of complexity, normally featuring a trade-off between complexity, tractability and need for training data. Recently, there is a shift in the image processing domain from simple, traceable methods based on classical image processing which require relatively little training data (such as Quadratic Discriminant Classifier (QDC) (Naes, T et al., 2004) or Support Vector Machines (SVM) (Hsu, C-W et al., 2016) to high-dimensional, untraceable machine learning methods with heavy training (such as Deep Learning and Convolutional Neural Networks). While the latter tend to outperform the former, at least when finely tuned, the former are still preferred in industrial applications, because they offer a more robust and reliable alternative, e.g., featuring a lower risk of overfitting and/or over segmentation of the problem space.

Especially Convolutional Neural Networks (CNNs), currently the most popular family of deep learning algorithms, are widely investigated for hyperspectral image processing. However, most of the work on the application of deep learning algorithms on hyperspectral data so far has focused on remote sensing applications (Paoletti et al., 2017; Chen et al., 2016; Deng et al. 2018). Moreover, most studies were limited to the spectral (pixel-by-pixel) analysis, ignoring the spatial information in the images. Very recently, a few authors have introduced CNN approaches for joint spatio-spectral analysis in different types of close-range applications. For example, Al-Sarayreh et al. (2018) used a 3D-CNN combining spatio-spectral features to detect meat adulteration and found that it outperformed a pixel based SVM classification. Wang et al. (2018) used deep CNNs to detect internal mechanical damage in blueberries using hyperspectral transmittance data reaching classification accuracies between 85-90% on test data. In this respect, food control applications are well suited for CNNs thanks to the abundance of ground truth data samples, which are much needed by CNNs in the training phase. Farooq et al. (2019) used transfer learning to train CNNs to discriminate weeds from low resolution hyperspectral images. Gruber et al. (2019) compared deep learning schemes with more traditional classifiers for a black plastic recycling application based hyperspectral imaging in the VNIR range.

Finally, Gao et al. (2020) achieved 98% discrimination accuracy on ripeness level of strawberries with CNNs in the VNIR range.

While Convolutional Neural Networks can offer high classification performance, they also have some drawbacks in terms of their computational cost, lack of insight in the internal classification mechanism (once the CNN reaches 2-3 layers), robustness to noise and lack of coherence in results. The latter two problems can be solved by adaptively smoothing the original image prior to classification and/or the labelled image produced by the classifier. In the former case, adaptive smoothing is needed to cope with noise and signal irregularities, while in the latter the smoothing is carried out to remove isolated pixels or non-coherent neighboring relationships. Some of the best known adaptive smoothing algorithms are Anisotropic Diffusion (Perona et al, 1998) and its extensions (Weickert, 1998), Bilateral Filtering (Tomasi et al., 1998) and Mean-Shift (Comaniciu et al., 2002). In the context of Hyperspectral Imaging, Liao et al. (2016) combined Extended Morphological Profile (EMP) information with the hyperspectral image by bilateral filtering to improve discrimination in a remote sensing application. Kang et al. (2013) presented an edge-preserving classification method based on bilateral filtering. They applied bilateral filtering to the classification map obtained from a pixel-based classifier such as SVM, resulting in an increased classification accuracy. An even simpler approach to combine (and simplify) spatial and spectral information jointly is the use of a Median Filter (Gonzalez et al., 2002). Median filters are widely used as a simple yet effective denoising method to correct pepper and salt noise in colour and hyperspectral images (Thirilogasundari et al., 2012). Similarly, median filtering can be used on a pixelwise labelled image to correct locally incoherent pixel miss-classifications.

As there is interaction between the different factors involved in optimizing an HSI study, the aim of this study was to explore the joint impact of all involved factors on the resulting discrimination accuracy. This is evaluated for a challenging case study from the food industry, namely ingredient quantification in a seed flour mix. Specifically, we study the use of the illumination systems presented in Chapter 4 with cameras of different spatio-spectral resolutions and combine these with the use of different pre-processing and analysis methods. For the latter we compare a pixel-based classifier such as QDC (Naes et al., 2004) with a joint spatial-spectral classifier such as CNN. We analyse the impact as well of pre- and post-processing methods such as spatial/spectral binning, bilateral filtering (Kang et al, Liao et al) and median filtering (Gonzalez et al, Thirilogasundari et al). We also benchmark our work against colour imaging systems restricted to the human-visible spectra. To our knowledge, this is the first study where the individual and joint impact of all these system aspects (illumination, analysis method, camera spatial-spectral resolution) is investigated for a specific hyperspectral imaging application.

With this study we pursue several goals. First, we want to assess what is the highest achievable performance of our hyperspectral system, starting from a basic system configuration and gradually enabling additional system parameters. Second, we want to study the relative impact of the different system parameters once they are jointly considered. Third, we intend to investigate the available system trade-offs to meet varied application requirements in terms of spatial resolution, classification performance, computing and memory cost, acquisition speed or hardware cost. Finally, we want to investigate the suitability of low spatial-spectral resolution cameras, which initially may seem insufficient to reach high discrimination accuracies for the application considered.

5.2 Materials and Methods

This section presents all system parameters studied: the camera system used, the illumination systems and the different analysis methods investigated.

5.2.1 Materials

We imaged an identical seed mix scene containing oat flakes, corn, millet, sesame, linseeds, sesame and pieces of soy grit and soy hull. The seed mix is to be later added to wheat flour for baking. This seed scene is imaged under both halogen and tunable led illumination to obtain the corresponding images for the same scene. This later allows us to force the selection of identical training samples for all illumination and analysis methods under comparison. We created ground truth masks for all these ingredients scanned by manually selecting all pixels corresponding to each ingredient with the help of the Gimp software (GNU Image Manipulation Program, 1997). An example of this ground truth selection for a hyperspectral image is shown in Figure 5-3.

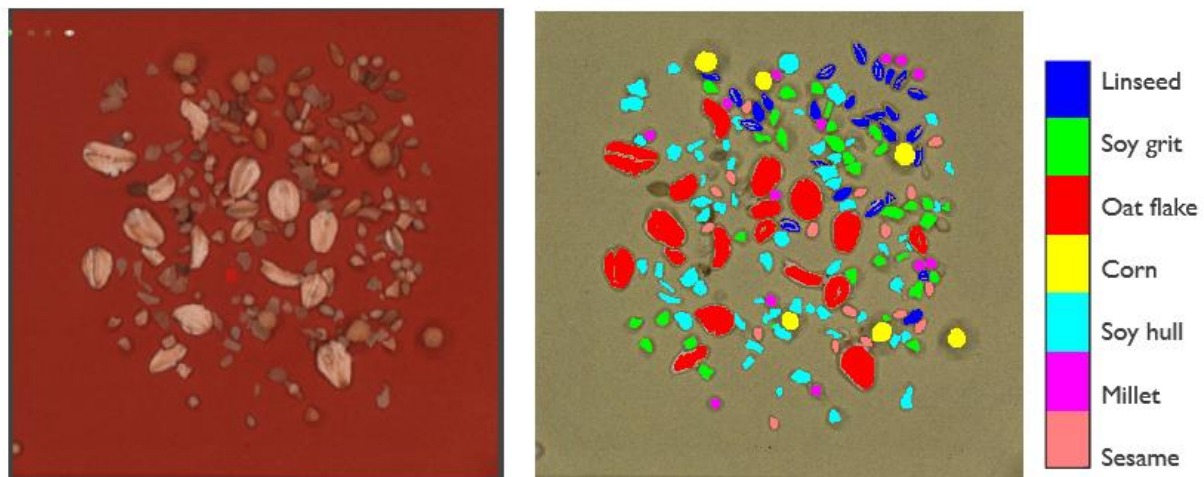


Figure 5-3: Color image of seed mix (left) and ground-truth mask selection for all ingredients (right)

We used one single image per camera system for the study, where half of the image was used as training set, while the other half was used for the validation. In the lower resolution images, since the seeds are not so homogeneously distributed, we made sure that training and testing pixels were selected from different groups of seeds in the image. In this sense, we avoided selecting random train/test pixels from the same individual seeds, which could create pseudo replicas. The created image ground truth was used to compute the classification accuracy.

It is important to note that the use of several seed images, such as in Chapter 3, would be advisable to develop a robust model for the end application. However, in this chapter our focus is to analyze the impact of the different system elements on identical train and test sets. For this purpose, the approach of a single image per camera system with the defined train and test sets is sufficient.

5.2.2 Illumination systems

We used the two illumination systems already presented Chapter 4: a halogen-based system and a tunable custom LED system. For the halogen system we use a basic configuration and a High Dynamic Range (HDR) mode that balances energy distribution by using a different exposure time per wavelength range. To perform HDR the camera performs scans at several, in our case 3, integration times (13, 26 and 39 ms). The highest integration time is used for the band range where less energy is

provided by the halogen source, while the lowest integration time is used for the band range receiving the highest energy.

The advantage of the tunable LED system with respect to the halogen system is that we can achieve a more balanced energy distribution on our sensor over the full visible and near-infrared wavelength range. Moreover, the illumination is also spatially homogeneously distributed. This translates in a reduced spectral variability, which translates into higher discrimination power for the different ingredient classes. In Chapter 4 we found that both a halogen system with the HDR method and our tunable LED illumination system (CVRL Ltd) outperformed a halogen system for the QDC classifier and a high-resolution hyperspectral image. In particular, the tunable LED system resulted in a higher SNR spectra and noticeable improvement in class discrimination/classification accuracy, with up to 10% higher mean pixel accuracy.

Figure 5-4 shows a sketch of the tunable-LED prototype with 4 LED bars. The four identical LED bars are placed in a square formation to achieve a homogeneous spatial distribution of the light. Each LED bar consists of 3 repeated units and every unit contains 16 LEDs with a different peak wavelength between 451nm and 940nm. The relative intensity of each LED was tuned to obtain a balanced energy distribution for our sensor. The spectral improvement of the tunable LED on some example seeds is shown as well.

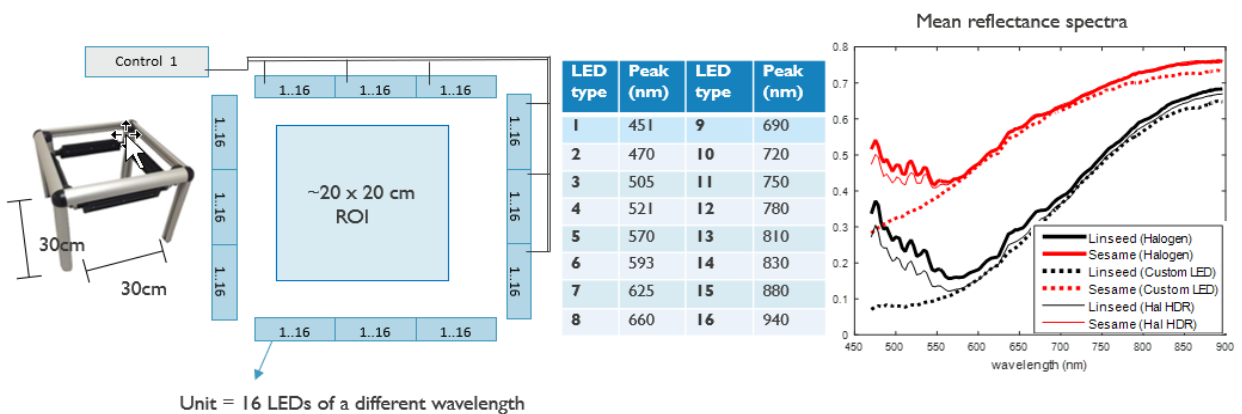


Figure 5-4: Tunable LED system (left), spatial layout (middle left), LED characteristics (middle right) and impact on the seed acquired spectra (right)

In this work, we evaluate the impact of the tunable LED system on the classification performance obtained with other two Snapshot cameras with reduced wavelength ranges. In addition, we now consider the use of additional pre-processing methods (binning, median filtering) and analysis methods which jointly exploit spatial and spectral information (bilateral filtering, convolutional networks).

5.2.3 Camera systems

We use the Imec Snapscan VNIR range camera system (Pichette et al, 2017), shown in Figure 5-5: a camera system concept that combines the high spatial resolution and spectral resolution of line scan hyperspectral imaging technology (Gonzalez et al, 2016). It can acquire datasets for a static scene as easily as with a snapshot camera. There is no need for any external scanning movement: scanning is handled internally, using a miniaturized scanning stage.

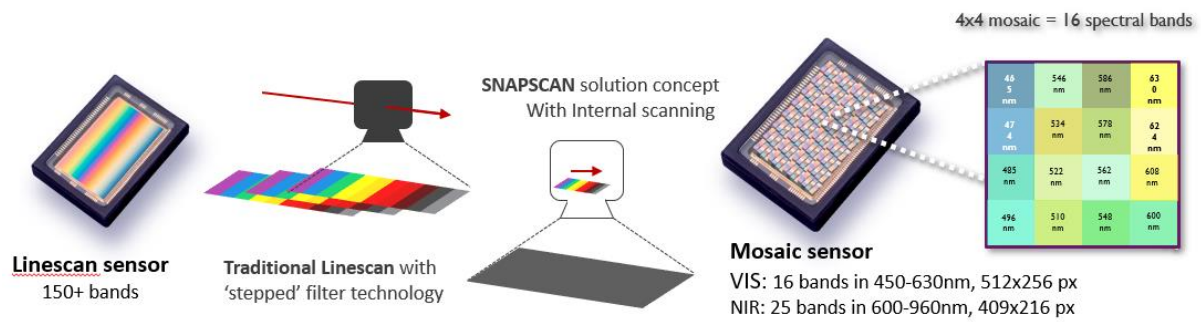


Figure 5-5: Traditional linescan sensor and scanning system (left), Snapscan VNIR system (middle) and Snapshot mosaic Vis sensor (right)

Full hyperspectral images can be acquired below 10 seconds. The maximal RAW spatial resolution that can be reached is 3650 x 2048px (7Mpx), with a spectral resolution of 150+ spectral bands within the 470-900 nm wavelength range. Some industrial applications, however, require portable and fast image acquisition even at the cost of a reduced spatial and spectral resolution. For this reason, we also test an Imec snapshot camera with a mosaic layout sensor where the full hyperspectral image is acquired for all bands simultaneously in one shot (B. Geelen et al, 2015). We have two flavours of the Mosaic camera. A Mosaic NIR camera with spatial resolution of 409 x 216 pixels, and 25 bands evenly spread in the 600-875nm range and a Mosaic VIS camera with spatial resolution of 512x256 and 16 bands in the 460-630nm range. The use of a Mosaic NIR or VIS camera allows even faster image acquisition (potentially 180 frames per second) at the cost of a reduced spatial and spectral resolution.

For our high-resolution Snapscan images there are around 150.000 ground-truth pixels. Approximately 40% of the pixels are randomly selected from the training half image. For our binned Snapscan or low-resolution Mosaic images there are 10.000-35.000 ground truth pixels available and therefore up to 80-90% of the pixels of the training set are used.

5.2.4 Analysis methods

The different analysis methods considered are summarized in the processing pipeline illustrated in Figure 5-6. The first pre-processing method that can be applied onto the input image is a denoising step, which can be implemented by either median filtering with a 3x3 or 5x5 window or by spatial/spectral binning of the original image. Another type of pre-processing method that can be applied next is feature extraction to reduce the input dimensionality. In this study, LDA (Linear Discriminant Analysis) was selected for this purpose, based on our previous study in Chapter 3. This step is applied prior to the training of the classifier, for which we test two different classification methods: The first is the Quadratic Discriminant Classifier (Naes et al. 2004), a pixel-based classifier exploiting only spectral information per pixel. The second method is a convolutional neural network (CNN), which is a more image-based method that jointly exploits spatial and spectral information. The final parameter or processing step is a post-processing method, which acts on the classified image with the purpose to correct some pixels miss-classifications by smoothing or imposing spatial coherence on the obtained classified image. For this purpose, either bilateral filtering (Kang et al. 2013), median filtering (Gonzalez et al, 2002), or both were evaluated. Our performance metric is the pixel classification accuracy as percentage of correctly classified pixels. The mean pixel classification accuracy for all seeds as well as the pixel accuracy for the worst performing seed class are provided.

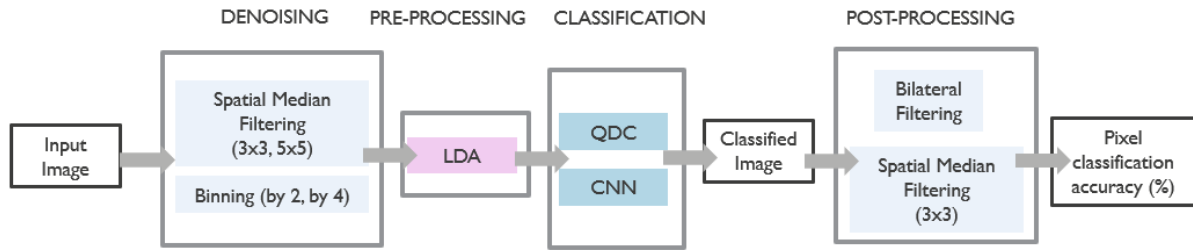


Figure 5-6: Processing pipeline for input image, with the following consecutive steps: denoising, pre-processing for feature selection, classification and post-processing on the classified image

The feature selection and classification model building were performed in the PerClass software (PerClass BV 2008-2019). For the remaining analysis methods (median filtering, binning, and bilateral filtering), we code our own Matlab scripts or use the Image processing toolbox in Matlab version R2015 (The Mathworks, Natick, MA, USA). The remainder of this section explains all these methods in greater detail.

Pre-processing methods for denoising and feature selection

Median Filtering

Median filters are a simple yet effective method for denoising colour and hyperspectral images by correcting for instance pepper and salt noise. In this sense, a median filter can be applied spatially to denoise the hyperspectral image, as well as on a classified image to correct for small pixel misclassifications. This was implemented by median filtering each waveband image in two dimensions. Each output pixel contains the median value in a N -by- N neighborhood around the corresponding pixel in the input image. We analyse its impact for pre-processing when applied as a 5x5 filter on the Snapscan image or as a 3x3 filter in the Mosaic images. A lower filter size is selected on these lower spatial resolution images to minimize the image blurring.

Spatial and Spectral Binning

Another method to increase the Signal to Noise ratio in our hyperspectral image is to implement spatial or spectral binning since averaging over pixel spectral values reduces the noise in the spectra. Both spatial and spectral binning were implemented. Spatial binning combines a cluster of $N \times N$ pixels (in our case 2x2 or 4x4) into a single pixel with its average value. This reduces the overall number of pixels and reduces the impact of noise at the cost of a lower resolution. Spectral binning by N bins is implemented by substituting each N bands by one band with their average value. As indicated, binning samples reduces the number of spatial or spectral samples available, this is, the effective spatial and spectral resolution available. This can have a noticeable impact when we are dealing with low spatial resolution images (e.g Mosaic cameras) or with small objects (e.g seeds of few pixels size) in a high-resolution image from the Snapscan camera. Therefore, binning may only be a valid alternative for denoising when the pixel size of the smallest objects is big enough.

For the first camera system, the Snapscan (1088x1048 pixels), we want to compare the different complexity – performance tradeoffs for different spatial-spectral resolutions of our seed image. We create these different resolutions by binning the full resolution image both spatially and spectrally by either factor 2 or factor 4. For our Mosaic images (max of 512x256 pixels) we do not consider binning since the original spatial resolution is lower.

Linear Discriminant Analysis (LDA) or Linear Discriminant Classifier (LDC) (Naes et al. 2004)

This method is used to reduce the feature dimension since it identifies the components (linear combination of the variables) with the highest information. LDA is a supervised method, assuming normal densities for the classes, in which the new features or components maximize the class variation. In our previous work on seed ingredient discrimination in Chapter 3 we observed that for this application LDA provided better performance than Principal Component Analysis (PCA) (Smith et al. 2002) as feature selection method. For this reason, we select LDA as the feature selection mechanism for both pixel-based and image-based (CNN) classifiers considered in this study. It is computed with PerClass (PerClass BV 2008-2019) software by finding a projection that separates each class from all others. The number of features obtained in this implementation is equal to the number of classes we are considering, minus one. In our case, with 10 classes we compress the initial 147 bands to 9 new spectral features.

Classifiers

Classifiers can be broadly categorized into pixel-based classifiers, exploiting the spectral information per pixel, or image-based classifiers, jointly exploiting spatial and spectral information. To compare the impact of both types of classifiers as system parameters we use the following classifiers, as implemented in PerClass software. Both classifiers are applied after the LDA preprocessing step:

Quadratic Discriminant Classifier (QDC):

Also known as Quadratic Discriminant Analysis (Naes et al, 2004) assuming as well normal densities for our spectral classes. Our work in Chapter 3 shows that for this application, QDC is the most performing classifier among the pixel-based ones and therefore we select it as the pixel-based classifier.

Convolutional Neural Networks:

We use a 3D convolutional neural network, illustrated in Figure 5-7 to extract simultaneously both spatial and spectral features from the Hyperspectral Image. We first reduce the hyperspectral image dimensionality by applying Linear Discriminant Analysis. From the initial 147 bands we obtain 9 LDA bands that are input to the network. This reduces the input dimensions to the network and with it the network complexity and computational time while still retaining the most salient features.

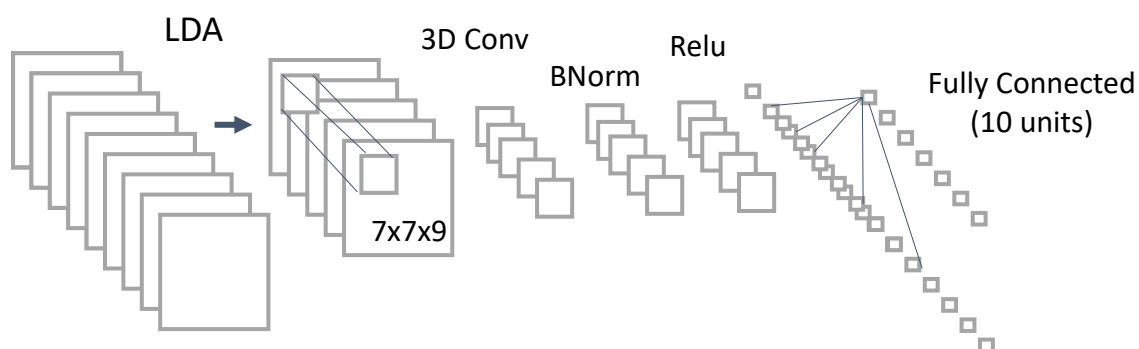


Figure 5-7: Schematic illustration of the structure of a CNN network

The convolutional neural network is then composed of two convolutional layers. Each of them followed by their corresponding batch normalization layer and Rectified linear (Relu) units. A 'Batch normalization' layer uses statistics of individual batches to re-normalize outputs of the previous convolutional layer, but it does not alter network geometry. A 'Rectified linear' unit is a simple transfer function that turns all negative values in zero and lets all positive values pass through. It is known to significantly improve convergence speed. We then add two fully connected layers at the end, one with

50 hidden units and the final one with 10 (identical to the number of classes). While the inner convolutional layers are performing the so-called feature extraction from the input images, the last fully connected layers are performing the classification of the corresponding features into one of the output labels or classes. (Yang et al. 2018).

We base our CNN parameter selection, in accordance with previous work (Paoletti et al., 2017; Chen et al., 2016; Al-Sarayeh et al., 2018) and opt for 16 convolutional filters of size 5x5, for an input block image of 7x7, a learning rate of 0.005, batch size of 100 and a maximum number of 40 iterations. We see experimentally that these parameters work well while still limiting the complexity of the network.

To choose the input block size we evaluate the impact of the selection of different image block sizes on the final classification accuracy. For this purpose, we test the use of image block sizes of 1x1, 3x3, 5x5, 7x7, 9x9 and 11x11 pixels on the full resolution Snapscan image (1048x1048 pixels).

The size of the convolutional filters chosen for the CNN network for the different input image block sizes are given in Table 5-1. The larger the image input block size taken the larger convolutional filter we can use, the limit being the input block size. We describe the convolutional filters here as 2D, but they have a third dimension, given by the number of spectral bands, in this case the 9 LDA bands. In the case of considering a 1x1 block size, this is, a single pixel, we want to exploit only the spectral information per pixel and not the spatial information or any spatial features. This is interesting to evaluate the amount of information which is present in the spectra or present in the spatial features in the image. For any larger image block size, the CNN uses the information from a pixel and its neighbouring pixels, therefore the spatial information is exploited as well.

Table 5-1: Input image block sizes versus convolutional filters used

<i>Block size</i>	<i>1x1</i>	<i>3x3</i>	<i>5x5</i>	<i>7x7</i>	<i>9x9</i>	<i>11x11</i>
<i>1st Conv Filter</i>	1x1	3x3	3x3	5x5	5x5	7x7
<i>2nd Conv Filter</i>	1x1	1x1	3x3	3x3	5x5	5x5

The larger the block size the more information we are giving as input to the network, in terms of input pixels. The network was trained with the same input pixels/training examples, which are the centre pixels of each input block. For instance, for a block size of 3x3, this corresponds to inputs of 9 pixels for every training example, resulting in a total of 3x3x9017 = 81153-pixel data. For the comparison we use the same number of network iterations for all block sizes and the same network architecture.

Post-processing techniques

We consider two different techniques to smooth the labelled images produced by the classifiers. The first and most simple one is median filtering, where median filters of 5x5 pixels are applied. The second technique is Bilateral Filtering. We used the Bilateral Filtering method as described in (Kang et al. 2013). In this method, first the probability maps from the classifier for every class label need to be extracted. This probability map is then bilaterally filtered based on a reference image. In (Kang et al. 2013) the reference image was created from the first 3 PCA components. In our case, we used as reference image the LDA bands, since in our case this shows better performance than PCA. This is in accordance as well with LDA performing better as pre-processing technique for the QDC classifier than PCA.

The probability maps per pixel are then bilaterally filtered according to the spatial and spectral similarity of a pre-defined block size around the pixel in the reference image. This way, the joint bilateral filter is based on the widely used Gaussian filter, considering the distance in the spatial domain and the distance or similarity in the spectral domain. The spatial and spectral distances are defined using two Gaussian decreasing functions, as described for the Joint Bilateral Filtering process

in (Kang et al. 2013). The main parameters to tune the bilateral filtering are δ_s and δ_r , defining the decay of these Gaussian functions, or weight decrease with respect to spatial distance and spectral distance (in terms of intensity similarity) respectively. In this sense, δ_r defines how the pixel weight decreases with the intensity difference while δ_s defines the size of the local window used to filter a pixel: Block size = $(2\delta_s + 1) * (2\delta_s + 1)$.

We explored the performance of these two parameters and set for the following parameter values according to the different spatial resolutions considered:

Table 5-2: Parameter selection per image size: input block size, and gaussian decay functions δ_s (wrt spatial distance) and δ_r (wrt spectral distance)

Camera Image	Image size	δ_s	δ_r	Block size
Snapscan original	1088 x 1048 pixels	3	4	7x7
Snapscan binned by 2	544 x 524 pixels	3	4	7x7
Snapscan binned by 4	272 x 256 pixels	1	0.4	3x3
Mosaic NIR	409 x 216 pixels	2	0.4	5x5
Mosaic VIS	512 x 256 pixels	3	4	7x7

As we can see in Table 5-2, different δ_s and block sizes are used for the different image resolutions considered. This can be related to the size of the seed spatial features in the different image resolutions. Table 5-3 shows how the approximate seed sizes for the smallest seeds relate to the image resolution used. We can see that the biggest seed sizes can be obtained for the Snapscan original and binned by 2 and the Mosaic VIS. The Mosaic NIR camera has only slightly lower spatial resolution than the Mosaic VIS. However, in our experiments the Mosaic NIR was placed slightly further from the scanned objects, and this causes it to image the seeds with roughly half the size of those in the Mosaic VIS.

We can see in Table 5-3 that the smallest seed size in pixels is related to a good performing value of block size where bilateral filtering around the central pixel is performed. This way, block sizes of 7x7, 49 pixels, are considered suitable for all image resolutions where the seed sizes are at least 100 pixels. For the Mosaic NIR and the Snapscan binned by 4 block sizes of 25 and 9 pixels respectively perform better since they correspond to a portion of an individual seed. In this sense, performing bilateral filtering over a too big block size would not be advantageous since the pixel labels would differ strongly within the same block size when a block size comprises different adjacent seed types.

Table 5-3: Approximate seed sizes in pixels for the considered image resolutions and corresponding suitable block size

Image	Spatial resolution	Sesame size	Millet size	Linseed size	Block size
Snapscan original	1088x1048 pixels	500 pixels	400 pixels	800 pixels	7x7=49
Snapscan binned by 2	544x 524 pixels	125 pixels	100 pixels	200 pixels	7x7=49
Snapscan binned by 4	272x 256 pixels	32 pixels	25 pixels	50 pixels	3x3=9
Mosaic NIR	409x 216 pixels	95 pixels	87 pixels	205 pixels	5x5=25
Mosaic VIS	512x 256 pixels	200 pixels	205 pixels	350 pixels	7x7=49

Moreover, next to previous parameters we need to define our distant metric from pixel i to neighbouring pixel j , $\|i - j\|$. For simplicity we choose it to be the Chebyshev metric (Cantrell, 2000). In our image, if the points i and j have Cartesian coordinates (i_1, i_2) and (j_1, j_2) , their Chebyshev distance is defined by equation (1) as:

$$D_{Chebyshev}(i, j) = \max(|i_1 - j_1|, |i_2 - j_2|) \quad (1)$$

Benchmark RGB color imaging

To benchmark hyperspectral imaging in the VNIR range (460-900nm) against regular colour imaging cameras we create RGB images from our hyperspectral image. This way, we can compare both imaging systems under the same system conditions: illumination, lens, and identical sample selection. We are aware that color cameras could be available at higher spatial resolution or SNR. However, we obtain the RGB image from our hyperspectral image since this allows us to evaluate the added value of hyperspectral imaging, while keeping all other parameters identical (spatial resolution, SNR).

To obtain the corresponding RGB image from the hyperspectral image we use XYZ parameter computation (Goodman, T.A 2012) from the Snapscan hyperspectral image. The CIE XYZ color space is a device-invariant representation of color. From the given spectrum, S , the illuminant function I , (here assumed E standard of theoretical equal energy radiator (Goodman, T.A 2012)) and the CIE color matching functions, we can obtain X, Y and Z color values. We can then transform these X, Y, Z values to RGB color components (International Colour Consortium 1999, sRGB).

To benchmark hyperspectral with respect to colour imaging we applied the same type of pre-processing, classification, and post-processing techniques to the RGB images as we applied to the hyperspectral images. The only difference is that, since we only have three bands in RGB images, there was no need to apply feature reduction with LDA. Therefore, the CNN was directly applied on the three RGB channels. Since the spectral information was limited to these three broadbands, input blocks 11x11 were used to exploit as much as possible the spatial information. The size of the convolutional filters was then chosen as given in Table 5-1.

5.3 Results and Discussions

5.3.1 Impact of illumination system

We compare the use of different illumination systems: halogen system, halogen with HDR and custom tunable LED system on the pixel classification accuracy for the QDC classifier and the Snapscan camera image. No other pre-processing or post-processing methods were used at this stage. Both mean pixel accuracy and minimum pixel accuracy (for the most challenging ingredient) are increased by better balancing the energy of the illumination system. This way, using HDR functionality on top of a halogen system increases mean accuracy from 70.4 to 73.2% and up for the most challenging class from 45.9% to 50.6%. The tunable LED system achieves the highest performance increase resulting in a 10% improvement in mean accuracy (reaching 81%) and up to 14% increase for the most difficult ingredient (59.5% versus 45.9% of halogen). This happens thanks to its more homogeneous spectral and spatial distribution, which is seen in a factor 6 reduction of the standard deviations of the spectral intensity over the white tile.

5.3.2 Impact of classifier and camera system

We analyse the effect of the image block size on the classification performance of the convolutional neural network for the Snapscan camera system under halogen illumination. To obtain a fair comparison, the same number of network iterations and the same architecture were used for all block sizes. We can observe in Table 5-4 that for a 1x1 block size the CNN performance increases the mean accuracy by 3% with respect to QDC classifier, even though no spatial information is exploited yet. With an increased block size, we increase further the mean and minimum pixel accuracies. The largest performance increase, 11% in mean accuracy, happens when going from a block size of 1x1 pixel to a 3x3 block size, since the network can then start to exploit spatial/spectral information of surrounding pixels. From 3x3 block size on till a 11x11 block size the performance increase is less noticeable, but there is still a total gain of around 5% in mean accuracy and 8% for the minimum accuracy (most

challenging ingredient). From a block size of 7x7 on, the gain is more limited (less than 1% in mean and 2% for the minimum). In terms of convergence time, we can see that for this block size a lower number of iterations required results in the minimum computing time required. A larger block size than 7 increases both network complexity and convergence time, therefore the 7x7 block size seems to be a good compromise and is used in all further experiments.

Table 5-4: Impact of input image block size on CNN performance (pixel accuracy) for an image acquired with the Snapscan camera under halogen illumination.

Block size	CNN feature size	Mean accuracy	Minimum accuracy	Iterations required	Convergence time (s)
1x1	9	73.3%	50.1%	35	90.0
3x3	9x9=81	84.6%	68.0%	35	87.0
5x5	25x9=225	87.9%	75.7%	35	94.3
7x7	49x9=441	89.1%	74.3%	25	75.6
9x9	81x9=729	90.0%	76.2%	25	101.0
11x11	121x9=1089	89.4%	71.0%	25	119.2

It should be noted that even the largest image block size considered, 11x11=121 pixels, is below the smallest seed sizes in our image, which is around 400 pixels for millet seeds. All other ingredients are bigger (e.g linseeds around 1000 pixels and oat flakes from 3000 pixels on).

In this respect, the performance of the CNN classifier with a 7x7 block size, is considerably higher than that of the QDC classifier, for all camera systems considered. The Snapscan system, with the highest spatial-spectral resolution, outperforms Mosaic camera systems, independently of the classifier: 70.4% as mean and 45.9% minimum for QDC, increasing to 89.1% mean and 74.3% minimum for the CNN. Both Mosaic systems, with a reduced spatio-spectral resolution and lower pixel SNR than the Snapscan camera, achieve poor performance with the QDC classifier (~45-50% in mean and 2-5% as minimum). However, their performance is considerably increased by the CNN, reaching 78.8% as mean and 50.7% as minimum for the VIS and 76.1% mean and 51.1% minimum for the NIR.

While CNNs have the potential to extract shape and size features (Szegedy et al., 2014), it is unlikely that our CNN implementation with 2 convolutional layers extracted much shape information. Moreover, our input block size was limited to 7x7=49 pixels, which cannot cover more than a fraction of even the smallest seeds. Therefore, most probably it is not extracting enough shape information per ingredient to rely on morphological information per seed as proposed by Vu et al. (2016) and Vermeulen et al. (2018). In contrast, our CNN is most likely relying on spatial textural information. Additionally, for less flat components such as soy grit, the presence of shade near the edge of the soy grit could be relevant information that the CNN might be exploiting. Moreover, to address an image containing multiple seeds of different size and shapes (e.g oat flakes versus millet seeds), this is probably not possible with one single size of convolutional filters, as used in our implementation. A different range of filter sizes may be required to optimally address different feature sizes. Finally, a combination of object segmentation and object classification tasks would probably be required, first to identify where seeds in the scene and then to analyze the shape at object level.

In this respect, Redmon et al. (2016) developed Yolo, a CNN with 9 to 24 convolutional layers with the purpose of pure object detection with high real-time performance. However, they did not extract object shape information. In contrast, CNNs from GoogLeNet (Szegedy et al., 2014) used a modified structure with several convolutional kernels of different sizes to capture features at different scales for an image classification task. More recently, Castorena et al. (2020) have addressed CNN modifications to be able to capture 2D – shape information since typically CNNs rely more on textural information, while Mishra et al. (2020) implemented CNN modifications to allow the network to extract 3D information. However, these latter works have addressed one single object per image.

Therefore, an image with multiple objects of varying size and shape, such as our application case, may require a combination of multiple different approaches and will incur in higher complexity than the CNN approach presented here.

Note that despite the potential of CNNs to include shape information, to discriminate heterogeneous ingredients in size and shape such as wheat bran or soy hull, the CNN would probably still need to rely more on spectral information.

5.3.3 Impact of pre-processing steps

Pre-processing for denoising by median filtering

We assess here the impact of applying median filters as pre-processing step to our classifiers for all camera systems with a halogen system. Identical training samples are used for the comparison of the different methods and accuracy is given over the whole image as test set. Median filtering as pre-processing step is a simple yet effective method to improve the classification performance. This is particularly the case for the QDC classifier with the Snapscan image. As we can see in Table 5-5, an increase up to 10% on mean accuracy and 16% on the minimum one can be achieved with a 5x5 median filter.

For the Mosaic VIS and Mosaic NIR images the median filtered applied is of 3x3, to avoid excessive blurring on these lower resolution images. Median filtering increases mean accuracy by 5-7% for the QDC classifier in both Mosaic systems. For the CNN there is also a 5% increase for the Mosaic VIS. For the Mosaic NIR CNN the performance decreases when median filtering is applied, which could be due to excessive image blurring for this lower resolution image.

Table 5-5: Impact of Median Filtering for the classification performance obtained with QDC and CNN on the images of seed mixes acquired with the Snapscan, Mosaic VIS & Mosaic NIR cameras

Camera Classifier & Preprocessing	<i>Snapscan, (Halogen)</i>		<i>Mosaic VIS, (Halogen)</i>		<i>Mosaic NIR, (Halogen)</i>	
	<i>QDC Mean/Min</i>	<i>CNN Mean/Min</i>	<i>QDC Mean/Min</i>	<i>CNN Mean/Min</i>	<i>QDC Mean/Min</i>	<i>CNN Mean/Min</i>
<i>None</i>	70.4%/45.9%	89.1%/74.3%	45.5%/2.3%	78.8%/50.7%	50.2%/5.6%	76.1%/51.1%
<i>MF</i>	80.8%/61.9%	88.8%/75.0%	52.6%/9.1%	83.0%/70.9%	55.3%/24.0%	70.0%/26.9%

Preprocessing for denoising by spectral/spatial binning

Applying spatial/spectral binning on an image can also help denoise the spectra. However, this is done at the cost of a reduced spatial or spectral resolution. We experiment with spatial and spectral binning of factor 2 and 4, on the Snapscan image (1048x1088 pixels). Figure 5-8 shows the impact of median filtering on a close-up of our seed image. We can see how filtering reduces the textural information.

No binning is performed on the Mosaic images since these ones have lower spatial-spectral resolution. Table 5-6 shows the impact of binning and median filtering on the classification accuracy with the Snapscan image and Halogen illumination. The use of binning increases classification accuracy for the QDC classifier up to 8.5% in mean and up to 16% for the minimum class accuracy. Therefore, it is another simple yet effective measure to increase performance. For the CNN classifier, with initial performance around 90%, the impact of binning is marginal. The benefit of binning being in this case that the memory and computational requirements for the CNN are heavily reduced (by factor 16 when binning by 4).

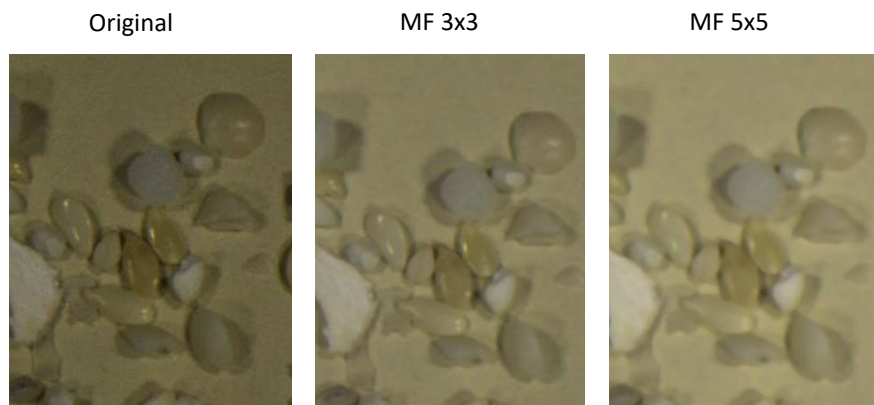


Figure 5-8: Impact of median filtering (MF) visualized on a close-up of the Snapscan image

As for the joint impact of binning and median filtering, we can observe that their individual performance increases do not add up when jointly applied. In fact, the highest performance increase is achieved by performing median filtering and not binning at all. The advantage of binning remains nevertheless, that a lower amount of data needs to be processed. This can be interesting when using the computing intensive CNNs. In this case, binning does not increase the performance of the CNN, but it heavily reduces computational and memory requirements while maintaining a similar performance.

Table 5-6: Joint impact of binning and median filtering as pre-processing on the mean and minimum classification accuracies obtained with QDC and CNN classifiers on seed images acquired with the Snapscan camera under halogen illumination.

Classifier/ Resolution	QDC Mean / Min	CNN Mean / Min
Original	70.4%/45.9%	89.1%/ 74.3%
Original + MF	76.0%/ 46.6%	89.5%/ 74.1%
Bin 2	72.2%/ 29.2%	90.5%/ 68.0%
Bin 2 + MF	74.4%/ 21.9%	90.6%/ 67.2%
Bin 4	76.4%/ 44.4%	87.9% /61.4%
Bin 4 + MF	77.6%/ 33.1%	87.6%/ 58.2%

Impact of post-processing steps: Median filtering and Bilateral filtering

We now evaluate the individual and joint impact of median filtering and bilateral filtering as post-processing steps applied on the labelled output image. The result of post-processing methods on the performance of the different camera systems is shown in Table 5-7. Bilateral filtering results in a higher performance increase than median filtering (11% versus 6% mean increase for Snapscan with QDC) at the cost of higher complexity. Combination of both, barely increases the performance. For the CNN there is also a modest performance increase by applying post-processing. The increase is less noticeable since the starting accuracy was high with lower potential for increase.

Table 5-7: Impact of post-processing steps on the mean and minimum classification accuracies obtained with QDC and CNN classifiers on images of seed mixes acquired with the Snapscan camera under halogen illumination and the Mosaic cameras under LED illumination.

Camera syst	Snapscan (Halogen)		Mosaic VIS (LED)		Mosaic NIR (LED)	
	QDC Mean / Min	CNN Mean / Min	QDC Mean / Min	CNN Mean / Min	QDC Mean / Min	CNN Mean / Min
None	70.4% /45.9%	89.1%/ 74.3%	52.5%/9.3%	80.5%/59.3%	49.4%/6.1%	83.1%/63.8%
MF	76.0% /46.6%	89.5%/ 74.1%	57.1%/11.6%	81.2%/59.9%	53.9%/8.0%	84.8%/66.0%
BF	81.5% /55.4%	90.3%/ 71.1%	59.3%/0.4%	83.2%/60.3%	49.4%/6.1%	83.1%/63.9%
BF + MF	81.6% /55.5%	90.3%/73.8%	59.5%/0.1%	83.3%/60.5%	53.9%/8.0%	84.9%/66.0%

These post-processing techniques correct miss-classified pixels by assuming most neighboring pixels are correctly classified. Otherwise, spatial filtering cannot correct for this poor classification and may make it worse. This specially occurs with Mosaic systems and QDC where some ingredient accuracies are below 10%. We can conclude that applying a pre-processing step to denoise the input spectra, is more effective than post-processing an already classified image with low accuracy and high number of miss-classifications, as in the Mosaic case.

Combined impact of pre-processing and post-processing steps

Table 5-8 shows the combined impact of the pre-processing and post-processing techniques with our QDC and CNN classifiers. In the case of QDC median filtering of 5x5 provides best results while in combination with the CNN, median filtering of 3x3 as pre-processing step is slightly preferable.

Table 5-8: Joint impact of pre- and post-processing techniques on the mean and minimum classification accuracies obtained with QDC and CNN classifiers on images of seed mixes acquired with the Snapscan camera under halogen illumination.

Pre & Post-processing + Classifier	QDC Mean / Min	CNN Mean / Min
Classifier	70.4% / 45.9%	89.1% / 74.3%
Classifier + MF	76.0% / 46.6%	89.5% / 74.1%
Classifier + BF	81.5% / 55.4%	90.3% / 74.1%
MF + Classifier	80.8% / 61.9%	88.8% / 75.0%
Classifier + BF + MF	81.6% / 55.5%	90.3% / 73.8%
MF + Classifier + MF	82.7% / 62.4%	89.1% / 74.8%
MF + Classifier + BF	85.4% / 66.3%	89.9% / 76.2%
MF + Classifier + BF +MF	85.5% / 66.6%	89.9% / 76.2%

From this table we can make several observations. Firstly, for QDC classifier, median filtering is more effective as pre-processing step than as post-processing step. Secondly, a pre-processing step such as median filtering achieves similar performance increase than bilateral filtering as post-processing step (around 10% for QDC). In addition, the joint use of median filtering as pre-processing and bilateral filtering provides further improvement even though the contribution of each individual performance does not fully add up (10% mean increase for each technique and 15% for the combination of both). For CNN, the conclusions are different though, the use of median filtering as pre-processing can even slightly decrease the mean accuracy. The reason might be that the blurring effect of median filtering decreases the spatial information provided to the CNN. Only the use of some post-processing (as BF) can slightly increase the performance (by 1%).

Combined impact of all system parameters

We now analyse the combination of all system parameters considered in previous sections: illumination system, pre-processing, analysis, and post-processing parameters for our two classifier types and different camera systems. Table 5-9 shows a summary of the basic configurations (only classifier without pre- or post-processing), those with pre and postprocessing methods (excluding binning) and the different illumination systems proposed for the Snapscan camera. Configurations illustrated in the same colour correspond to a similar performance achieved. Last row on Table 5-9 corresponds to the corresponding classification accuracy for the corresponding RGB image.

Table 5-9: Joint impact of system illumination and analysis methods on the mean and minimum classification accuracies obtained with QDC and CNN classifiers on images of seed mixes acquired with the Snapscan camera.

Configuration	Halogen Mean / Min accuracy	Halogen HDR Mean / Min accuracy	Tunable LED Mean / Min accuracy
QDC	70.4% 45.9%	73.2% 50.6%	81.1% 59.5%
MF+QDC+BF+MF	85.5% 66.6%	87.0% 68.5%	91.4% 70.7%
CNN	89.1% 74.3%	88.8% 77.7%	94.1% 86.0%
CNN+BF+MF	90.3% 73.8%	90.5% 80.2%	95.4% 87.5%
CNN+BF+MF (RGB)	67.6% 34.1%	- -	73.5% 35.6%

Figure 5-9 illustrates the preceding table showing which system parameters can be gradually added to increase the system performance. Starting from a basic configuration (QDC classifier, halogen system and no pre-post processing steps), we can considerably increase the performance, by up to 25% mean accuracy, till the most complex configuration (CNN classifier, LED system and pre/post processing). Moreover, different parameter configurations can be used to achieve similar performance (showcased in same color) while meeting different application requirements.

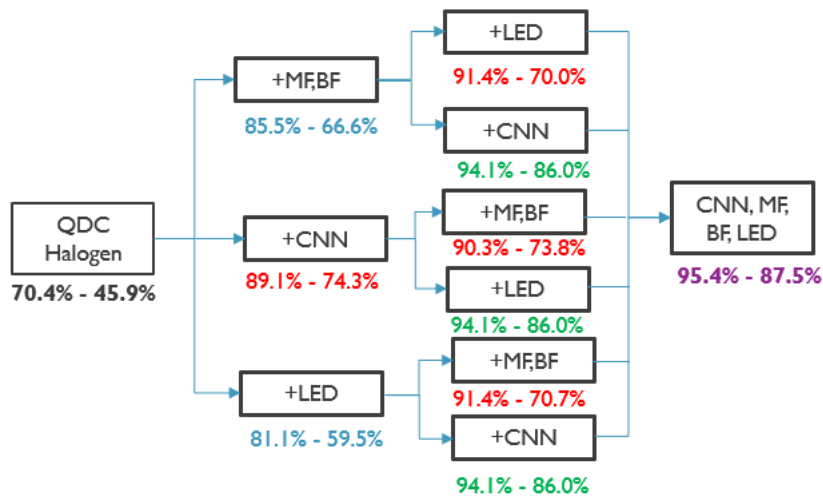


Figure 5-9: Suggested configuration map to increase system performance. Starting from a configuration with halogen lights and QDC classifier different components can be modified: use of CNNs (+CNN), use of pre- and postprocessing (+MF, BF), use of LED illumination (+LED) or a combination of them. Similar colors indicate similar accuracy levels.

This way, from the basic configuration (halogen system and QDC classifier) we can increase the accuracy to over 80% in mean and around 60% for the minimum by either:

- Combining MF, QDC and BF in the halogen-based system
- Using the basic classifier QDC without pre/post-processing but in the LED-based system

To further increase performance, to around 90% for mean and over 70% the minimum, we can either:

- Use CNNs, in combination or not with pre/post-processing.
- Use the LED-based system in combination with QDC classifier, pre- and post-processing (Median Filtering and Bilateral Filtering). This allows us to reach similar accuracy without resorting to CNNs.

The highest reachable performance is achieved by combining the following system parameters: CNNs, LED system and pre- and post-processing methods.

Finally, we benchmark the results with respect to RGB imaging in Table 5-9. For this purpose, we take the best possible configuration for RGB imaging of CNN's in combination with post-processing. Even though the use of LED illumination also benefits RGB by around 6% in mean accuracy we can see that hyperspectral imaging outperforms RGB imaging even when comparing to the pixel-based approach of QDC, even by a 10% in the minimum accuracy. When compared to the same analysis method, CNN, hyperspectral outperforms by 20% on the mean accuracy and around 40% on the minimum accuracy.

To visualize the effect of these different system aspects on the classification accuracy we show the classified images for the Snapscan binned by 2 case. Figure 5-10 shows the impact of the classification accuracy on the resulting classified images for some of these configurations. Figure 5-11 shows a crop of the original seed image with its corresponding classified images. For some seeds, the QDC has many pixel miss-classifications (circled in red), which make the seeds unrecoverable even after majority vote in a seed. The use of median filtering prior and after classification helps to increase the accuracy in some cases but fails in others. Indeed, the central part of the image shows one miss-classified sesame seed, miss-classified soy hull and soy grit wrongly detected as either millet or corn. This is corrected in the images acquired with the LED system and classified with the CCN, where the right type of seeds is correctly discriminated.

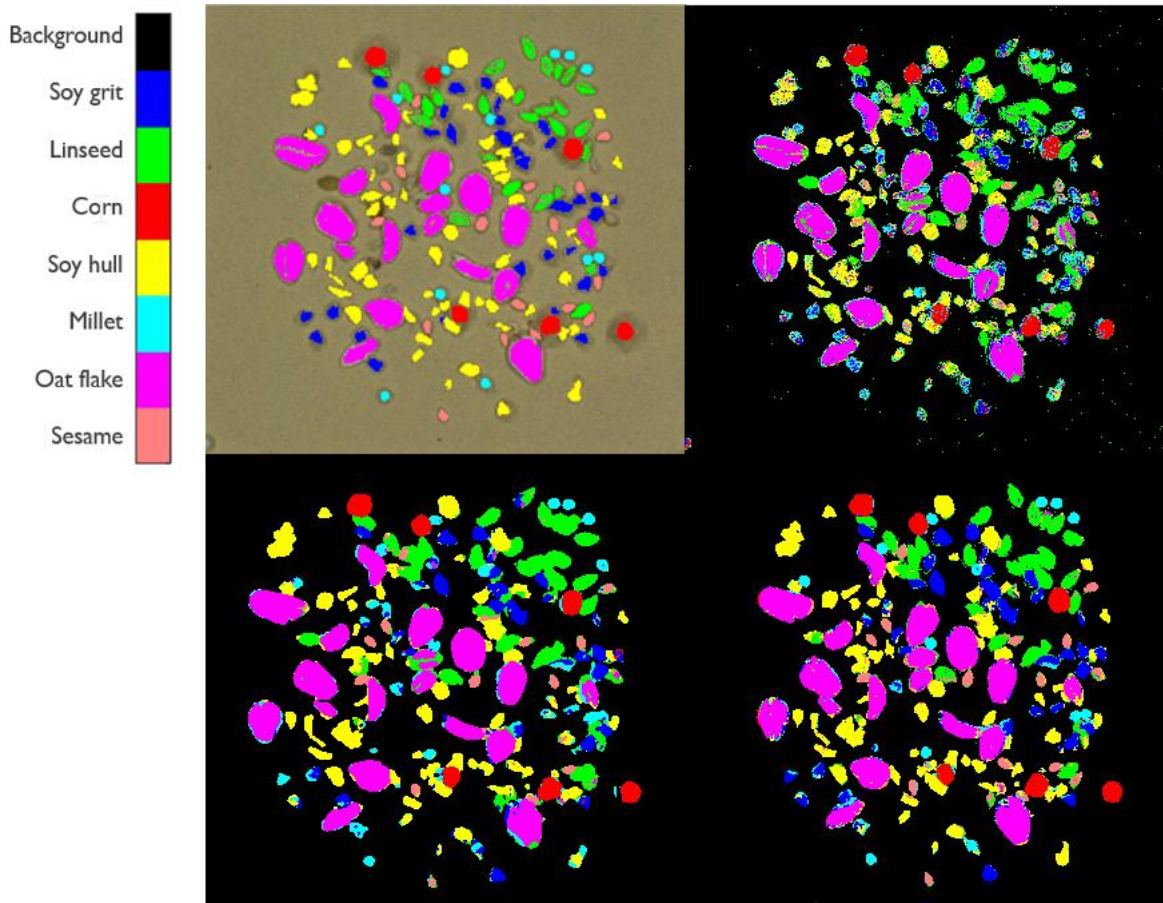


Figure 5-10: False color image of seeds with labelled ground-truth (top-left), classified image for halogen illumination with a QDC classifier without (top right), and with (bottom left) median filtering, and for the combination of LED illumination with a CNN (bottom right).

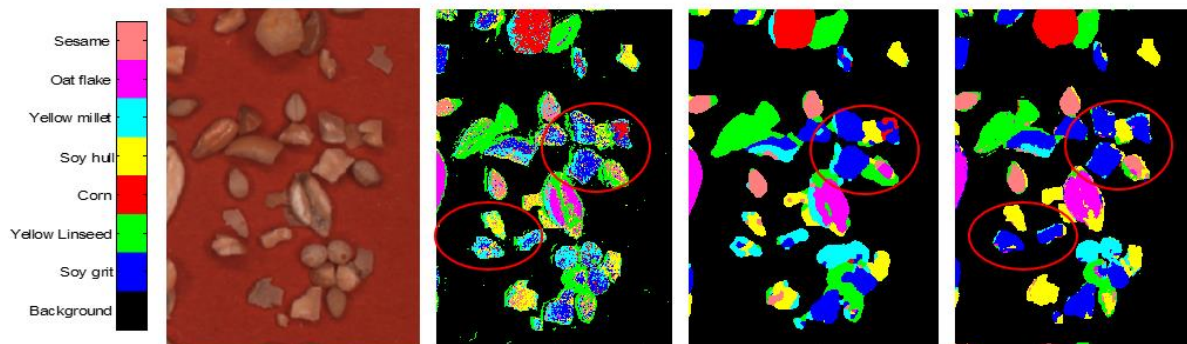


Figure 5-11: Close-up of Figure 5-10 and corresponding classified images, left to right with a) Halogen QDC, b) Halogen (MF+QDC+MF) and c) LED system and CNN.

Table 5-10 shows the performance of selected system configurations for the Mosaic VIS and the Mosaic NIR, respectively. In both cases the basic configuration with a pixel-based classifier (LDA+QDC) obtains poor performance. However, by modifying some system parameters that either reduce the spectral noise (MF, LED) or exploit more spatial information (CNNs), the performance can be dramatically increased (35 to 45% mean accuracy increase and up to 70% increase in minimum accuracy) achieving then very high performance with both Mosaic VIS and NIR. Note that median filtering is applied as pre-processing step on the image obtained with the Mosaic VIS and CNNs but not on the image obtained with the Mosaic NIR and CNNs. In this case no median filtering is applied

since this reduces the overall performance, probably due to the excessive loss of texture information, as it was seen in Table 5-5.

Table 5-10: Joint impact of system illumination and analysis methods on the seed classification performance for Mosaic cameras

Camera	Mosaic VIS		Mosaic NIR	
	<i>Halogen Mean / Min</i>	<i>Tunable LED Mean / Min</i>	<i>Halogen Mean / Min</i>	<i>Tunable LED Mean / Min</i>
<i>QDC</i>	45.5%/2.3%	52.5%/ 9.3%	50.2%/ 5.6%	49.4%/ 6.1%
<i>MF+QDC+BF+MF</i>	56.8%/ 0.7%	65.0%/ 7.9%	60.1%/ 32.1%	62.6%/ 43.2%
<i>CNN</i>	78.8%/50.7%	80.5%/ 59.3%	76.2%/ 51.1%	83.1%/ 63.8%
<i>(MF)+CNN+BF+MF</i>	87.6%/75.6%	90.3%/ 75.1%	77.8%/ 52.5%	84.9%/ 66.0%

It is important to note that LED illumination can help increase performance significantly in either Mosaic VIS or NIR range. This is also the case for the CNN classifier, where over 10% accuracy increase is achieved for the most challenging ingredients. The use of pre- and post-processing techniques can also increase the performance by over 10% in mean accuracy. However, for this application to reach a mean classification accuracy around 80% with the mosaic cameras, CNNs are required, exploiting both spectral and spatial information. Once a CNN is enabled, a more equivalent performance can be obtained from either adding LED illumination or pre/post-processing. For a mean classification accuracy closer to 90%, we would need to resort to the optimal configuration combining LED illumination, pre-processing through median filtering, a CNN classifier and post-processing. The most performing configuration under all illumination systems and cameras is achieved by using CNN, median filtering as pre- and post-processing and bilateral filtering. Only for Mosaic NIR images with CNN, due to the reduced spatial resolution, the optimal configuration does not use median filtering as pre-processing step.

Figure 5-12 shows an example of a classified image for the Mosaic VIS under different system settings. We can see how QDC poorly discriminates most seeds, while using CNN (bottom left) enables correct discrimination of the different ingredients with a mean accuracy close to 80%. The use of LED lights and extra pre- and post-processing on CNN (named as CNN+) further improves the classified image reaching up to 90%pixel classification accuracy.

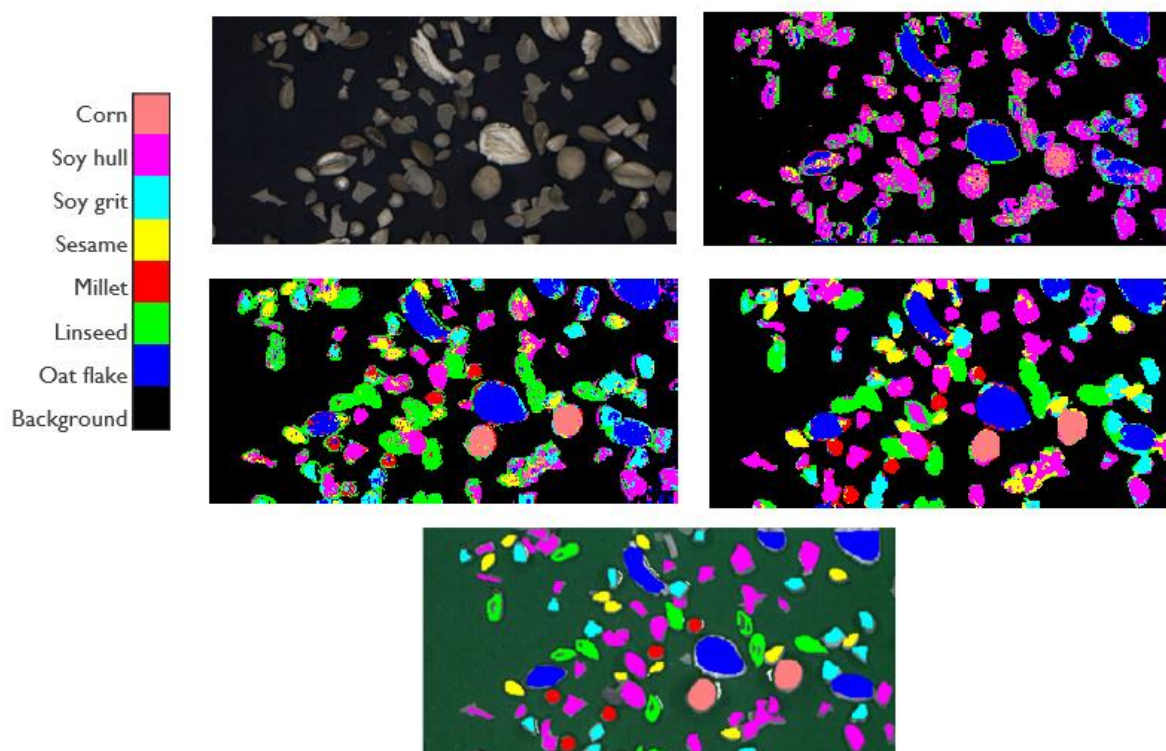


Figure 5-12: Classified images for illustration of the classification performance obtained on images acquired with the Mosaic camera in the Vis range. (Top row: False color image (left) and classified Halogen QDC+(right), Middle row: classified Halogen CNN (left) and classified LED CNN+ (right), Bottom row: manually masked ground-truth image)

5.4 Conclusions

In this chapter, we proposed a methodology to find the optimal combination of several system parameters that allows to increase our hyperspectral system performance, measured as pixel classification accuracy. We compared the impact of different parameters of a hyperspectral imaging system, such as illumination, camera, and analysis methods. From our experiments we observe that illumination is a key aspect of a hyperspectral system since a customized led system can increase accuracy over a traditional halogen system in the order of 10% in mean accuracy and close to 15% for the minimum accuracy. In addition, the use of pre-processing and post-processing methods (such as median and bilateral filtering) can also increase the accuracy significantly: over 10% in mean, and around 20% for the minimum accuracy for a pixel-based classifier but also around 1-3% the minimum accuracy in the CNN case. The impact of using an image-based versus a pixel-based classifier is even more noticeable for our application, where an increase in 15-20% mean accuracy can be obtained with respect to our pixel-based classifier. In total, the mean pixel classification accuracy for the Snapscan camera increased from 70% to 95% by replacing the basic combination (halogen illumination with quadratic discriminant classification and no pre/post processing) by the most advanced one: tunable LED illumination with a convolutional neural network and pre/post-processing methods applied. For more portable low-resolution Mosaic cameras, enabling all system parameters in this advanced configuration can noticeably increase our application mean pixel accuracy from 50% to over 90%.

Our system analysis has shown that similar performance can be achieved by enabling a different set of system parameters. For instance, we can reach the same performance than a CNN under halogen lights by using a QDC classifier and enabling tunable LED illumination and the use of pre- and post-processing techniques. This specific system trade-off is valid for the application considered. A basic

system with QDC and halogen lights might suffice to reach the highest accuracy in another application. Similarly, a tunable LED illumination providing more balanced spectral and spatial distribution is beneficial, but its advantage could be more limited for a different sensor or camera system. Another important aspect is the degree of spatial and spectral information available in our application. The more information available in the spatial dimension the more beneficial a joint spatial-spectral analysis with CNN will be with respect to a purely spectral pixel-based analysis such as QDC. This is application dependent. In addition, a higher degree of spatial information in our application motivates benchmarking with respect to color cameras. For instance, in our case, high spatial resolution RGB color imaging with LED illumination and CNN classification could achieve similar or higher performance than with a low-resolution Snapshot hyperspectral camera with pixel-based classification.

A way to assess whether the classification mainly relies on the spatial or spectral dimension could be the following: If we can discriminate the different objects/classes reasonably well by visually inspecting an RGB image corresponding to the hyperspectral image, then there is either a certain degree of spatial information present or the problem can be solved with regular color imaging. Moreover, in this case discrimination based on color images could still provide reasonable accuracy. In this sense, there is generally some degree of spatial information available in the image since neighboring pixels typically belong to the same objects/materials. On the other hand, we can evaluate the degree of spectral information available in the image by analyzing the performance of a pixel-based classifier such as QDA, where no spatial information is exploited.

The existing performance-complexity trade-offs between high-resolution and low-resolution camera systems often hold for a generic hyperspectral system. This said, for some applications a low-resolution system may suffice to reach the application target performance. A general conclusion that can be drawn is the need for a joint study of all system parameters. By performing this joint analysis, we can enable the system parameters that better fit the application requirements in terms of performance, spatial resolution, computation cost or speed of acquisition. Therefore, system-wide analysis can lead to better decisions when adapting to the specific application requirements.

Chapter 6

Adding wavelength range to the joint system evaluation of hardware, illumination, and data analysis

In this Chapter, we extend the system aspect analysis covered in Chapter 5 by introducing, as in Chapter 2, the wavelength range as a system parameter with high impact on the system cost. To this end, we study the impact of the SWIR camera hardware (1100 – 1700 nm range) on the Devil’s triangle of performance – cost – complexity for the same seed application used in previous chapters.

By considering, in addition to the VNIR range, cameras in the SWIR range it might be possible to increase discrimination performance. This would then happen at the expense of a camera system cost increase since sensors in this range are typically more expensive. In addition, SWIR sensors offer lower spatial resolution (typically VGA). On the other hand, their potentially higher discrimination power may help to reduce the associated processing complexity. This is the case if, for instance, pixel-based classification suffices to attain the required performance and more advanced processing methods such as CNNs are not needed. In this chapter, both types of SWIR camera systems are considered: Snapscan cameras with high spatial-spectral resolution and Mosaic snapshot cameras with lower spatial-spectral resolution.

Figure 6-1 shows the focus of our Devil’s triangle in this chapter on Performance and System Cost where RGB, VIS/NIR and SWIR range systems are considered in both high spatio-spectral resolution (Snapscan system) and low spatio-spectral resolution (Snapshot system).

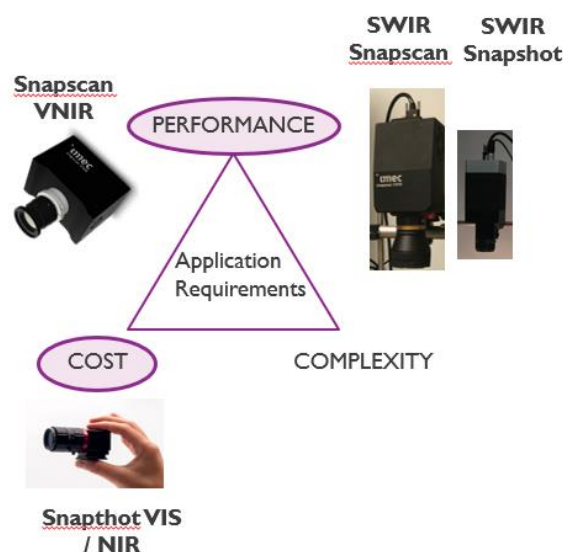


Figure 6-1: Devil’s triangle of application requirements considering different camera wavelength ranges.

6.1 Materials and Methods

6.1.1 Camera systems

Recently, the on-chip hyperspectral imaging technology has been extended to cover the short-wave infrared (SWIR) range between 1100 and 1650 nm (Gonzalez et al., 2018). Figure 6-2 shows the corresponding Snapscan camera system with its main characteristics, being 100 bands in the 1100 to 1700 nm range and a maximum spatial resolution of 1200 x 640 pixels.

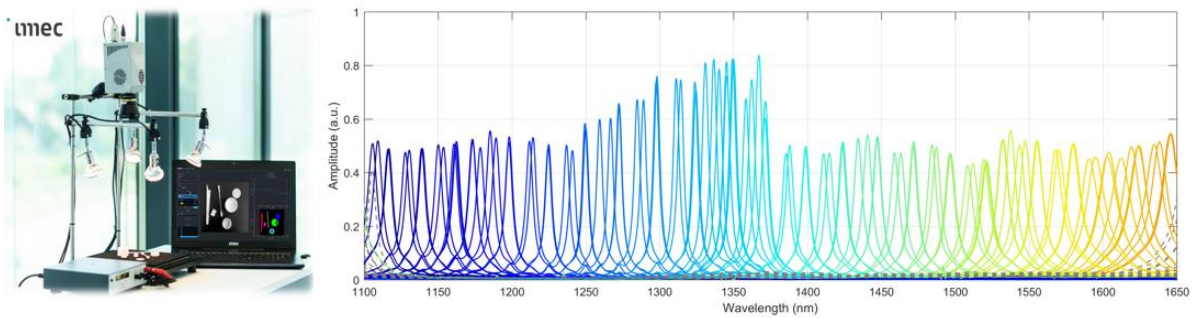


Figure 6-2: Compact Snapscan SWIR camera system (left) and measurement after calibration of its 100 spectral bands in the 1100-1700 nm range. - Courtesy of Imec

Similarly, Mosaic SWIR Snapshot cameras have also been developed to enjoy the benefits of mosaic snapshot cameras at the expense of a reduced spatial-spectral resolution with respect to the Snapscan SWIR camera system. This way, the Mosaic SWIR camera system used for this study offers 16 bands at a spatial resolution of 128 x 160 pixels. The lay-out of the 16 bands selected in the 4x4 Mosaic SWIR design is illustrated in Figure 6-3.

1.30 um	1.32 um	1.34 um	1.36 um
1.38 um	1.40 um	1.42 um	1.44 um
1.46 um	1.48 um	1.50 um	1.52 um
1.54 um	1.56 um	1.58 um	1.60 um

Figure 6-3: Band selection and distribution in 4x4 Mosaic SWIR sensor

Both camera systems were used with halogen lights since no high-power LEDs in the SWIR range were commercially available at the time of the study.

Figure 6-4 benchmarks these SWIR range camera systems with respect to the VNIR systems used in previous chapters by illustrating the Spatial – Spectral resolution tradeoffs that can be expected from each of the camera systems considered. While RGB cameras could offer higher spatial resolution than hyperspectral cameras, their spectral resolution is very low. Although this is application dependent, the SWIR range is considered to contain more detailed chemical information. Therefore, we could expect our SWIR Snapscan camera to offer the highest spectral discrimination and an average spatial resolution, comparable to that of Mosaic VIS/NIR cameras. A Snapshot SWIR camera would provide lower discrimination power than the Snapscan SWIR, but it may be comparable or even better than

that of a VNIR Snapscan camera for specific applications such as the seed discrimination application of Chapter 3 to 5, in which both VNIR and SWIR ranges are discriminative.

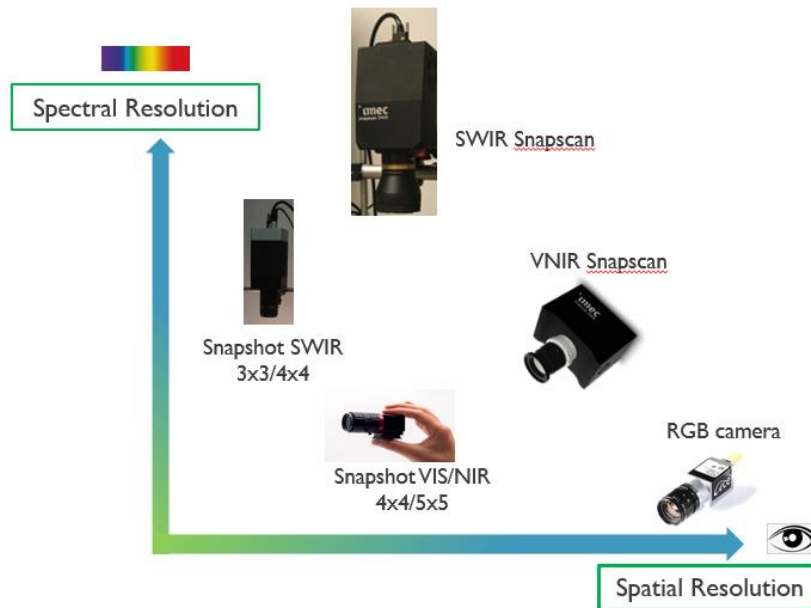


Figure 6-4: Tradeoffs in Spatial-spectral resolution provided for this particular application with the different camera systems used in this research.

6.1.2 Sample selection and processing pipeline

To evaluate these trade-offs, we used the same seed application with the ingredients presented in Chapter 4 and 5. Similar to the procedure followed in the previous chapters, half of the image was used for training the algorithms, while the other half was used for the validation. As the seeds were not so homogeneously distributed, we made sure that training and testing pixels are selected from different groups of seeds in the lower resolution image (Mosaic camera) by manually selecting different masks with different seed selection for training/testing. The created image ground truth with all seeds was used to compute the classification accuracy.

The Mosaic SWIR 4x4 image was upsampled from a resolution of 128 x 160 per band to obtain the original sensor resolution of 512 x 640 pixels. This was done to increase the size of the spatial features of our Mosaic SWIR image to a size comparable that that of the camera systems in the VNIR range, presented in Chapter 5.

The data analysis pipeline used in Chapter 5 for the VNIR range images was also used for processing these images in the SWIR range: median filtering 3x3 as pre- and post-processing technique, LDA as pre-processing band selection method, the pixel-based QDC classifier and the CNN to implement the joint spatial-spectral analysis. As the upsampled Mosaic SWIR image has similar spatial features as the Snapscan VNIR image, the CNN parameters optimized for the Snapscan VNIR image, as provided in Table 5.2 in Chapter 5, were also used here.

Similar to Chapter 5, all analyses were performed in Matlab and PerClass.

6.2 Results and discussion

The mean reflectance spectra of the seed ingredients are illustrated in Figure 6-5 for the Snapscan SWIR and the Mosaic SWIR cameras. We can see how the Mosaic SWIR 4x4 band selection is restricted to the 1300 to 1600 nm range (marked by the dotted vertical line), and this eliminates some interesting features around 1200 nm.

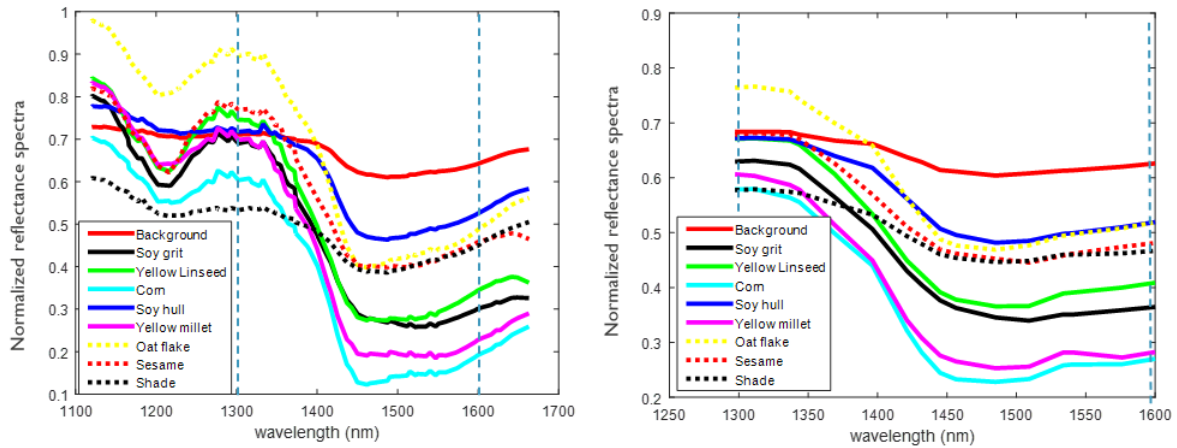


Figure 6-5: Normalized mean reflectance spectra for different seed types acquired with the Snapscan SWIR (left) and Mosaic SWIR (right) hyperspectral cameras.

Table 6.1 summarizes the performance in terms of mean and minimum pixel accuracies per camera system: the ones in the VNIR range presented in Chapter 5 and the additional camera systems in the SWIR range. The Snapscan SWIR camera provides the highest pixel-based accuracy, which is comparable to the one obtained with the VNIR Snapscan system under tunable LED illumination in combination with a CNN approach. Similar to the Mosaic Vis and NIR systems, the Mosaic SWIR system requires a spatial-spectral approach to achieve higher performance. However, even for the QDC classifier the 4x4 Mosaic SWIR system achieves clearly better pixel accuracy than the Mosaic VIS and NIR systems with a similar number of bands. This suggests that the SWIR range (1100-1600 nm) is more discriminative than the VNIR range (450-900 nm) for this application.

Table 6-1: Mean and minimum pixel classification accuracies for different combinations of illumination system, hyperspectral camera classifier.

	RGB LED	LED + Mosaic VIS 4x4	Halogen +VNIR Snapscan	LED + VNIR Snapscan	Mosaic SWIR 4x4	SWIR Snapscan
QDC	67.6% 34%	52.5% 9.3%	70.4% 45.9%	81.1% 59.5%	84.9% 60.0%	97.0% 92.7%
CNN	73.5% 35%	90.3% 75.1%	89.1% 74.3%	94.1% 86.0%	95.8% 86.9%	-

The false color and classified image for the Snapscan SWIR image are illustrated in Figure 6-6. A cleaner per-pixel classification can be seen with respect to VNIR images despite the lower spatial resolution.

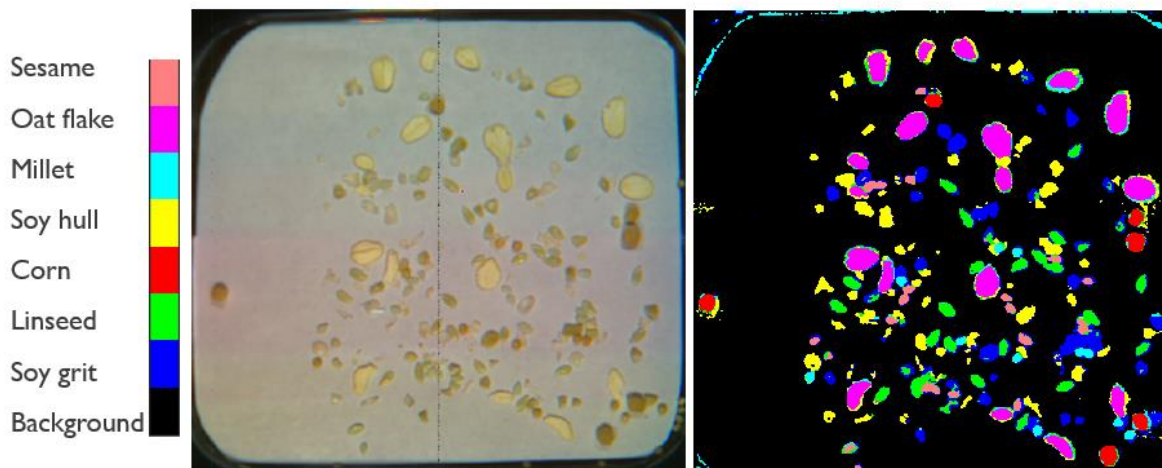


Figure 6-6: False color image (left) and classified image (right) for a seed mix acquired with the Snapscan SWIR camera.

In Figure 6-7 the Performance – Cost tradeoffs for the different camera systems are visualized. Performance is quantified in terms of the minimum and mean per-pixel classification accuracy, while the systems have been ordered from lower to higher hardware cost along the X-axis.

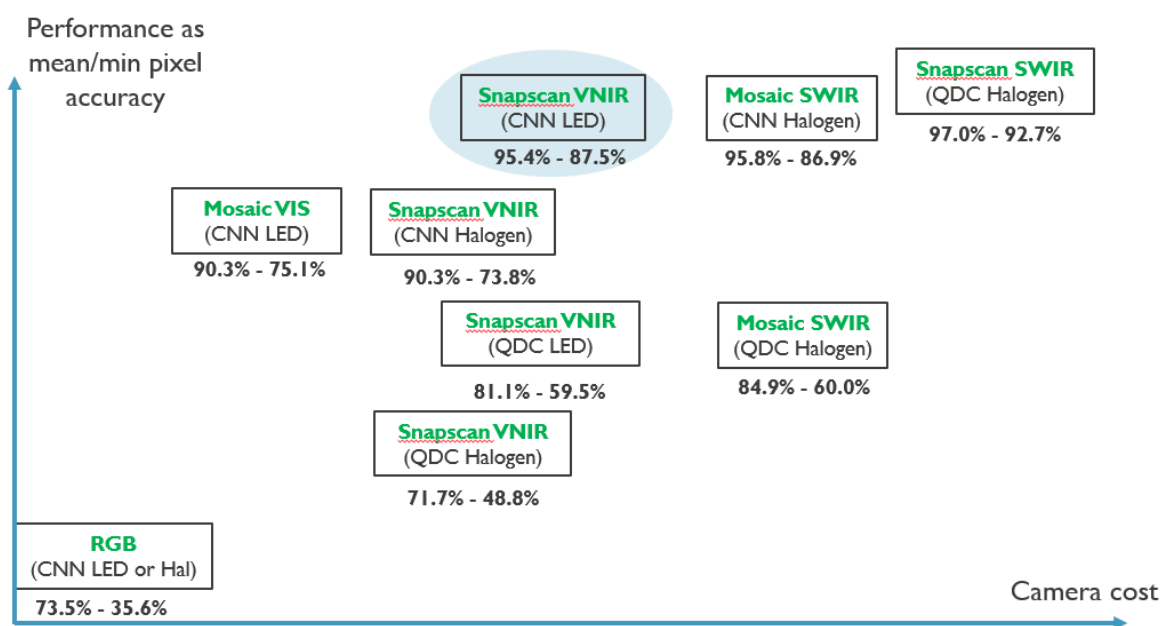


Figure 6-7: Performance – cost tradeoffs for all camera systems considered.

Before deciding on the practical implementation, several system tradeoffs such as Performance – Cost tradeoffs have to be made. Depending on the performance and cost requirements different system configurations (combination of camera system, illumination system, data analysis) will offer the most suitable tradeoff. For instance, while the most economical option would be to opt for a color camera, this would most likely not meet the required discrimination requirements. On the other hand, the option with the highest discrimination power would be the use of a Snapscan camera in the SWIR range. However, a more cost-effective choice could be to use a Snapscan camera in the VNIR range, preferably with LED illumination and image-based data analysis (CNN).

At this point, Snapscan VNIR is a more cost-effective option than Mosaic SWIR unless acquisition speed plays an important role. Moreover, the spatial resolution provided is higher for the Snapscan VNIR camera and this allows to image more product in one single scan.

Other system aspects such as system complexity have not been addressed in this study. While we could generally assume that pixel-based classification (QDC) will be simpler to implement and require a lower amount of training data than CNN-based classification, a more in-depth study of these implementation aspects would be required. Similarly, the impact of the spatial resolution offered by each camera system has not been considered yet. In this respect, a camera system with higher spatial resolution brings a two-fold advantage: increased spatial information and also the capacity of covering a larger amount of material/product in one single scan.

6.3 Conclusion

In this chapter the wavelength range dimension has been added to the evaluation of the system trade-offs discussed in the previous chapter. We have shown that this is a key parameter which influences both camera system cost and discrimination performance. Therefore, it enables new system tradeoffs. For the application considered the most performing configuration is that of the Snapscan system in the SWIR range, reaching the highest discrimination accuracy without resorting to convolutional neural networks. Since the Snapscan SWIR is also the most expensive camera system a more cost-effective camera system choice is the Snapscan VNIR system, that reaches very similar performance with the help of a LED illumination system and CNNs but at a lower system cost.

In general, if there is a high degree of information in the spatial domain it may be worth considering the VNIR range instead of the SWIR range since we may have higher spatial resolution available there. On the other hand, if most of the information can be found in the spectral dimension and our camera hardware does not achieve enough discrimination, it might be advisable to consider camera hardware in a different wavelength range.

Chapter 7

Conclusions and future work

In this PhD dissertation, the **most relevant parameters in a hyperspectral imaging system**, namely the illumination, camera hardware and analysis methods, have been studied. The impact of each key element on the performance accuracy has been assessed in a joint evaluation of all system parameters.

In chapter 2, it was hypothesized that the wavelength range is an important system parameter since it enables system tradeoffs such as a reduction of the hardware cost. This was evaluated for a textile sorting application, where costly equipment in the SWIR range is typically used. However, we demonstrated on a limited number of samples that this camera hardware could be replaced by a lower cost camera in the VNIR range with higher spatial resolution. Achieving the required performance in this range, which has generally lower discrimination power for this application than the SWIR range, involved using a different data analysis approach. Extending this work by measuring a higher number of samples and more textile mixes would be advisable. However, current VNIR discrimination power can already be useful for increasing the number of textile sorting points at a lower cost. In addition, it offers the advantage of a better discrimination of denim textile, which is one of the most important materials for textile recycling. In this sense, it is worth exploring the suitability of different wavelength ranges or camera hardware when this can enable new tradeoffs at the application level, such as lower cost or higher acquisition speed. Typically, this exploration of other camera hardware options may trigger to shift complexity to the data analysis.

Chapter 3 introduced our main application case of seed mixture quantification and showed the impact of the data analysis techniques such as preprocessing and pixel-based classification where only spectral information is used. In this respect, benchmarking with respect to color imaging is important since this may reach the application requirements at a lower cost. For instance, depending on the seed ingredient selection, RGB imaging could offer enough discrimination power. Moreover, we showed that the use of data preprocessing and the integration of spatial information with the spectral information can be useful to increase the system performance and reach the application targets.

In Chapter 4, it was shown that the illumination system is one of the key elements in a hyperspectral imaging system. In addition, it was observed that both spectral and spatial homogeneity of a light source are required qualities in order to maximize the system's performance. In this respect, achieving suitable system illumination is more challenging in the case of Snapshot imagers. Ideally, the light source would also be customized to fit the sensor requirements.

In Chapter 5, our hypothesis that all system parameters should be jointly evaluated has been confirmed. In this respect, system parameters such as camera hardware, illumination system and data analysis methods had to be considered. This allowed us to find the best combination of system parameters and explore different tradeoffs at system level. This way, we have shown how different system configurations can be used to offer different performance-cost-speed tradeoffs to best match the application requirements. It was also shown that the same performance may be achieved with different system configurations. For example, in our specific application a configuration with a basic

pixel-based classifier and a high-quality illumination system achieved the same performance as a configuration of more basic halogen illumination with more advanced image-based processing.

Finally, in Chapter 6, wavelength range has been added as an additional system parameter to the joint evaluation of camera hardware, illumination system and data analysis methods performed in Chapter 5 by considering camera hardware in the SWIR range. This way, for the application considered, the Snapscan SWIR system reaches the highest discrimination performance at the expense of a higher system cost while the Snapscan camera system in the VNIR range remains the most cost-effective choice.

While the performance obtained with a certain system configuration depends on the specific application, the existing performance-complexity trade-offs between high-resolution and low-resolution camera systems holds for a generic hyperspectral system. For some applications, a low-resolution system may suffice to reach the application target performance. Another important aspect is the degree of spatial and spectral information available in our application. The more information available in the spatial dimension the more beneficial a joint spatial-spectral analysis with CNN will be with respect to a purely spectral pixel-based analysis such as QDC. Similarly, to increase the SNR of the system, trading-off spatial resolution (if enough available) by SNR can be considered. This can be done by spatial binning or even median filtering. Alternatively, the camera distance can be shortened to increase the spatial resolution. Moreover, HDR mode and averaging of images (increasing acquisition time) can be used or a better illumination system such as a customized tunable LED system (impacting cost and possibly acquisition time again) can be implemented. A last and most costly option may be to upgrade the camera system to one providing higher resolution and SNR, such as going from a Mosaic camera to a Snapscan camera. Finally, benchmarking with respect to color imaging is advisable, especially when a considerable portion of the information may be present in spatial features. For instance, in our application, high spatial resolution RGB imaging with LED illumination and CNN classification could achieve similar or higher performance than with a low-resolution Snapshot hyperspectral camera with pixel-based classification.

Figure 7-1 shows the different guidelines that can be followed depending on a) whether the information resides mostly on the spectral dimension or on the spatial one and b) the available spatial and/or spectral resolution of the chosen camera hardware. For instance, if the application relies strongly on **spatial information** and the camera has high enough spatial resolution, it makes sense to benchmark it with an RGB camera, since this might provide sufficient discrimination and be more cost-effective. Similarly, image-based processing will be more suitable than pixel-based processing if there is a higher degree of spatial information than spectral information.

However, if most of the information is on the **spectral axis**, instead of the spatial one, a camera hardware of high spatial resolution will not be as relevant, but this extra availability of pixels can be used to increase the SNR by averaging the spectra acquired over different pixels (binning, median filtering). Having a low spatial resolution camera will not trigger in this case any action to increase performance and it is therefore excluded from the guidelines. In addition, when the information resides mostly in the spectra it makes sense to improve the illumination making it more spectrally and spatially balanced, both in case of higher or lower spectral resolution.

When information is present in **both spectral and spatial domains** a mix of previous guidelines is applied. In this case, however, we have to find the right balance between sacrificing spatial resolution to increase SNR and retain sufficient spatial information for successful spatial analysis. It should also be noted that improving the illumination system may always be beneficial, but especially when the information is mainly in the spectral domain.

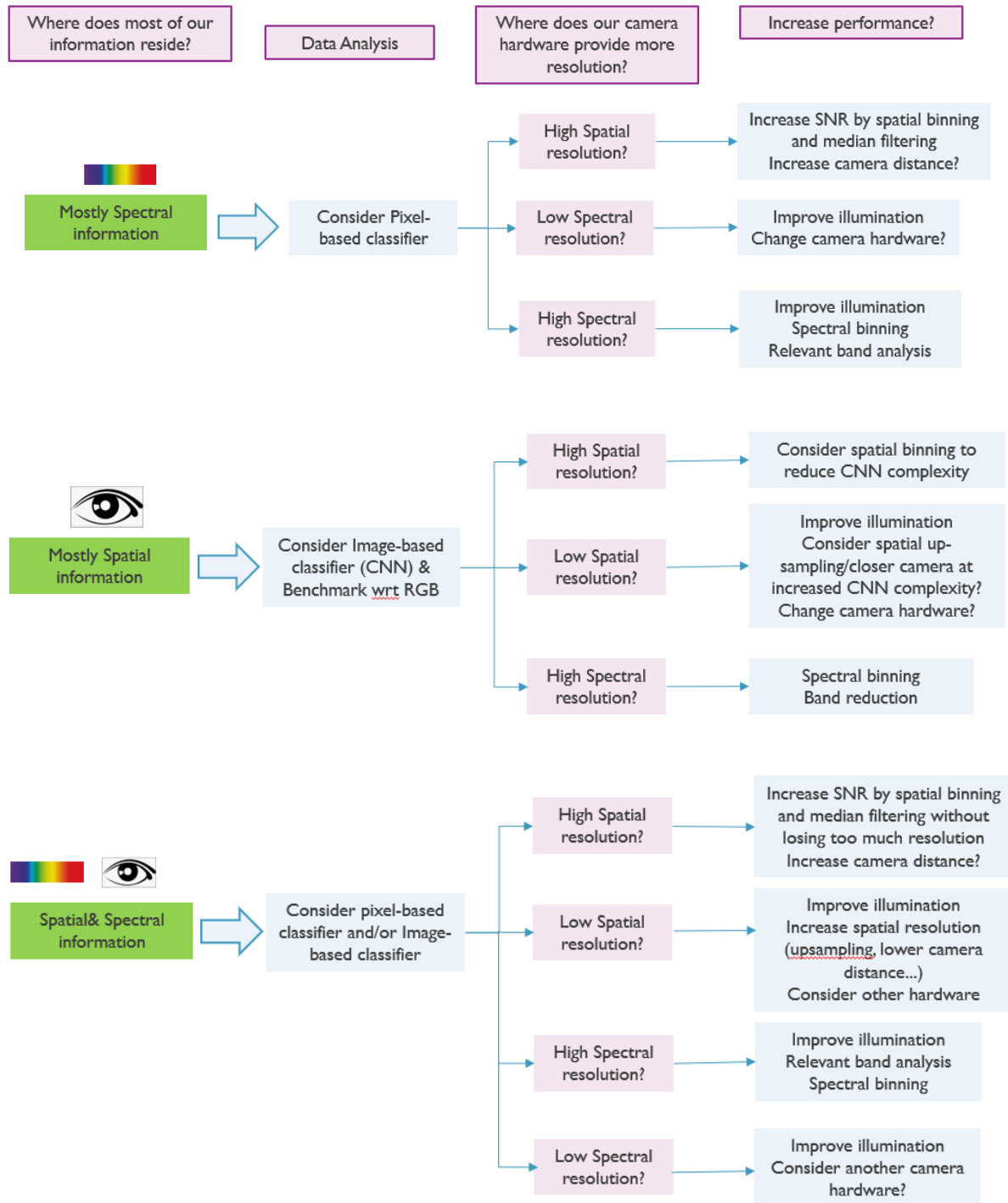


Figure 7-1: Guidelines for system-wide performance optimization

The information in our application may rely mostly on the spatial or spectral domain. However, our camera hardware may not offer enough spatial or spectral resolution. Next, different approaches can be followed to further either increase our spatial or spectral resolution. To artificially increase the spatial resolution of our camera we can spatially up-sample the image as a pre-processing step or/and reduce the camera distance. This will increase the physical resolution in the image at the cost of a lower subsampling capacity. Another alternative is to change the camera hardware from a Mosaic Snapshot to a Snapscan system for instance, which will lower the acquisition speed and increase the system cost. When the spectral resolution of the camera system is not sufficient, it may be possible to

increase the discrimination power by either relying more on spatial analysis (e.g CNNs or spatial post-processing instead of pixel-based analysis). Alternatively, another approach, with higher impact on the system cost and speed is to modify the camera hardware by using a different wavelength range (e.g SWIR system instead of VNIR one) or going from a Mosaic system to a Snapscan one with higher number of spectral bands.

As we have seen, it is important to assess the relative proportion of spatial and spectral information available in the image since this can motivate later system configuration aspects. A way to assess whether the classification mainly relies on the spatial or spectral dimension could be the following: If we can discriminate the different objects/classes reasonably well by visually inspecting an RGB image corresponding to the hyperspectral image, then there is a certain degree of spatial information present. Moreover, in this case discrimination based on color images could still provide reasonable accuracy. In this sense, there is generally some degree of spatial information available in the image since neighboring pixels typically belong to the same objects/materials. On the other hand, we can evaluate the degree of spectral information available in the image by analyzing the performance of a pixel-based classifier such as QDA, where no spatial information is exploited.

In addition, depending on whether our application requirements are maximizing speed or minimizing cost, different strategies can be taken. For instance, **to reduce cost** we can evaluate the discrimination capacity of the VNIR range with respect to the SWIR range. In some cases, the additional spatial information may compensate for a lower resolving power in the spectral domain. This would reduce the camera equipment cost. Similarly, by assessing if a Mosaic snapshot system can fulfill the application requirements, the cost can be reduced with respect to a high resolution Snapscan system. Moreover, more advanced processing methods may enable a VNIR system to perform equally well with a more economical illumination system (such as halogen with respect to LEDs), but at the expense of a higher computational cost.

It is important to note that when we increase the discrimination power of our system due to a suitable choice of a system parameter such as the camera hardware or the illumination, this can have a beneficial impact, not only on a classification accuracy task but on other hyperspectral imaging tasks such as anomaly detection or quantitative analysis of chemical/physical properties. In this respect, an increased discrimination power can be reflected for instance as higher fidelity spectra or lower intra-class variation.

To increase the system's speed several strategies can be adopted as well. We can move from a Snapscan system to a Snapshot camera system, where both acquisition and processing speeds will be increased thanks to the lower amount of acquired data per frame. An alternative to this is to perform spatial and spectral binning of the image, as well as relevant band selection. These methods can heavily reduce the amount of data generated and reduce its processing time. An increase in the illumination intensity can also help to reduce the integration time and therefore speed up acquisition. Finally, the choice of less time consuming/optimized processing methods, avoiding multi-frame acquisition or HDR also help to reduce the acquisition and processing times.

Future work

A system-wide study has been addressed in this thesis evaluating the impact of multiple key parameters. However, it was not possible to cover all system aspects and possible options in terms of system illumination, camera hardware and analysis and processing methods in one thesis. Several system elements can be further explored.

The tunable LED illumination setups could be further optimized and tested. There are also processing methods to increase the SNR that are worth investigating such as specific camera parameters, or super-resolution methods to increase the spatial resolution of Snapshot cameras. Moreover, new developments in the hardware for the SWIR range may also bring new tradeoffs. Next to this, it could be interesting to develop a more quantitative method to assess the spatial and spectral information available in the image, relating this to the actual physical resolution. This could guide the choice of the system parameters. One way to do this might be by comparing the classification accuracy obtained by relying purely on spectral or purely on spatial information. This could be done for instance by comparing the performance of a CNN on a 1x1 blocksize, exclusively relying on the spectral information per pixel with the performance of a CNN with a larger input blocksize applied to the corresponding RGB image. The difference between both model accuracies could give an indication of which type of information, spectral or spatial, is more important for a specific application case.

It could also be interesting to quantify and compare the computational and memory cost of the different analysis and pre/post-processing methods. This would allow to judge which methods are suitable for use at high processing speeds and at which cost.

Finally, all work presented in this thesis built on the assumption that data training and testing of the classifier models is done for each specific hyperspectral system (e.g., Snapscan camera with halogen lights). In other words, training and testing of the algorithms has to be repeated for every setup and no transfer model between hyperspectral systems has been used. Ideally, we would like to have robust classification models that are transferable, valid, and equally performant, across different hyperspectral systems with differences in illumination setup or camera system. This would further enable industry to implement multiple camera systems, while only training the classifier model once.

While the extensive research on how to perform calibration transfer between master and slave point spectroscopy instruments has recently been extended to hyperspectral devices (Pu et al., 2018), (Rehman et al., 2020), (Li et al., 2020), a different approach could be investigated. The manufacturing process of the hyperspectral filters on the sensors can introduce deviations from the original design, such as variations in the wavelength dependent sensitivity (QE). However, since all hyperspectral sensors are calibrated and their respective spectral responses known, this information could potentially be used to reduce the need for this model calibration transfer by bridging the gap between both systems based on the known spectral responses on calibration material such as Macbeth charts. Therefore, it may be possible to devise a method that would automatically calibrate a slave camera with respect to the master camera with minimal requirements for additional measurements for a specific target application.

For calibration transfers between setups of different characteristics such as lens, illumination system, camera position or even different sensor type (corresponding to different spatial-spectral resolution) a different transfer model may be required, because the above-mentioned method may not be able to cope with these additional setup modifications.

In this thesis, we have used CNNs to perform the ingredient discrimination/classification at pixel level. However, to estimate each ingredient specific abundance a second spatial post-processing step, as shown in Chapter 3, was required. In this respect, it could be interesting to investigate the possibility to estimate the ingredient abundance in one single step with the convolutional neural network. To do so, a high number of images should be provided to the network with its corresponding ingredient abundance. This would allow the network to not only discriminate the different ingredients, but also to quantify them simultaneously. For classification purposes we used small image blocks (7x7) that would contain generally one single seed or a portion of it. To extend the goal to quantification, the

training could be done with full hyperspectral images or at least portions of it where several seeds are present and more global ingredient features can be learned by the network.

References

- Abdlaty, R., Orepoulos, J., Sinclair, P., Berman, R. & Fang, Q. (2018). "High Throughput AOTF Hyperspectral Imager for Randomly Polarized Light". *Photonics Journal*, 2018, 5(1), 3; <https://doi.org/10.3390/photonics5010003>
- Ahlberg, J., Renhorn, I. G., Chevalier, T. R., Rydell, J., & Bergström, D. (2017). "Three-dimensional hyperspectral imaging technique". In *Algorithms and Technologies for Multispectral, Hyperspectral, and Ultraspectral Imagery XXIII* (Vol. 10198, p. 1019805). International Society for Optics and Photonics, May 2017.
- Al-Sarayreh, M., Reis, M., Yan, W.Q. & Klette, R. (2018). "Detection of Red-Meat Adulteration by Deep Spectral-Spatial Features in Hyperspectral Images". *Journal of Imaging*, 4(5), 63.
- Amigo, J.M., Martin, I. & Gowen, A. (2013) "Hyperspectral Imaging and Chemometrics: A Perfect Combination for the Analysis of Food Structure, Composition and Quality". *Data handling in science and technology* (Vol. 28, pp. 343-370). Elsevier.
- Amini, S., Homayouni, S., Safari, A., & Darvishsefat, A. A. (2018). "Object-based classification of hyperspectral data using Random Forest algorithm". *Geo-spatial information science*, 21(2), 127-138.
- Anand, R., Veni, S., Geetha, P., & Subramoniam, S. R. (2021). "Extended morphological profiles analysis of airborne hyperspectral image classification using machine learning algorithms". *International Journal of Intelligent Networks*, 2, 1-6.
- Bain, M. (2018) "Only black is the new black: a cultural history of fashion's favorite shade", Retrieved from <https://qz.com/quartz/1194798/only-black-is-the-new-black-a-cultural-history-of-fashion-favorite-shade/>
- "Bakery products market- growth, trends and forecast (2019-2024)". Retrieved from: <https://www.mordorintelligence.com/industry-reports/bakery-products-market>
- Bareth, G., Aasen, H., Bendig, J., Gnyp, M. L., Bolten, A., Jung, A., Michels, R. & Soukkamäki, J. (2014, April). "Spectral comparison of low-weight and UAV-based hyperspectral frame cameras with portable spectroradiometer measurements". *Proceedings of the Workshop on UAV-based Remote Sensing Methods for Monitoring Vegetation* (Vol. 94, pp. 1-6). Geographisches Institut der Universität zu Köln-Kölner Geographische Arbeiten.
- Barnes, R. J., Dhanoa, M. S., & Lister, S. J. (1989). "Standard normal variate transformation and detrending of near-infrared diffuse reflectance spectra". *Applied spectroscopy*, 43(5), 772-777.
- Behmann, J., Acebron, K., Emin, D., Bennertz, S., Matsubara, S., Thomas, S., Bohnenkamp, D., Kuska, M.T., Jussila, J., Salo, H., Mahlein, A.K. & Rascher, U. (2018). "Specim IQ: Evaluation of a New, Miniaturized Handheld Hyperspectral Camera and Its Application for Plant Phenotyping and Disease Detection". *Sensors* 2018, 18(2), 441; <https://doi.org/10.3390/s18020441>
- Benediktsson, J. A., Palmason, J. A., & Sveinsson, J. R. (2005). "Classification of hyperspectral data from urban areas based on extended morphological profiles". *IEEE Transactions on Geoscience and Remote Sensing*, 43(3), 480-491.

- Bioucas-Dias, J. M., Plaza, A., Camps-Valls, G., Scheunders, P., Nasrabadi, N., & Chaussoot, J. (2013). "Hyperspectral remote sensing data analysis and future challenges". *IEEE Geoscience and remote sensing magazine*, 1(2), 6-36.
- Blanch-Perez-del-Notario, C., Baert, R., & D'Hondt, M. (2012). "Multi-objective genetic algorithm for task assignment on heterogeneous nodes". *International Journal of Digital Multimedia Broadcasting*, 2012.
- Blanch-Perez-del-Notario, C., & Lambrechts, A. (2016) "Hyperspectral imaging for textile sorting and recycling in industry". In *Hyperspectral Imaging & Applications Conference* (pp. 12-13).
- Blanch-Perez-del-Notario, C., & Lambrechts, A. (2017). "Hyperspectral analysis for extraction of chemical characteristics in dehydrated bones". *Journal of Spectral Imaging*, 6. 2017.
- Blanch-Perez-del-Notario, C., Saeys, W., & Lambrechts, A. (2019). "Convolutional neural networks for heterogeneous ingredient discrimination with hyperspectral imaging". In *2019 10th Workshop on Hyperspectral Imaging and Signal Processing: Evolution in Remote Sensing (WHISPERS)* (pp. 1-6). IEEE.
- Blanch, C., Saeys, W. & Lambrechts, A. (2020). "Fast ingredient quantification in multigrain flour mixes using hyperspectral imaging". *Journal of Food Control*, vol. 118, 2020. <https://doi.org/10.1016/j.foodcont.2020.107366>
- Boelt, B., Shrestha, S., Salimi, Z., Jorgensen, J.R., Nicolaisen, M & Carstensen, J.M. (2018). "Multispectral imaging – a new tool in seed quality assessment?". *Seed Science Research*, Vol 28, Special Issue 3 (Seeds as Systems).
- Bonah, E., Huang, X., Yi, R., Aheto, J. H., & Yu, S. (2020). "Vis-NIR hyperspectral imaging for the classification of bacterial foodborne pathogens based on pixel-wise analysis and a novel CARS-PSO-SVM model". *Infrared Physics & Technology*, 105, 103220.
- Bonifazi, G., Capobianco, G., Palmieri, R. and Serranti, S. (2019). "Hyperspectral imaging applied to the waste recycling sector". *Spectroscopy Europe*, April 2019.
- Brosnan, T., Sun, D-W. (2004) "Improving quality inspection of food products by computer vision – a review". *Journal of Food Engineering*, vol 61, 3-16.
- Camps-Valls, G., & Bruzzone, L. "Kernel-based methods for hyperspectral image classification". *IEEE Trans. Geosci. Remote Sens.* 43(6), 1351–1362 (2005)
- Caporaso, N., Whitworth, Martin B., & Fisk, Ian.D. (2018). "Near-Infrared spectroscopy and hyperspectral imaging for non-destructive quality assessment of cereal grains". *Applied Spectroscopy Reviews* 2018, DOI: 10.1080/05704928.2018.1425214
- Carstensen, J.M "LED spectral imaging with food and agricultural applications". *Proceedings of SPIE, the International Society for Optical Engineering*, Vol. 10656, 2018.
- Castorena, J., & Oyen, D. (2020, March). "Learning Shapes on Image Sampled Points with Dynamic Graph CNNs". In *2020 IEEE Southwest Symposium on Image Analysis and Interpretation (SSIAI)* (pp. 1-4). IEEE.
- Chang, C. I., & Chiang, S. S. (2002). "Anomaly detection and classification for hyperspectral imagery". *IEEE transactions on geoscience and remote sensing*, 40(6), 1314-1325.

- Chen., Y. Nasrabadi, N.M. & Tran, T.D. "Hyperspectral image classification via kernel sparse representation". *IEEE Trans. Geosci. Remote Sens.* 51(1), 217–231 (2013)
- Chen, Y., Jiang, H., Li, Ch., Jia, X. & Ghamisi, P. (2016) "Deep Feature Extraction and Classification of Hyperspectral Images Based on Convolutional Neural Networks", *IEEE Transactions on Geoscience and Remote Sensing*, October 2016.
- Chen, H., Ho, B., Wang, H., Tan, S. H., Zhao, C. X., Nguyen, N. T., ... & Zhou, J. (2019, September). "Automatic Live and Dead Cell Classification via Hyperspectral Imaging". In *2019 10th Workshop on Hyperspectral Imaging and Signal Processing: Evolution in Remote Sensing (WHISPERS)* (pp. 1-5). IEEE.
- Chen, H., Tan, C., & Lin, Z. (2020). "Quantitative Determination of the Fiber Components in Textiles by Near-Infrared Spectroscopy and Extreme Learning Machine". *Analytical Letters*, 53(6), 844-857.
- Chen, Y., Jiang, H., Li, Ch., Jia, X. & Ghamisi, P. (2016) "Deep Feature Extraction and Classification of Hyperspectral Images Based on Convolutional Neural Networks". *IEEE Transactions on Geoscience and Remote Sensing*, October 2016.
- Choudhary, R., Mahesh, S., Paliwal, J. & Jayas, D.S. (2009). "Identification of wheat classes using wavelet features from near infrared hyperspectral images of bulk samples". *Biosystems Engineering* 102, www.elsevier.com/locate/issn/15375110
- "CIE 1931 Color Space", 2021. Retrieved from https://en.wikipedia.org/wiki/CIE_1931_color_space
- "CIE LAB color space", 2021. Retrieved from https://en.wikipedia.org/wiki/Lab_color_space
- "CIE Standard Observers and calculation of CIE X, Y, Z color values", Hunter Lab, 2012. Retrieved from <https://support.hunterlab.com/hc/en-us/articles/203420099-CIE-Standard-Observers-and-calculation-of-CIE-X-Y-Z-color-values-AN-1002b>
- Comaniciu, D. & Meer, P. (2002) "Mean shift: a robust approach toward feature space analysis", *IEEE Transactions on Pattern Analysis and Machine Intelligence*, vol. 24, no. 5, pp. 603-619, 2002.
- Côme, E., Oukhellou, L., Denœux, T., & Aknin, P. (2008). "Mixture model estimation with soft labels. In *Soft Methods for Handling Variability and Imprecision*" (pp. 165-174). Springer, Berlin, Heidelberg.
- CVR lighting, Ltd 2015. <http://cvrlighting.com/>
- Cyrus. D. Cantrell (2000). "Modern Mathematical Methods for Physicists and Engineers". Cambridge University Press. ISBN 0-521-59827-3.
- "D65 illuminant", CIE. (n.d.). CIE Spectral Data. Retrieved from <http://files.cie.co.at/204.xls>
- Davidson, M. W. (2015). "Tungsten-halogen incandescent lamps". *Carl Zeiss Microscopy Online*. <http://zeiss-campus.magnet.fsu.edu/articles/lightsources/tungstenhalogen.html>.
- Deng, F., Pu, S., Chen, X., Shi, Y., Yuan, T. & Pu, S. "Hyperspectral Image Classification with Capsule Network Using Limited Training Samples", in *Sensors* 2018.
- Dong P., Liu J. (2011) "Hyperspectral Image Classification Using Support Vector Machines with an Efficient Principal Component Analysis Scheme". In: Wang Y., Li T. (eds) *Foundations of Intelligent Systems. Advances in Intelligent and Soft Computing*, vol 122. Springer, Berlin, Heidelberg. https://doi.org/10.1007/978-3-642-25664-6_17

Drăguț, L., Csillik, O., Eisank, C., & Tiede, D. (2014). "Automated parameterisation for multi-scale image segmentation on multiple layers". *ISPRS Journal of photogrammetry and Remote Sensing*, 88, 119-127.

"Effi-flex adjustable beam angle LED bar", (Dec 21, 2020) Retrieved from https://www.effilux.com/documentation/doc-technique/DATASHEET_EFFI-FLEX_V2.4.2020.pdf

Elmasry, G., Kamruzzaman, M., Sun, D-W. & Allen, P. (2012). "Principles and Applications of Hyperspectral Imaging in Quality Evaluation of Agro-Food Products: A Review" *Critical reviews in food science and nutrition*. 2012. 52. 999-1023. 10.1080/10408398.2010.543495.

"Étude de Caractérisation des TLC (Textiles D'habillement, Linge de Maison et Chaussures) Usagés Entrant en Centres de Tri ainsi que des Déchets Ultimes Résultant du Tri" (2014).

"Euclidean Distance", 2021. Retrieved from https://en.wikipedia.org/wiki/Euclidean_distance

Fabricius, H., & Pust, O. (2014) "Linear Variable Filters for Biomedical and Hyperspectral Imaging Applications". In *Biomedical Optics* (pp. BS3A-42). Optical Society of America, April 2014. DOI: 10.1364/BIOMED.2014.BS3A.42.

Farooq, A., Jia, X., Hu, J., & Zhou, J. (2019, September). "Knowledge Transfer via Convolution Neural Networks for Multi-Resolution Lawn Weed Classification". In 2019 10th Workshop on Hyperspectral Imaging and Signal Processing: Evolution in Remote Sensing (WHISPERS) (pp. 01-05). IEEE.

Feng, Y. Z., & Sun, D. W. (2012). "Application of hyperspectral imaging in food safety inspection and control: a review". *Critical reviews in food science and nutrition*, 52(11), 1039-1058.

Feng, F., Li, W., Du, Q., & Zhang, B. (2017). "Dimensionality reduction of hyperspectral image with graph-based discriminant analysis considering spectral similarity". *Remote sensing*, 9(4), 323.

Feng, L., Zhu, S., Liu, F., He, Y., Bao, Y. & Zhang, C. (2019). "Hyperspectral imaging for seed quality and safety inspection: a review". *Plant Methods* (2019) 15:91 <https://doi.org/10.1186/s13007-019-0476-Y>

Fernandez-Pierna, J. A., Vincke, D., Dardenne, P., Yang, Z., Han, L., & Baeten, V. (2014). "Line scan hyperspectral imaging spectroscopy for the early detection of melamine and cyanuric acid in feed". *Journal of Near Infrared Spectroscopy*, 22(2), 103-112.

Fernandez-Pierna, J. A., Vermeulen, P., Eylenbosch, D., Burger, J., Bodson, B., Dardenne, P., & Baeten, V. (2020). "Chemometrics in NIR Hyperspectral Imaging: Theory and Applications in the Agricultural Crops and Products Sector". *Comprehensive Chemometrics Chemical and Biochemical Data Analysis*, 361-379.

Fibersort, Valvan Baling systems. Retrieved from <http://www.valvan.com/products/equipment-for-used-clothing-wipers/sorting-equipment/fibersort/>

Flémal, P., Pigeon, O., Dardenne, P., Pierna, J. F., Baeten, V., & Vermeulen, P. (2017). "Assessment of pesticide coating on cereal seeds by near infrared hyperspectral imaging". *Journal of Spectral Imaging*, 6.

Folkestad, A., Wold, J.P., Rørvik, K-A., Tschudi, J. Haugholt, K.H., Kolstad, K. and Mørkøre, T. (2008) "Rapid and non-invasive measurements of fat and pigment concentrations in live and slaughtered Atlantic salmon (*Salmo salar* L.)", in Elsevier *Journal of Aquaculture*, Volume 280, Issues 1-4, 2008, Pages 129-135, ISSN 0044-8486, <https://doi.org/10.1016/j.aquaculture.2008.04.037>.

- "Fourth Industrial Revolution", 2020. https://en.wikipedia.org/wiki/Fourth_Industrial_Revolution
- Fotiadou, K., Tsagkatakis, G., & Tsakalides, P. (2017). "Deep convolutional neural networks for the classification of snapshot mosaic hyperspectral imagery". *Electronic Imaging*, 2017(17), 185-190.
- Fuller, D., Colledge, S., Murphy, C. & Stevens, C.J. (2017). "Sizing up cereal variation: patterns in grain evolution revealed in chronological and geographical comparison".
- Geelen, B., Tack, K. & Lambrechts, A. (2013) "A Snapshot Multispectral Imager with Integrated, Tiled Filters and Optical Duplication", in *Proceedings of SPIE*, 8613:14, March 2013. DOI: 10.1117/12.2004072
- Geelen, B., Blanch, C., Gonzalez, P., Tack, N., & Lambrechts, A. (2015). "A tiny VIS-NIR snapshot multispectral camera". In *Advanced Fabrication Technologies for Micro/Nano Optics and Photonics VIII* (Vol. 9374, p. 937414). International Society for Optics and Photonics, March 2015.
- Gewali, U. B., Monteiro, S. T., & Saber, E. (2018). "Machine learning based hyperspectral image analysis: a survey", 2019. arXiv preprint arXiv:1802.08701.
- Ghuneim, A. http://www.imageprocessingplace.com/downloads_V3/root_downloads/tutorials/contour_tracing_Abeer_George_Ghuneim/connect.html
- Giacco, R., Clemente, G., Cipriano, D., Luongo, D., Viscovo, D., Patti, L., Di Marino, L., Giacco, A., Naviglio, D., Bianchi MA., Ciati, R., Brighenti, F., Rivellese, A.A. & Riccardi, G. (2010). "Effects of the regular consumption of wholemeal wheat foods on cardiovascular risk factors in healthy people". *Nutr Metab Cardiovasc Dis* 2010; 20:186-94.
- GNU Image Manipulation Program, The GIMP team, GIMP 2.0, 1997-2020, retrieved on 31.07.2014. <http://gimp.org>.
- Goeltner, C. (2020). "LED light source enables mobile spectroscopy for industry and consumer use", in *Laser Focus World* magazine, March 2020. <https://www.laserfocusworld.com/lasersources/article/14168107/led-light-source-enables-mobile-spectroscopy-for-industry-and-consumer-use>
- Goetz, A. F. (2011). "Measuring the Earth from Above: 30 Years (and Counting) of Hyperspectral Imaging". *Photonics Spectra*, 45(6), 42-47.
- Gonzalez, P., Geelen, B., Blanch, C., Tack, K., & Lambrechts, A. (2015). "A CMOS-compatible, monolithically integrated snapshot-mosaic multispectral imager". *NIR news*, 26(4), 6-11.
- Gonzalez, P., Tack, K., Geelen, B., Masschelein, B., Charle, W., Vereecke, B. & Lambrechts, A. (2016, May) "A novel CMOS-compatible, monolithically integrated line-scan hyperspectral imager covering the VIS-NIR range". In *Next-Generation Spectroscopic Technologies IX* (Vol. 9855, p. 98550N). International Society for Optics and Photonics. Proc. SPIE 9855, 98550N (2016). <https://doi.org/10.1117/12.2230726>
- Gonzalez, P., Pichette, J., Vereecke, B., Masschelein, B., Krasovitski, L., Bikov, L., & Lambrechts, A. (2018, May). "An extremely compact and high-speed line-scan hyperspectral imager covering the SWIR range". In *Image Sensing Technologies: Materials, Devices, Systems, and Applications V* (Vol. 10656, p. 106560L). International Society for Optics and Photonics. <https://doi.org/10.1117/12.2304918>
- Gonzalez, R.C & Woods, R.E "Digital Image Processing", Eaglewood Cliffs, NJ: Prentice-Hall, 2002.

Goodman, T.A (2012) "Colour Design, Theories and Applications". International Standards for Colour, Pages 417-452

Goossens, T., Van De Vijver, R., Mertens, K., Saeys, W., Lootens, P., Somers, B., ... & Van Hoof, C. (2018). "System characterization of a snapshot mosaic spectral camera for UAV applications in agriculture". In Hyperspectral Imaging & Applications Conference, October 2018.

Gunasekaran, S. (1996). "Computer vision technology for food quality assurance". Trends in Food Science and Technology, 7(8), 245–256. 1996

Guo, Y., Yin, X., Zhao, X., Yang, D., & Bai, Y. (2019). "Hyperspectral image classification with SVM and guided filter". EURASIP Journal on Wireless Communications and Networking, 2019(1), 1-9. <https://doi.org/10.1186/s13638-019-1346-z>

Gutiérrez-Gutiérrez, J.A, Pardo, A., Real, E., López-Higuera, J.M. & Conde, O.M. (2019) "Custom Scanning Hyperspectral Imaging System for Biomedical Applications: Modeling, Benchmarking, and Specifications". Sensors Journal, April 2019, 1692; doi:10.3390/s19071692.

Hagen, N. A., & Kudenov, M. W. (2013). "Review of snapshot spectral imaging technologies". Optical Engineering, 52(9), 090901.

Hahn, R., Haist, T., Hämmerling, F. E., Fleischle, D., Schwanke, O., Hauler, O., Rebner, K., Brecht, M. & Osten, W. (2020, April). "Detailed characterization of a hyperspectral snapshot imager for full-field chromatic confocal microscopy". In Optics and Photonics for Advanced Dimensional Metrology (Vol. 11352, p. 113520Y). International Society for Optics and Photonics. <https://doi.org/10.1117/12.2556797>.

Hai, V., Tachtatzis, C., Murray, P., Harle, D., Dao, T.K., Atkinson, R., Le, T-L., Andonovic, A. & Marshall, S. (2016). "Spatial and spectral features utilization on a Hyperspectral imaging system for rice seed varietal purity inspection". 2016 IEEE RIVF International Conference on Computing & Communication Technologies, Research, Innovation, and Vision for the Future.

Han, J., Kamber, M. & Pei, J. (2012) "Data mining: concepts and techniques" <https://doi.org/10.1016/C2009-0-61819-5>

Haran, T. "Short-Wave Infrared Diffuse Reflectance of Textile Materials". Thesis, 2008.

He, C., Zhu, Q., Huang, M. & Mendoza, F. (2016) "Model updating of hyperspectral imaging data for variety discrimination of maize seeds harvested in different years by clustering algorithm." Transactions of the ASABE. 59(6): 1529-1537, 2016.

He, D., Pang, Y., Lodewijks, G. & Liu, X. (2018) "Healthy speed control of belt conveyors on conveying bulk materials", in Elsevier Journal of Powder Technology, Volume 327, March 2018, Pages 408-419. <https://doi.org/10.1016/j.powtec.2018.01.002>

Helland, I. S., Næs, T., & Isaksson, T. (1995). "Related versions of the multiplicative scatter correction method for preprocessing spectroscopic data". Chemometrics and Intelligent Laboratory Systems, 29(2), 233-241.

Herrala, E. (2020), "Guide to selecting hyperspectral instruments", Specim, Spectral Imaging Ltd Retrieved from <https://www.specim.fi/>

Herrero-Langreo, A., Gorretta, N., Beghin, A., Ferone, M., Gowen, A., & Scannell, A. (2019, September). "Orthogonal Projection as a Spectral Pre-Treatment Method To Reduce The Interference Of

- Polystyrene Signal In Nir Imaging Of Agar On Petri-Dishes.” In 2019 10th Workshop on Hyperspectral Imaging and Signal Processing: Evolution in Remote Sensing (WHISPERS) (pp. 1-4). IEEE.
- Holland, J.H. (1992) “Genetic Algorithms”. In Scientific American, 267. <http://dx.doi.org/10.1038/scientificamerican0792-66>
- “HSI Range LED Lighting”, (2020) <https://www.afilux.com/>
- Hsu, C-W., Chang, Ch-Ch. & Lin, Ch-J. (2016) “A practical guide to support vector classification”, available at <https://www.csie.ntu.edu.tw/~cjlin/papers/guide/guide.pdf>
- Hu, L., Qi, C., & Wang, Q. (2018). “Spectral-spatial hyperspectral image classification based on mathematical morphology post-processing”. *Procedia Computer Science*, 129, 93-97.
- Huang. H., Liu, L. & Ngadi, M. (2014). “Recent Developments in Hyperspectral Imaging for Assessment of Food Quality and Safety”. *Journal of Sensors*, April 2014.
- Huang, M., He, C., Zhu, Q., & Qin, J. (2016). “Maize seed variety classification using the integration of spectral and image features combined with feature transformation based on hyperspectral imaging”. *Applied Sciences*, 6(6), 183.
- Hubold, M., Berlich, R., Gassner, C., Brüning, R., & Brunner, R. (2018, February). “Ultra-compact micro-optical system for multispectral imaging”. In *MOEMS and Miniaturized Systems XVII* (Vol. 10545, p. 105450V). International Society for Optics and Photonics.
- Hunter Lab, “CIE observer angle”. <https://support.hunterlab.com/hc/en-us/articles/203420099-CIE-Standard-Observers-and-calculation-of-CIE-X-Y-Z-color-values-AN-1002b>
- “Hyperspectral and Multispectral imaging”, Edmund Optics GmbH, 2021. <https://www.edmundoptics.es/knowledge-center/application-notes/imaging/hyperspectral-and-multispectral-imaging/>
- “Hyperspectral imaging market – growth, trends, and forecast (2019-2024)” (2018). Mordor Intelligence Report; Retrieved from <https://www.mordorintelligence.com/industry-reports/hyperspectral-imaging-market>
- “Hyperspectral Imaging Market – growth, trends, covid-19 impact, and forecasts (2021-2026)”. Mordor Intelligence Report; Retrieved from <https://www.mordorintelligence.com/industry-reports/hyperspectral-imaging-market>
- “Hyperspectral imaging market 2018: Key insights, Industry global revenue, historic & forecast period 2018-2024”. (September 2018). Retrieved from <https://www.marketwatch.com/press-release/hyperspectral-imaging-market-2018-key-insights-industry-global-revenue-historical-forecast-period-2018-2024-2018-09-18>
- “Hyperspectral Imaging”. (2021, January 11). Retrieved from Wikipedia https://en.wikipedia.org/wiki/Hyperspectral_imaging
- International Color Consortium 1999, sRGB Doc, IEC 61966-2-1:1999. Retrieved from <http://www.color.org/chardata/rgb/srgb.xalter>
- Kakani, V., Nguyen, V. H., Kumar, B. P., Kim, H., & Pasupuleti, V. R. (2020). “A critical review on computer vision and artificial intelligence in food industry”. *Journal of Agriculture and Food Research*, 2 (February), 100033. <https://doi.org/10.1016/j.jafr.2020.100033>

- Kale, K. V., Solankar, M. M., Nalawade, D. B., Dhumal, R. K., & Gite, H. R. (2017). "A research review on hyperspectral data processing and analysis algorithms". *Proceedings of the National Academy of Sciences, India Section A: Physical Sciences*, 87(4), 541-555.
- Kamruzzaman M., El Masry G., Sun D-W. & Allen P. (2012) "Non-destructive prediction and visualization of chemical composition in lamb meat using NIR hyperspectral imaging and multivariate regression". *Innovative Food Science and Emerging Technologies* vol 16 (2012), pp 218-226.
- Kang, X., Li, Z. & Benediktsson, J-A. (2013). "Spectral-spatial hyperspectral image classification with edge-preserving filtering". *IEEE Transactions on Geoscience and remote sensing*.
- Katrašnik, J., Pernuš, F., & Likar, B. (2013). "A method for characterizing illumination systems for hyperspectral imaging". *Optics express*, 21(4), 4841-4853.
- Kerekes, J.P & Baum, J.E. "Hyperspectral Imaging System Modelling" in *Lincoln Laboratory Journal* Vol 14, 2003.
- Keresztes, J.C., Koshel, R.J., D'huys, K., De Ketelaere, B., Audenaert, J., Goos, P. & Saeys, W. (2016). "Augmented design and analysis of computer experiments: a novel tolerance embedded global optimization approach applied to SWIR hyperspectral illumination design". *Optics Express*, 24 (26), 29380-29405
- Khan, M. J., Khan, H.S, Yousaf, A., Khurshid, K. & Abbas, A. (2018). "Modern trends in hyperspectral image analysis: a review". *IEEE Access Open Access Journal*, Digital Object Identifier 10.1109/ACCESS.2018.2812999, March 2018.
- Kim, C. H., Liang, H. W., Han, S. H., Kim, J. Y., Ryang, K. W., & Kim, C. (2016). "Optimizing spectral distribution character of the LEDs to decrease discoloring of the collections in museum". *arXiv preprint arXiv:1604.06389*.
- Kim, S. J., Deng, F., & Brown, M. S. (2011). "Visual enhancement of old documents with hyperspectral imaging". *Pattern Recognition*, 44(7), 1461-1469.
- Kobayashi, T., Nagata, H., Goto, Y., Toyoda, H. & Tallada, J. (2006). "Study on Anthocyanin Pigment Distribution Estimation for Fresh Fruits and Vegetables Using Hyperspectral Imaging. Part 2. Visualization of Anthocyanin Pigment Distribution of Strawberry (*Fragaria x ananassa* Duchesne)" in *Shokubutsu Kankyo Kogaku*, 2006.
- Kong, W., Zhang, C., Liu, F., Nie, P. & He, Y. (2013). "Rice seed cultivar identification using near-infrared hyperspectral imaging and multivariate data analysis". *Sensors* 2013, ISSN 1424-8220 www.mdpi.com/journal/sensors
- Kruse, F. A., Lefkoff, A. B., Boardman, J. W., Heidebrecht, K. B., Shapiro, A. T., Barloon, P. J., & Goetz, A. F. H. (1993). "The spectral image processing system (SIPS)—interactive visualization and analysis of imaging spectrometer data". *Remote sensing of environment*, 44(2-3), 145-163.
- Kurtulmus, F., Alibas, I. & Kavdir, I. (2015). "Classification of pepper seeds using machine vision based on neural network". *International Journal on Agriculture & Biology Engineering*, 2015.
- Lambrechts, A., Gonzalez, P., Geelen, B., Soussan, P., Tack, K., & Jayapala, M. (2014). "A CMOS-compatible, integrated approach to hyper-and multispectral imaging". In *2014 IEEE International Electron Devices Meeting* (pp. 10-5), 2014.

- Lanaras, C. (2018). "Enhancing the Spectral and Spatial Resolution of Remote Sensing Images" (Vol. 122). ETH Zurich.
- Lapray, P.-J., Wang, X., Thomas, J.B. & Gouton, P. (2014) "Multispectral Filter Arrays: Recent Advances and Practical Implementation", in *Sensors* 2014, 14, 21626-21659; doi:10.3390/s141121626
- Lawrence, K. C., Park, B., Windham, G. H. W., & Thai, C. N. (2007). "Evaluation of LED and tungsten-halogen lighting for fecal contaminant detection". *Applied engineering in agriculture*, 23(6), 811-818.
- Li, H., Liu, W., Dong, B., Kaluzny, J. V., Fawzi, A. A., & Zhang, H. F. (2017). "Snapshot hyperspectral retinal imaging using compact spectral resolving detector array". *Journal of Biophotonics*, 10(6-7), 830-839. 2017.
- Li, N., Huang, X., Zhao, H., Qiu, X., Deng, K., Jia, G., Li, Z., Fairbairn, D. & Gong, X. (2019) "A Combined Quantitative Evaluation Model for the Capability of Hyperspectral Imagery for Mineral Mapping". *Sensors*, January 2019.
- Li, X. Y., Ren, G. X., Fan, P. P., Liu, Y., Sun, Z. L., Hou, G. L., & Lv, M. R. (2020). "Study on the Calibration Transfer of Soil Nutrient Concentration from the Hyperspectral Camera to the Normal Spectrometer". *Hindawi Journal of Spectroscopy*, 2020.
- Liao, W., Vancoillie, F., Devriendt, F., Gautama, S., Pizurica, A., & Philips, W. (2014). "Fusion of pixel-based and object-based features for classification of urban hyperspectral remote sensing data". In 5th International conference on Geographic Object-Based Image Analysis (GEOBIA 2014) (Vol. 3, No. 2S, pp. 179-184).
- Liao, W., Ochoa-Donoso, D.E., Van Coillie, F., Li, J., Qi, Ch., Gautama, S. & Philips, W. "Spectral-spatial classification for hyperspectral image by bilateral filtering and morphological features", 8th Workshop on Hyperspectral Image and Signal Processing: Evolution in Remote Sensing (WHISPERS), 2016.
- Lorente, D., Aleixos, N., Gomez-Sanchis, J., Cubero, S., Garcia-Navarrete, O.L. & Blasco, J. (2011). "Recent Advances and Applications of Hyperspectral Imaging for Fruit and Vegetable Quality Assessment". *Food and Bioprocess Technology* · May 2011
- Lu, Y., Saeys, W., Kim, M., Peng, Y., & Lu, R. (2020). "Hyperspectral imaging technology for quality and safety evaluation of horticultural products: A review and celebration of the past 20-year progress". *Postharvest Biology and Technology* vol 170, 111318, Dec 2020. <https://doi.org/10.1016/j.postharvbio.2020.111318>
- Luthman, A. S., Waterhouse, D. J., Ansel-Bollepalli, L., Yoon, J., Gordon, G. S., Joseph, J., ... & Bohndiek, S. E. (2018). "Bimodal reflectance and fluorescence multispectral endoscopy based on spectrally resolving detector arrays". *Journal of Biomedical Optics*, 24(3), 031009.
- Ma, F., Wang, J., Liu, Ch., Lu, X., Chen, C., Yan, J. & Zheng, L. (2015) "Discrimination of kernel quality characteristics for sunflower seeds based on multispectral imaging approach". *Food Analytical Methods* 8, 1629–1636.
- Mäkelä, M., Rissanen, M., & Sixta, H. (2020). "Machine vision estimates the polyester content in recyclable waste textiles". *Resources, Conservation and Recycling*, 161, 105007.
- Manley, M., Baeten, V. (2018). Chapter 3. "Spectroscopic technique: Near Infrared (NIR) Spectroscopy". <https://doi.org/10.1016/B978-0-12-814264-6.00003-7>

- Manley, M., McGoverin, C.M., Engelbrecht, P. & Geladi, P. (2011). "Influence of grain topography on near infrared hyperspectral images". *Talanta Elsevier*, 89- 223-230. www.elsevier.com/locate/talanta
- Mathison, G.W., Engstrom, D.F., Soofi-Siawash, R. & Gibb, D. (1997) "Effects of tempering and degree of processing of barley grain on the performance of bulls in the feedlot". *Canadian journal of animal science*, 1997.
- Matlab Release 2015b, The MathWorks, Inc., Natick, MA, USA 2015. <https://www.mathworks.com>
- Matteoli, S., Diani, M., & Corsini, G. (2010). "A tutorial overview of anomaly detection in hyperspectral images". *IEEE Aerospace and Electronic Systems Magazine*, 25(7), 5-28.
- Melgani, F. & Bruzzone, L. (2004). "Classification of hyperspectral remote sensing images with support vector machines". *IEEE Trans. Geosci. Remote Sens.* 42(8), 1778–1790 (2004)
- "Metamerism (color)", Feb 2021, Retrieved from [https://en.wikipedia.org/wiki/Metamerism_\(color\)](https://en.wikipedia.org/wiki/Metamerism_(color))
- Mills, A. (2005). "Phosphor development for LED lighting". *Advanced Semiconductor Magazine*, Vol. 18, n3, pp 32-34. April 2005.
- Mindermann, S. (2018). "Hyperspectral Imaging for Readability Enhancement of Historic Manuscripts" (Doctoral dissertation, Technical University of Munich).
- Mishra, P., & Hélie, S. (2020). "3D shape estimation in a constraint optimization neural network". *Vision Research*, 177, 118-129.
- Mishra, P., Herrero-Langreo, A., Barreiro, P., Roger, J-M., Diezma, B., Gorretta, N. & Lleo, L. (2015). "Hyperspectral to multispectral imaging for detection of tree nuts and peanut traces in wheat flour". *Journal of Spectral Imaging*, June 2015.
- Morgan, S.L., Nieuwland, A.A., Mubarak, C.R., Hendrix, J.E., Enlow, E.M. & Vasser, B.J. (2004). "Forensic discrimination of dyed textile fibers using UV-VIS and Fluorescence Microspectrophotometry". *Proceedings of the European Fibres Group, Prague (2004)*.
- Moroni, M., Mei, A., Leonardi, A., Lupo, E. & La Marca, F. (2015) "PET and PVC Separation with Hyperspectral Imagery", in *Sensors* 2015, 15, 2205-2227; doi:10.3390/s150102205.
- Naes, T., Isaksson, T., Fearn, T. & Davies, T. (2004). "A User-Friendly Guide to Multivariate Calibration and Classification". NIR Publications.
- Ngadi, M. O., & Liu, L. (2010). "Hyperspectral image processing techniques". In *Hyperspectral imaging for food quality analysis and control*. (pp. 99-127). Academic Press.
- Nguyen-Do-Trong, N., Keresztes, J.C., De Ketelaere, B. & Saeys, W. "Cross-polarised VNIR hyperspectral reflectance imaging system for agrifood products" in *Journal of Biosystems Engineering*, Volume 151, 2016, Pages 152-157, ISSN 1537-5110. <https://doi.org/10.1016/j.biosystemseng.2016.08.027>.
- Novini, A. (1995). "The latest in vision technology in today's food and beverage container manufacturing industry". *Food Processing Automation IV Proceedings of the 1995 Conference*. Michigan, USA: ASAE.
- Oehlschläger, J., Schmidhalter, U., & Noack, P. O. (2018, September). "UAV-based hyperspectral sensing for yield prediction in winter barley". In *2018 9th Workshop on Hyperspectral Image and Signal Processing: Evolution in Remote Sensing (WHISPERS)* (pp. 1-4). IEEE.

- Oliveri, P., Malegori, C., Casale, M., Tartacca, E., & Salvatori, G. (2019). "An innovative multivariate strategy for HSI-NIR images to automatically detect defects in green coffee". *Talanta*, 199, 270-276.
- Ortega, S., Guerra, R., Diaz, M., Fabelo, H., Lopez, S., Callico, G-M. & Sarmiento, R. (2019). "Hyperspectral Push-Broom Microscope Development and Characterization". In Special Section on Advanced optical imaging for extreme environments, September 2019. DOI 2019.2937729
- Pan, L., Sun, Y., Xiao, H., Gu, X., Hu, P., Wei, Y. & Kang, T. (2017). "Hyperspectral imaging with different illumination patterns for the hollowness classification of white radish". *Postharvest biology and technology*, vol 126, pp 40-49.
- Paoletti, M.E., Haut, J.M., Plaza, J. & Plaza, A. (2018) "A new deep convolutional neural network for fast hyperspectral image classification". *ISPRS Journal of Photogrammetry and Remote Sensing* 145 (2018).
- Paoletti, M.E., Haut, J.M., Plaza, J. & Plaza, A. (2019) "Deep learning classifiers for hyperspectral imaging: A review". *ISPRS Journal of Photogrammetry and Remote Sensing*, Volume 158, December 2019, Pages 279-317
- Park, B., Windham, W. R., Lawrence, K. C., & Smith, D. P. (2007). "Contaminant classification of poultry hyperspectral imagery using a spectral angle mapper algorithm". *Biosystems Engineering*, 96(3), 323-333. DOI: 10.1016/j.biosystemseng.2006.11.012 AGR: IND43886778
- Pasquini, C. (2018) "Near infrared spectroscopy: a mature analytical technique with new perspectives: a review". *Elsevier Journal of Analytical Chimica Acta* 1026, pp 8-36, 2018.
- Patel, K.K., Kar, A., Jha, S.N. & Khan, M.A. (2012). "Machine vision system: a tool for quality inspection of food and agricultural products". *Journal of Food Science and Technology*, 2012. <https://www.ncbi.nlm.nih.gov/pmc/articles/PMC3550871/>
- Pearson, T.C. (2013) "Accurate seed sorting with machine vision". <https://www.vision-systems.com/articles/2013/07/accurate-seed-sorting-with-machine-vision.html>
- PerClass BV 2008-2021, Delft, NL. <http://perclass.com/perclass-toolbox/product>
- Perona, P. & Malik, J. (1990). "Scale-space and edge detection using anisotropic diffusion", in *IEEE Transactions on Pattern Analysis and Machine Intelligence*, 12 (7): 629-639.
- Perot, A., & Fabry, C. (1899). "On the application of interference phenomena to the solution of various problems of spectroscopy and metrology", in *The Astrophysical Journal*, 9, 87.
- Peter, A .M "Design and Evaluation of LED Illumination Source for Multispectral Imaging Applications", Thesis for Master of Technology, 2015.
- Petropoulos, G. P., Vadrevu, K. P., & Kalaitzidis, C. (2013). "Spectral angle mapper and object-based classification combined with hyperspectral remote sensing imagery for obtaining land use/cover mapping in a Mediterranean region". *Geocarto international*, 28(2), 114-129. DOI: 10.1080/10106049.2012.668950
- Pichette, J., Charle, W., & Lambrechts, A. (2017) "Fast and compact internal scanning CMOS-based hyperspectral camera: the Snapscan" In *Photonic Instrumentation Engineering IV* (Vol. 10110, p. 1011014). International Society for Optics and Photonics.

- “PixelCam, OEM Multispectral Imaging Camera”. Retrieved from <https://www.acalbfi.com/uk/Imaging-for-Science-and-Industry/Hyperspectral-Imager/p/OEM-Multispectral-Imaging-Camera/0000003FJW>. <https://www.pixelteq.com>
- Plaza, A., Du, Q., Chang, Y-L. & King, R-L. (2011). “High Performance Computing for Hyperspectral Remote Sensing” in IEEE Journal of selected topics in applied earth observations and remote sensing, vol. 4, n3 September 2011.
- Pu, Y. Y., Sun, D. W., Riccioli, C., Buccheri, M., Grassi, M., Cattaneo, T. M., & Gowen, A. (2018). “Calibration transfer from micro NIR spectrometer to hyperspectral imaging: a case study on predicting soluble solids content of bananito fruit (*Musa acuminata*)” in Food analytical methods, 11(4), 1021-1033.
- Pust, O. (2016). “Innovative Filter Solutions for Hyperspectral Imaging”. In *Optik & Photonik*. <https://onlinelibrary.wiley.com/doi/pdf/10.1002/opph.201600012>
- Qin, J., Kim, M. S., Chao, K., Chan, D. E., Delwiche, S. R., & Cho, B. K. (2017). “Line-scan hyperspectral imaging techniques for food safety and quality applications”. *Applied Sciences*, 7(2), 125.
- Ramanan, A. & Nipe, G. (2018). “Hyperspectral Imaging fights food waste”. *Industrial Photonics*. <https://www.impactvi.com/hyperspectral-imaging-fights-food-waste/>
- Redmon, Joseph, Divvala, S., Girshick, R. & Farhadi, A. “You only look once: Unified, real-time object detection”. In *Proceedings of the IEEE conference on computer vision and pattern recognition*. 2016. p. 779-788.
- Rehman, T. U., Zhang, L., Ma, D., Wang, L., & Jin, J. (2020). “Calibration transfer across multiple hyperspectral imaging-based plant phenotyping systems: I–Spectral space adjustment.” In *Elsevier Journal of Computers and Electronics in Agriculture*, 176, 105685.
- “Resyntex: A New Circular Economy Concept for Textiles and Chemicals”. Retrieved from <http://www.resyntex.eu/>
- Rezagholi, F. & Hesarinejad, M.A (2017). “Integration of fuzzy logic and computer vision in intelligent quality control of celiac-friendly products”. *Procedia Computer Science*, Vol 120.
- Rodgers, J., & Beck, K. (2009). “NIR characterization and measurement of the cotton content of dyed blend fabrics”. *Textile research journal*, 79(8), 675-686.
- Rosenrater, K.A. & Evers, A-D. (2018) Chapter 9: Breakfast Cereals in “Kent’s technology of Cereals”. <https://doi.org/10.1016/B978-0-08-100529-3.00009-8>
- Sandin, G. & Peters, G.M, “ Environmental impact of textile reuse and recycling”, in *Elsevier Journal of Cleaner Production*, Volume 184, 20 May 2018, Pages 353-365
- Sarkar, N.R. “Machine vision for quality control in the food industry”. In I. Fung, & E. Matthews (Eds.), *Instrumental methods for quality assurance in foods* (pp. 167-187). New York: Marcel Decker.
- Savitzky, A., & Golay, M. J. (1964). “Smoothing and differentiation of data by simplified least squares procedures”. *Analytical chemistry*, 36(8), 1627-1639.
- Sawyer, T. W., Luthman, A. S., & Bohndiek, S. E. (2017). “Evaluation of illumination system uniformity for wide-field biomedical hyperspectral imaging”. *Journal of Optics*, 19(4), 045301.

- Schwandt, F., Hubert, M.E., Thomson, D.U., Vahl, C., Bartle, S.J. & Reinhardt, C.D. (2017). "Flake density, roll diameter and flake moisture all influence starch availability of steam-flaked corn". Kansas Agricultural Experiment Station Research Reports. 3. 10.4148/2378-5977.1356.
- Serranti, S., Gargiulo, A., & Bonifazi, G. (2011). "Characterization of post-consumer polyolefin wastes by hyperspectral imaging for quality control in recycling processes". *Waste Management*, 31(11), 2217-2227.
- Serranti, S. (2019). "Plastic waste monitoring and recycling by hyperspectral imaging technology". In *SPIE Future Sensing Technologies* (Vol. 11197, p. 1119706). International Society for Optics and Photonics.
- Sharma, S., Sharma, N., Sharma, R. & Handa, S. (2018). "Formulation of Functional Multigrain Bread and Evaluation of their Health Potential". *International Journal of Current Microbiology and Applied Sciences* ISSN: 2319-7706 Vol 7 Number 07.
- Shelton, D. & Martin, G. (2004). "Wheat and Flour Testing Methods: A Guide to Understanding Wheat and Flour Quality". By the Wheat Marketing Center, Inc. Portland Oregon. ABD, 2004.
- Shen, G., Pierna, J. A. F., Baeten, V., Cao, Y., Han, L., & Yang, Z. (2020). "Local anomaly detection and quantitative analysis of contaminants in soybean meal using near infrared imaging: The example of non-protein nitrogen". *Spectrochimica Acta Part A: Molecular and Biomolecular Spectroscopy*, 225, 117494.
- Signoroni, A., Conte, M., Plutino, A. & Rizzi, A. (2020) "Spatial–Spectral Evidence of Glare Influence on Hyperspectral Acquisitions". In *Sensors*, 20(16), 4373.
- Skvaril, J., Kyprianidis, K., Dahlquist, E. (2017) "Applications of near-infrared spectroscopy (NIRS) in biomass energy conversion processes: A review". *Applied Spectroscopy Reviews*. DOI: 10.1080/05704928.2017.1289471
- "Smallest hyperspectral camera", 2014. Retrieved from <https://www.gamaya.com/blog-posts/smallest-hyperspectral-camera>
- Smith, L. (2002). "A tutorial on principal component analysis". 2002. http://www.cs.otago.ac.nz/cosc453/student_tutorials/principal_components.pdf
- "Soex Recycling Germany, GmbH". <https://www.soex.de/en/recycling-germany/>
- Sun, D. W. (2000). "Inspecting pizza topping percentage and distribution by a computer vision method". *Journal of food engineering*, 44(4), 245-249.
- Sun, D. W. (Ed.). (2010). "Hyperspectral imaging for food quality analysis and control". Elsevier. ISBN 978-0-12-374753-2.
- Sun, J., Jian, S., Mao, H., Wu, X. & Li, Q. (2016). "Classification of black beans using visible and near infrared hyperspectral imaging". *International Journal of Food Properties*, 19:8, 1687-1695, DOI: 10.1080/10942912.2015.1055760
- "Sustainable production and consumption", 2020. Retrieved from: <https://ec.europa.eu/jrc/en/research-topic/sustainable-production-and-consumption>

Suzuki, S., Suzuki, Y., Ohta, H., Sugita, R. & Marumo, Y. "Microspectrophotometric discrimination of single fibers dyed by indigo and its derivatives using ultraviolet-visible transmittance spectra", *Science & Justice* 41, 107–111 (2001). [https://doi.org/10.1016/S1355-0306\(01\)71861-8](https://doi.org/10.1016/S1355-0306(01)71861-8)

SVM, PerClass. Retrieved from http://doc.perclass.com/perClass_Toolbox/guide/classifiers/svm.html

Szczypiński, P.M., Klepaczko, A. & Zapotoczny, P. (2015) "Identifying barley varieties by computer vision". *Journal Computers and Electronics in Agriculture*, Vol 110.

Szegedy, C., Liu, W., Jia, Y., Sermanet, P., Reed, S., Anguelov, D., ... & Rabinovich, A. (2015). "Going deeper with convolutions". In *Proceedings of the IEEE conference on computer vision and pattern recognition* (pp. 1-9).

"T4T project". <https://ec.europa.eu/environment/ecoinnovation/projects/en/projects/t4t>

Tack, K., Lambrechts, A., Soussan, P. & Haspelslagh, L. "A compact, high-speed, and low-cost hyperspectral imager", in *SPIE OPTO*, 2012. Vol 8266, *Silicon Photonics VII*; 82660Q (2012) <https://doi.org/10.1117/12.908172>.

Talaei, M., Mohammadifard, N., Khaje, M-R., Sarrafzadegan, N., Sajjadi, F., Alikhasi, H., Maghroun, M., Iraj, F. & Ehteshami, S. (2013). "Healthy Bread Initiative: Methods, Findings, and Theories—Isfahan Healthy Heart Program". *Journal of Health, Population and Nutrition*, March 2013.

Tan, C., Chen, H., Lin, Z., & Wu, T. (2019). "Category identification of textile fibers based on near-infrared spectroscopy combined with data description algorithms". *Vibrational Spectroscopy*, 100, 71-78.

Thirilogasundari, V., Suresh babu, V. & Janet, S.A. (2012) "Fuzzy based salt and pepper noise removal using adaptive switching median filter", in *Elsevier Procedia Engineering* 38, 2012.

Timmermans, A. J. M., & Hulzebosch, A. A. (1996). "Computer vision system for on-line sorting of pot plants using an artificial neural network classifier". in *Computers and Electronics in Agriculture*, 15(1), 41-55. 1996.

Tomasi, C. & Manduchi, R. (1998), "Bilateral filtering for gray and color images", in *Sixth International Conference on Computer Vision (IEEE Cat. No.98CH36271)*, January 1998

Toprak, T., Anis, P. "Textile industry's environmental effects and approaching cleaner production and sustainability, an overview." in *Journal of Textile Engineering and Fashion Technology*. 2017;2(4):429-442. DOI: 10.15406/jteft.2017.02.00066

Trang, N. T. Q., Ai, T. T. H., Giang, N. V., & Hoa, P. V. (2016). "Object-based vs. pixel-based classification of mangrove forest mapping in Vien An Dong Commune, Ngoc Hien District, Ca Mau Province using VNREDSat-1 images". *Advances in Remote Sensing*, 5(4), 284-295.

Traore, M.K. "Computational Frameworks: Systems, Models and Applications", Book by ISTE Press - Elsevier, 2017. 978-1-78548-256-4

Vaidya, S., Ambad, P. & Bhosle, S. "Industry 4.0 – A Glimpse", in *Elsevier Procedia Manufacturing* 20 (2018), 233-238, from 2nd International Conference on Materials Manufacturing and Design Engineering. <https://doi.org/10.1016/j.promfg.2018.02.034>

- Van De Vijver, R., Mertens, K., Heungens, K., Somers, B., Nuyttens, D., Borra-Serrano, I., ... Saeys, W. (2020). "In-field detection of *Alternaria solani* in potato crops using hyperspectral imaging". *Computers and Electronics in Agriculture*, 168(November), 105106.
- Van der Meer, F. D., Van der Werff, H. M., Van Ruitenbeek, F. J., Hecker, C. A., Bakker, W. H., Noomen, M. F., ... & Woldai, T. (2012). "Multi-and hyperspectral geologic remote sensing: A review". *International Journal of Applied Earth Observation and Geoinformation*, 14(1), 112-128.
- Vermeulen, P., Suman, M., Pierna, J. A. F., & Baeten, V. (2018). "Discrimination between durum and common wheat kernels using near infrared hyperspectral imaging". *Journal of Cereal Science*, 84, 74-82.
- Vinod, P., Ratnadeep, J., & Deshmukh, R. (2017) "Hyperspectral remote sensing for agriculture: a review". In *IJCA* (Vol. 172, No. 7).
- Wan, P., Toudeshki, A., Tan, H., & Ehsani, R. (2018). "A methodology for fresh tomato maturity detection using computer vision". *Computers and Electronics in Agriculture*, 146(February), 43–50. <https://doi.org/10.1016/j.compag.2018.01.011>
- Wang, H., Sun, D. "Correlation between cheese meltability determined with a computer vision method and with Arnott and Schreiber Tests". In *Journal of Food Science*, 2002. <https://doi.org/10.1111/J.1365-2621.2002.TB10670.X>
- Wang, X., Zhao, Ch., Huang, W., Wang, Q., Liu, Ch. & Yang, G. (2018). "Near-infrared hyperspectral imaging for detection and quantification of azodicarbonamide in flour". *Journal of Science and Food Agriculture*. 2018
- Wang, Z., Hu, M-H. & Zhai, G. "Application of Deep Learning Architectures for Accurate and Rapid Detection of Internal Mechanical Damage of Blueberry Using Hyperspectral Transmittance Data", in *Sensors Vol 18*, 2018.
- Weickert, J. (1998) "Anisotropic diffusion in image processing", in *ECMI Series*, Teubner-Verlag, Stuttgart, Germany, 1998.
- West, M., Grossmann, J., & Galvan, C. (2019). "Commercial Snapshot Spectral Imaging: The Art of the Possible."
- Wold, J.P., Johansen, I.R., Haugholt, K.H., Tschudi, J. & Thielemann, J. (2006) "Non-contact transreflectance near infrared imaging for representative on-line sampling of dried salted coalfish (bacalao)" in *Journal of Near Infrared Spectroscopy* 14 (1), 59-66, 2006.
- "xiSpec - Hyperspectral Cameras with USB3 Vision", Ximea. Retrieved from <https://www.ximea.com/en/usb3-vision-camera/hyperspectral-usb3-cameras-mini>
- Xiong, F., Zhou, J., Chanussot, J., & Qian, Y. (2019, September). "Dynamic material-aware object tracking in hyperspectral videos". In *2019 10th Workshop on Hyperspectral Imaging and Signal Processing: Evolution in Remote Sensing (WHISPERS)* (pp. 1-6). IEEE.
- Yang, X.; Hong, H.; You, Z.; Cheng, F. "Spectral and Image Integrated Analysis of Hyperspectral Data for Waxy Corn Seed Variety Classification". *Sensors* 2015, 15, 15578-15594. <https://doi.org/10.3390/s150715578>

- Yang, X., Ye, Y., Li, X., Lau, R.Y.K., Zhang, X. & Huang, X. "Hyperspectral image classification with deep-learning models", *IEEE Transactions on Geoscience and Remote Sensing*, April 2018.
- Yano, A., Takakusagi, M., Oikawa, K., Nakajo, S. & Sugawara, S. (2017) "Xanthophyll levels in foxtail millet grains according to variety and harvesting time". *Journal of Plant Production Science*.
- Yeom, J.S. "Textile Fingerprinting for Dismount Analysis in the Visible, Near, and Shortwave Infrared Domain". Thesis, Department of the Air Force Air University, 2014.
- Yiu, T (2019). <https://towardsdatascience.com/understanding-random-forest-58381e0602d2>
- Zhang, X., Liu, F., He, Y. & Li, X. (2012). "Application of hyperspectral imaging and chemometric calibrations for variety discrimination of maize seeds". *Sensors*, 2012, ISSN 1424-8220 www.mdpi.com/journal/sensors
- Zhao, H., Wang, Y., Liu, S., Li, K., & Gao, W. (2019). "Spectral reflectance characterization and fiber type discrimination for common natural textile materials using a portable spectroradiometer". *Journal of Archaeological Science*, 111, 105026.
- Zhao, X., Wang, W., Ni, X., Chu, X., Li, Y-F. & Sun, C. (2018). "Evaluation of Near-Infrared Hyperspectral Imaging for Detection of Peanut and Walnut Powders in Whole Wheat Flour". *Journal of Applied Sciences*, July 2018.
- Zhao, Y., Zhu, S., Zhang, C., Feng, X., Feng, L., & He, Y. (2018). "Application of hyperspectral imaging and chemometrics for variety classification of maize seeds". *Royal Society of Chemistry Advances*, 8(3), 1337-1345.

List of publications

Internationally reviewed academic journals

- Blanch-Pérez del Notario, C., Saeys, W. and Lambrechts, A. “Hyperspectral imaging for textile sorting in the visual-near infrared range”, in *Journal of Spectral Imaging* 8, 2019. <https://doi.org/10.1255/jsi.2019.a17>
- Blanch, C., Saeys, W. and Lambrechts, A. “Fast ingredient quantification in multigrain flour mixes using hyperspectral imaging”, in *Journal of Food Control*, vol. 118, 2020. <https://doi.org/10.1016/j.foodcont.2020.107366>
- Blanch-Pérez del Notario, C., López-Molina, C., Lambrechts, A. and Saeys, W. “Hyperspectral system trade-offs for illumination, hardware and analysis methods: a case study of seed mix ingredient discrimination”, in *Journal of Spectral Imaging* 9, a16 (2020). <https://doi.org/10.1255/jsi.2020.a16>.

Conference proceedings

- Blanch, C., Luyten, H., Saeys, W., and Lambrechts, A. “Optimized custom LED illumination for hyperspectral imaging” in the *International Conference for Near Infrared Spectroscopy (ICNIRS)*, 15-20 September 2019.
- Blanch-Pérez-del-Notario, C., Saeys, W., & Lambrechts, A. (2019, September). “Convolutional neural networks for heterogeneous ingredient discrimination with hyperspectral imaging”. In 2019 10th Workshop on Hyperspectral Imaging and Signal Processing: Evolution in Remote Sensing (WHISPERS) (pp. 1-6). IEEE.
- Blanch-Pérez-del-Notario, C., Luthman, S., Lefrant, R., Gonzalez, P. and Lambrechts, A. “Compact high-speed snapshot hyperspectral imager in the SWIR range (1.1-1.65 nm) and its potential in sorting/recycling industry”, submitted to SPIE Photonex Hyperspectral Imaging and Applications conference, September 2021.

Biography

Carolina Blanch Pérez del Notario was born in Pamplona, Spain. She received her M.S degree in Telecommunications Engineering from the Public University of Navarra, Spain, and an M.S. in Artificial Intelligence from the Katholieke Universiteit Leuven. Since 2002 she has been working as a Research Engineer at Imec, Belgium. Her research interests in the past included video coding and transmission, and cross-layer optimizations. Since 2012 she is working at the Integrated Imaging group in Imec as a Senior Research Engineer, where she is responsible for hyperspectral feasibility studies, focusing on machine learning methods and chemometric analysis.